



HAL
open science

Multiscale X-ray tomography of cementitious materials: A review

Sébastien Brisard, Marijana Serdar, Paulo J.M. Monteiro

► **To cite this version:**

Sébastien Brisard, Marijana Serdar, Paulo J.M. Monteiro. Multiscale X-ray tomography of cementitious materials: A review. *Cement and Concrete Research*, 2020, 128, pp.105824. 10.1016/j.cemconres.2019.105824 . hal-02384580

HAL Id: hal-02384580

<https://enpc.hal.science/hal-02384580>

Submitted on 28 Nov 2019

HAL is a multi-disciplinary open access archive for the deposit and dissemination of scientific research documents, whether they are published or not. The documents may come from teaching and research institutions in France or abroad, or from public or private research centers.

L'archive ouverte pluridisciplinaire **HAL**, est destinée au dépôt et à la diffusion de documents scientifiques de niveau recherche, publiés ou non, émanant des établissements d'enseignement et de recherche français ou étrangers, des laboratoires publics ou privés.

Multiscale X-ray Tomography of Cementitious Materials: a Review

Sébastien Brisard, Marijana Serdar, Paulo J.M. Monteiro

This is the accepted version of the following article: “Multiscale X-ray Tomography of Cementitious Materials: a Review”, which has been published in final form at <https://doi.org/10.1016/j.cemconres.2019.105824>.

The published version of this review paper includes many figures from other publications; these are not reproduced here.

© 2020. This manuscript version is made available under the [CC-BY-NC-ND 4.0](https://creativecommons.org/licenses/by-nc-nd/4.0/) license. See [Elsevier Sharing Policy](https://www.elsevier.com/locate/elsevierpolicy).

Multiscale X-ray Tomography of Cementitious Materials: a Review

Sébastien Brisard^{a,*}, Marijana Serdar^b, Paulo J.M. Monteiro^c

^aUniversité Paris-Est, Laboratoire Navier, ENPC, IFSTTAR, CNRS UMR 8205, F-77455 Marne-la-Vallée

^bUniversity of Zagreb, Faculty of Civil Engineering, Department of Materials, Fra Andrije Kačića-Miošića 26, 10000 Zagreb, Croatia

^cUniversity of California, Department of Civil & Environmental Engineering, Berkeley, 725 Davis Hall, Berkeley, CA 94720, USA

Abstract

X-ray computed tomography (CT) is a non-destructive technique that offers a 3D insight into the microstructure of thick (opaque) samples with virtually no preliminary sample preparation. Since its first medical application in 1973, the technique has improved dramatically in terms of acquisition times and resolution. The best resolution achievable for both parallel- and cone-beam setups is presently sub-micron. The macroscopic properties (stiffness, resistance, permeability, durability, ...) of cementitious materials are known to be significantly affected by their multiscale microstructure. This calls for x-ray CT investigations of cementitious materials down to the smallest length-scales. The present review first provides background information on the technique (including image-processing). It then covers various applications of x-ray CT to cementitious materials: imaging of the porous network, durability experiments, damage experiments, ..., cutting-edge nanotomography experiments. Current challenges such as time- and chemically- resolved experiments are also discussed.

Keywords: X-ray, computed tomography, micro tomography, microstructure, reconstruction, artefacts, hydration, durability, cracking

Contents

1 Introduction	1	4.4 Cleaning-up the segmented images	11
		4.5 Labelling	11
		4.6 Quantification of the processed images	12
A FROM SINOGRAMS TO 3D RECONSTRUCTIONS	3	B RECENT APPLICATIONS OF X-RAY COMPUTED TOMOGRAPHY TO CEMENTITIOUS MATERIALS	12
2 X-ray computed tomography in a nutshell	3	5 What can you expect to see? Contrast is of the essence	12
2.1 Absorption of x-rays by matter	4	6 Static observations	13
2.2 Parallel x-ray computed tomography	5	6.1 Observation of well-contrasted features	13
2.3 Reconstruction techniques for parallel projections	5	6.2 Intra-matrix observations	15
2.4 Reconstruction techniques for cone-beam projections	6	7 Dynamic observations	15
2.5 Reconstruction techniques for incomplete datasets	7	7.1 Hydration	16
3 Practical aspects of a x-ray CT experiment	7	7.2 Durability-related observations	16
3.1 Geometric considerations	7	7.3 Cracking	18
3.2 Calibration	7	C CUTTING-EDGE TOMOGRAPHY	18
3.3 Voxel size vs. resolution	8	8 Nanotomography	18
3.4 Artefacts	8	9 Challenges and opportunities	20
4 Image analysis of the 3D reconstructions	10		
4.1 Available software	10		
4.2 Denoising	10		
4.3 Segmentation of images	11		

*Corresponding author

Email addresses: sebastien.brisard@ifsttar.fr
(Sébastien Brisard), mserdar@grad.hr (Marijana Serdar),
monteiro@berkeley.edu (Paulo J.M. Monteiro)

1. Introduction

Cementitious materials are characterized by a complex, notoriously multiscale microstructure, the details of which play

Not reproduced

Figure 1: First x-ray image taken on 22 December 1895 by Wilhelm Röntgen and presented to Ludwig Zehnder of the Physik Institut, University of Freiburg, on 1 January 1896. The image represents the hand of Röntgen's wife and displays her wedding ring (courtesy of the U.S. National Library of Medicine, Dream Anatomy Gallery).

a significant role on the macroscopic properties, such as stiffness, strength, long-term deformation and durability. As a consequence, a large number of studies is dedicated to the sole characterization of the microstructure.

Traditional techniques of microstructure and chemical/mineralogical investigation include scanning and transmission electron microscopy (SEM and TEM) [1, 2], optical microscopy [3], mercury intrusion porosimetry (MIP) [4, 5], water absorption [6], gas adsorption/desorption [7, 8], thermogravimetric analysis [9] and x-ray diffraction [10] among others. However, the sample preparation required by these *ex-situ* techniques, such as cutting, grinding, polishing or high vacuum testing, often affects the microstructure irreversibly. Electron probe microanalysis (EPMA) [11, 12], nuclear magnetic resonance (NMR) [13–16], small-angle x-ray or neutron scattering (SAXS/SANS) [17–19] or ultrasonic measurements [20] are less invasive, alternative or complementary *in-situ* techniques. However, none of the above techniques provide three-dimensional visualization of the microstructure and information about the spatial distribution of its constituents (e.g. connectivity and tortuosity for pores).

X-ray computed tomography operates *in-situ* on samples with preparation kept to a minimum, and delivers three-dimensional images. Owing to the ability of x-rays to pass through thick, opaque objects, x-ray computed tomography is particularly well suited to the investigation of cementitious materials. This technique offers an unprecedented window on e.g. the porous network (including connectivity) down to a few tens of microns; the distribution of metallic fibers (for fiber reinforced concrete); the development of cracks, or the alteration of the cementitious matrix owing to various chemical degradation processes. Careful experiments might even deliver an insight into the spatial distribution of the hydration products, while recent developments aim at time-resolved experiments, such as monitoring hydration and in-situ crack propagation.

Röntgen discovered x-rays in 1895, and almost immediately applied his discovery to imaging. Quite famously, the first x-ray image is a radiograph of his wife's hand, who is believed to have said that she had seen her death on this occasion. In 1901, Röntgen received the Nobel Prize for his achievements.

It was soon realized that x-rays carried an immense potential for medical imaging. At the advent of World War I, the technique was already mature enough for Marie Curie to develop mobile x-ray vehicles that were sent to the battle fields. More than one century later, x-ray imaging has improved dramatically. Comparing first-generation (circa 1896) and modern x-ray systems, Kemerink et al. [21] concluded that the skin dose was reduced by a factor of about 1500, the corresponding ex-

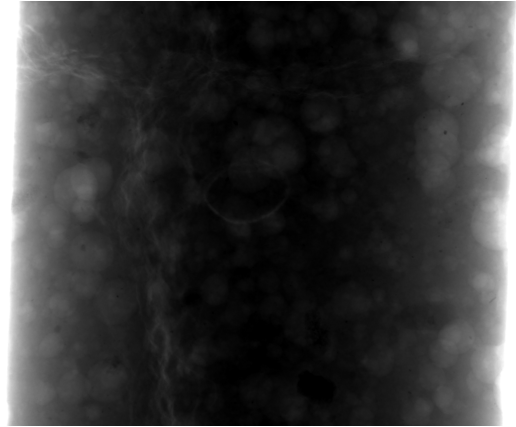


Figure 2: X-ray image of a cylindrical sample (diam.: 20 mm) of mortar (CEM I cement, 0.53 water-to-cement weight ratio, 3.0 sand-to-cement weight ratio). Owing to the projection artefacts, the image is barely legible, while the 3D reconstruction of the same sample, which results from the combination of a large number of such projections reveals fine details of the microstructure (see Figure 10).

Not reproduced

Figure 3: Lead numbers mounted in 1 cm distances on balsawood (left). The non-computed tomography delivers an image where all numbers are blurry, except for 7, that lies in the focal plane. (Reproduced from Reference [24], with permission.)

posure time going from 90 min down to 20 ms ($\times 1/270\,000$).

Despite its undisputable achievements in the medical field, x-ray imaging suffers from the fact that it provides a *projection* of the object of interest. In other words, information about depth is lost in the process. While this is not too problematic for not-too-thick and not-too-opaque samples (such as the human body), projection artefacts become prohibitive for cementitious materials (see Figure 2). To overcome this limitation, it was proposed to combine several projections. The human brain constructs a mental 3D image from the two views of the same scene captured by each eye (at slightly different angles). Similarly, a 3D image of a sample can be reconstructed from its projections at several angles; thus, tomography was born. The term itself comes from ancient Greek *tomos* (section, slice).

Tomography comes in two flavors [22]. *Non-computed (or conventional) tomography* on the one hand (also known as laminography, planigraphy, stratigraphy) dates back to the early 1920s and was initiated by Bocage among others [23]. In this approach, both the source and the film are moved simultaneously in opposite directions. The resulting image is a composite projection where the features that lie out of the focal plane are blurred (see Figure 3).

In his 1917 seminal paper, Radon on the other hand laid out the principles of *computed tomography* [25]. He provided a mathematical analysis of the associated transform that is called after him. Inversion of the Radon transform (which delivers the 3D reconstruction of the sample from its projections) requires a computer, and it was not until 1956 that Bracewell [26] imple-

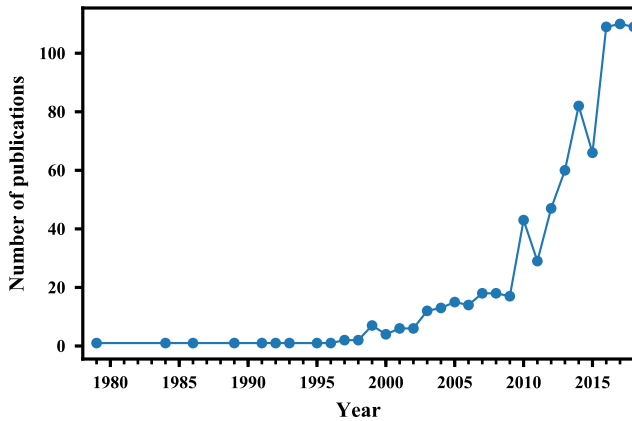


Figure 4: Number of publications related to x-ray tomography of cementitious materials (source: Scopus, using the following query: TITLE-ABS-KEY ((cement OR concrete) AND tomography AND x-ray) AND (EXCLUDE (SUBJAREA, "MEDI") OR EXCLUDE (SUBJAREA, "BIOC") OR EXCLUDE (SUBJAREA, "PHYS") OR EXCLUDE (SUBJAREA, "DENT") OR EXCLUDE (SUBJAREA, "NEUR") OR EXCLUDE (SUBJAREA, "HEAL") OR EXCLUDE (SUBJAREA, "AGRI") OR EXCLUDE (SUBJAREA, "SOC") OR EXCLUDE (SUBJAREA, "PHAR") OR EXCLUDE (SUBJAREA, "IMMU") OR EXCLUDE (SUBJAREA, "PSYC") OR EXCLUDE (SUBJAREA, "VETE") OR EXCLUDE (SUBJAREA, "BUSI") OR EXCLUDE (SUBJAREA, "ARTS") OR EXCLUDE (SUBJAREA, "NURS") OR EXCLUDE (SUBJAREA, "DECI"))).

mented a reconstruction algorithm for radio-astronomy images that was later to be adopted for x-ray computed (or computerized) tomography as well. Computed tomography is usually attributed to Cormack and Hounsfield, who received the Nobel Prize for medicine in 1979. Cormack’s contribution is mostly theoretical, while Hounsfield is regarded as the inventor of clinical computed tomography in 1973 [27].

Computed tomography was initially intended for medical applications. However, it was soon realized that this technique had enormous potential for materials science. Although one of the first applications of x-ray computed tomography to cementitious materials dates back to the late 1970s [28, 29], the technique really took off at the beginning of the 21st century (see Figure 4).

This paper provides an overview of applications of x-ray computed tomography to cementitious materials. The first part provides background knowledge on the technique itself (see sections 2 and 3) and the post-processing of the resulting 3D images. After discussing what can be expected from x-ray imaging of cementitious materials in section 5, the second part reviews various recent applications. We cover both “static” (see Section 6) and “dynamic” (see Section 7) applications. In sections 8 and 9 discuss “cutting-edge” tomography and future developments, including nanotomography, ultra-fast tomography and chemical mapping. In the remainder of this paper, we will often use the abbreviation CT for “computed tomography”. Where resolution matters, we will also refer to systems that have a micron or submicron resolution as micro-CT. Finally, systems allowing spatial resolution better than 50 nm will be referred to as nano-CT.

A. FROM SINOGRAMS TO 3D RECONSTRUCTIONS

2. X-ray computed tomography in a nutshell

X-ray computed tomography is a non-destructive technique that provides a gray level, three-dimensional image of the sample under investigation. As the gray values are related to the local chemical composition, they reflect the local microstructure.

This section provides a brief overview of the essential theoretical aspects underlying the principles of x-ray CT, including: production of x-rays, interaction of x-rays with matter, tomographic reconstruction and image artefacts. For the sake of brevity, each topic will be only touched upon, but more thorough references are provided along the text to the interested reader. There is a very large body of literature dealing with x-ray CT. Beyond the classical (but dated) textbook by Kak and Slaney [30], the authors found References [22, 31–34] (textbooks) and [35–37] (review papers) particularly helpful for the preparation of this review.

A typical (simplified) tomography setup comprises 3 parts (see Figures 5 and 6)

1. **The source** produces x-rays. Synchrotron sources produce beams that can essentially be considered as parallel (emitted rays come from one unique direction). Conversely, x-ray tubes that come in laboratory setups produce conic beams (emitted rays emerge from one focal spot). Both synchrotron and laboratory x-ray sources are polychromatic (photon wave-lengths are distributed according to the source spectrum). The large flux of photons produced by synchrotron sources allows for aggressive filtering that can achieve near-monochromaticity. This is the typical operating mode of synchrotron tomography setups, although so-called “pink”-mode imaging (moderately polychromatic beam) is also popular for specific applications, such as dynamic tomography.
2. **The detector** measures the intensity of the attenuated x-rays emerging from the sample. Typically, a scintillator first converts X photons to visible light photons. Then, a 2D CCD sensor records these photons and produces a 2D image (the radiograph).
3. **The sample stage** sits between the source and the detector. It can be rotated about a fixed (vertical) axis, thus allowing for the acquisition of radiographs of the sample for a number of rotation angles.

The output of a x-ray CT experiment is thus a stack of radiographs of the same sample, viewed at various angles. Tomographic reconstruction is the mathematical process that allows to recover a 3D image of the interior of the sample from this stack. It is an *inverse* problem, the solution of which requires a mathematical description of the *forward* problem. In other words, we need to understand what is the mathematical relationship between the (local) physical properties of the sample and its radiographs. This is discussed in the remainder of the present section.

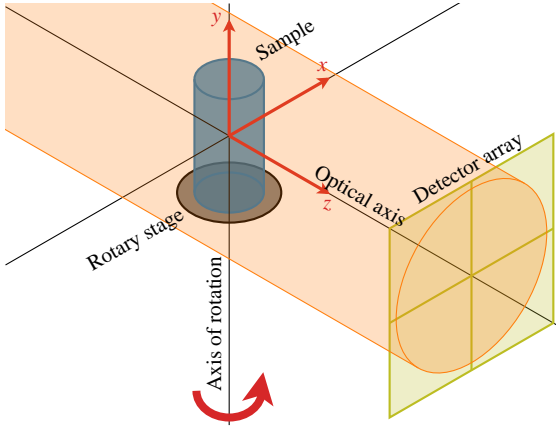


Figure 5: A typical parallel tomography setup.

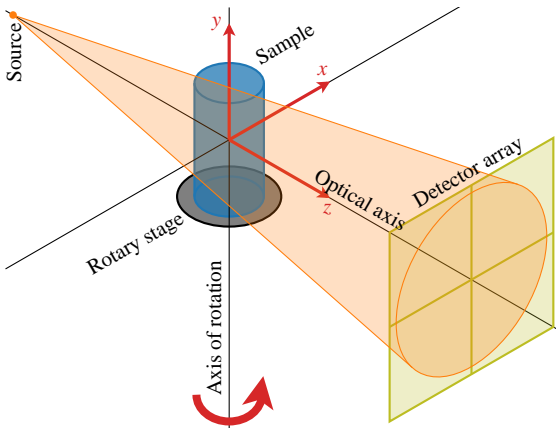


Figure 6: A typical cone-beam tomography setup.

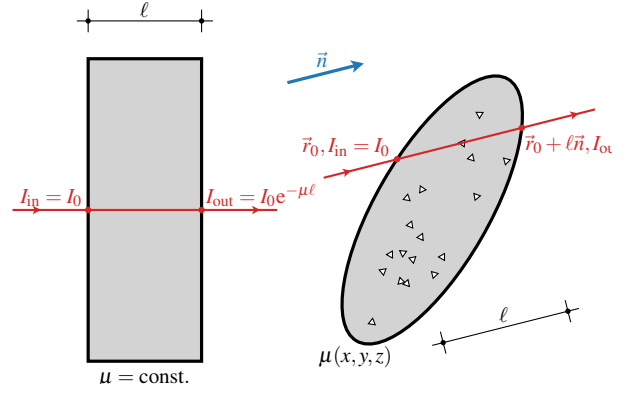


Figure 7: Illustration of the Beer–Lambert law for a homogeneous sample of constant thickness (left) and a heterogeneous sample (right).

2.1. Absorption of x-rays by matter

The classical assumption underlying most x-ray CT reconstruction algorithms is that x-rays are absorbed by matter according to the Beer–Lambert law, which relates the intensity I of the x-ray beam that emerges from a sample to the intensity I_0 of the incident x-ray beam. This simplification of the reality delivers satisfactory results in most cases.

For a homogeneous sample of constant thickness ℓ , illuminated by a monochromatic x-ray beam, this law reads (see also Figure 7, left)

$$I = I_0 e^{-\mu \ell}, \quad (1)$$

where μ denotes the so-called linear attenuation coefficient.

The linear attenuation coefficient is a material property that essentially depends on the atomic number and density and accounts for photoelectric attenuation, incoherent Compton scattering and coherent Rayleigh scattering. It also strongly depends on the energy of the incident x-ray beam. In laboratory (polychromatic) setups, this can cause significant artefacts due to *beam hardening* (see Section 3.4).

Tabulated values of the *mass attenuation coefficient* μ_α/ρ_α (ρ_α : mass per unit volume) can be freely retrieved for all chemical elements α from various databases, such as XCOM at NIST¹ or the X-Ray Database at LBNL, CXRO² [38]. Then, the mass attenuation coefficient of a compound is obtained from the following rule of mixtures (x_α : fraction by weight of the α -th element)

$$\frac{\mu}{\rho} = \sum_{\alpha} x_{\alpha} \frac{\mu_{\alpha}}{\rho_{\alpha}}. \quad (2)$$

Figure 8 represents the linear attenuation coefficient as a function of the photon energy for various materials: water, (dry) air, iron (which is close to steel), as well as some constitutive phases of anhydrous/hydrated cement (portlandite, alite, C–S–H). Such a plot is a valuable tool to plan a tomography experiment. In particular, it allows the user to estimate the expected contrast between phases, as well as the overall transmission

¹<http://physics.nist.gov/xaamdi>, last retrieved 2019-06-19.

²http://henke.lbl.gov/optical_constants/, last retrieved 2019-06-19.

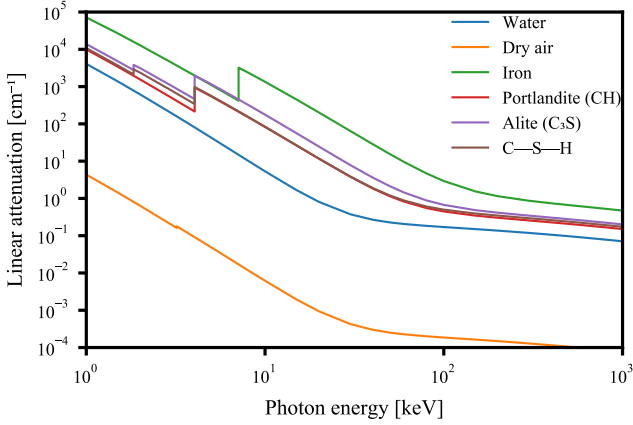


Figure 8: Linear attenuation coefficient for various phases of cementitious materials. The typical energy range for micro-CT experiments is 10 keV to 100 keV. For nano-CT, it is also possible to use soft x-rays (0.1 keV to 1.5 keV).

through the sample. Based on these preliminary calculations, the energy of the source and the overall size of the sample can be selected.

It is observed in Figure 8 that the contrast between hydration products on the one hand and water, air and steel on the other hand is excellent. In other words, pores and cracks (dry samples preferably), steel reinforcement and hardened cement paste are usually easily identifiable on a tomographic reconstruction. However, the contrast between the various hydration products is rather poor, so that they generally must be considered as a unique phase.

Equation (1) can readily be extended to heterogeneous samples as follows (see also Figure 7, right)

$$I = I_0 \exp\left[-\int_0^\ell \mu(\vec{r}_0 + s\vec{n}) ds\right], \quad (3)$$

where $\mu(\vec{r})$ now denotes the *local* linear attenuation coefficient at point $\vec{r} = (x, y, z)$, and s is the arc-length measured along the ray. It is assumed that x-rays propagate along the unit vector $\vec{n} = (n_x, n_y, n_z)$. The integral must then be computed between the entry point $\vec{r}_0 = (x_0, y_0, z_0)$ and the exit point $\vec{r}_0 + \ell\vec{n}$ of the x-ray into the sample (ℓ : distance between these two points).

2.2. Parallel x-ray computed tomography

It is assumed that the geometry of the setup is free of imperfections: in particular, the detector is plane, x-rays propagate perpendicular to the detector and the rotation axis is parallel to the detector. Let $(O, \vec{e}_x, \vec{e}_y, \vec{e}_z)$ denote the fixed frame of reference, attached to the laboratory. The direction of propagation of the x-rays is (O, \vec{e}_z) , while the (vertical) axis of rotation of the sample stage is (O, \vec{e}_y) axis.

We first assume that the sample is not rotated. Let $I(x, y)$ denote the x-ray intensity measured at pixel (x, y) of the detector. From the Beer–Lambert law (3), it is readily found that

$$I(x, y) = I_0 \exp\left[-\int \mu(x, y, z) dz\right]. \quad (4)$$

Equation (4) effectively provides the mathematical expression of the *radiograph* of the sample. It will be convenient to also introduce the *projection* of the sample's x-ray attenuation field, which is defined as the following quantity

$$P(x, y) = \int \mu(x, y, z) dz, \quad (5)$$

and we have $P(x, y) = \log I_0 - \log I(x, y)$. It will be shown in Section 3.2 how appropriate calibration delivers an estimate of the projection P of the sample from its measured radiograph I .

Assuming now that the sample is rotated, it is convenient to define the frame $(O, \vec{e}_X, \vec{e}_Y, \vec{e}_Z)$ attached to the sample stage, and the rotation angle θ such that

$$\vec{e}_X = \cos \theta \vec{e}_x - \sin \theta \vec{e}_z, \quad \vec{e}_Y = \vec{e}_y, \quad \vec{e}_Z = \sin \theta \vec{e}_x + \cos \theta \vec{e}_z. \quad (6)$$

The sample is attached to the sample stage. Therefore, its local linear attenuation coefficient $\mu(X, Y, Z)$ is expressed in the (X, Y, Z) coordinate system. In other words, the projection $P(x, y, \theta)$ of the sample rotated by θ reads

$$P(x, y, \theta) = \int \mu(x \cos \theta - z \sin \theta, y, x \sin \theta + z \cos \theta) dz. \quad (7)$$

Retrieving $\mu(X, Y, Z)$ from the set of projections $P(x, y, \theta)$ (tomography stack) is an inverse problem known as *tomography reconstruction*. That this problem indeed has a unique solution was established by Radon [25] one hundred years ago almost to the day; the modern proof of this result relies on the Fourier slice theorem (usually attributed to Bracewell [26])

The 1D Fourier transform (with respect to x) of the projection $P(x, y, \theta)$ at angle θ of the object is equal to a radial slice at polar angle θ of the 2D Fourier transform (with respect to X and Z) of the linear attenuation coefficient $\mu(X, Y = y, Z)$.

Note that in the integral equation (7), the altitude y of the horizontal plane is fixed in both sides. In other words –for parallel tomography– tomographic reconstruction (if possible at all) can be performed horizontal slice by horizontal slice and is essentially a 2D (rather than 3D) problem. This greatly alleviates the computational cost of tomographic reconstruction in the case of parallel tomography. However, this uncoupling breaks down in the case of cone-beam tomography, as will be discussed in Section 2.4.

2.3. Reconstruction techniques for parallel projections

Direct Fourier reconstruction methods. In principle, the Fourier slice theorem provides a method for reconstructing the map of the linear attenuation coefficient from the projections. The outline of this method, first proposed by De Rosier and Klug [39] is the following:

1. compute the 1D Fourier transform of each projection of the object,
2. reconstruct the 2D Fourier transform of the linear attenuation coefficient from its radial slices,

3. compute the linear attenuation coefficient as an inverse Fourier transform.

Practical implementation of the above method is however problematic, since the necessary interpolation that occurs between steps 2 and 3 in Fourier space from a polar grid generated by collating 1D radial slices through the sample to a cartesian grid required by standard 2D FFT techniques can induce severe losses of accuracy [40]. The resulting reconstructions are generally inferior in quality to that produced with the filtered backprojection method described below. As a consequence, this method is rarely implemented in practice, despite the fact that it can outperform the filtered backprojection method in terms of computational time [41] owing to a lower complexity.

Recently, more sophisticated methods based on direct reconstruction have been proposed, which significantly improve the quality of the reconstruction, while preserving the overall efficiency. Natterer [42] suggests a nearest-neighbor interpolation in the angular variables, and generalized sinc interpolation in the radial variable. Edholm and Herman [43, 44] introduce so-called *linograms* to replace standard sinograms, with no need for interpolation. Finally, non-equispaced, fast Fourier transforms [41, 45, 46] have also been used.

Owing to the advent of ultra-fast synchrotron tomography, direct Fourier reconstruction methods have again attracted some interest.

The filtered backprojection method. First proposed by Ramachandran and Lakshminarayanan [47], this method is probably the most widely used reconstruction technique. It results from the reformulation of the direct reconstruction method using cylindrical coordinates in the Fourier space [see 30, §3.3]. It is rather simple to implement, less CPU intensive than algebraic techniques and leads to very accurate reconstructions. It proceeds as follows

1. convolve each projection with a discrete filter that approximates the ramp filter in Fourier space [48],
2. compute the backprojection of the resulting filtered projections (see Figure 9).

Step 1 can be performed either in the real space or the Fourier space; step 2 is illustrated in Figure 9. Note that most modern implementations of this reconstruction method make use of GPUs [49].

Algebraic reconstruction methods. A different class of reconstruction methods was introduced in the early 70s by Gordon et al. [50] (see also the review by Beister [51]). Algebraic reconstruction methods rely on the observation that the linear integral equation (7) reduces to a linear system upon suitable discretization. For example, for pixel-based reconstructions, the unknown local linear attenuation map $\mu(X, Y, Z)$ reduces to a discrete set of pixel values. Discretization of the integral in equation (7) then amounts to finding the contribution of each individual pixel to the projections. This contribution is usually estimated as either of the three options below and then suitably normalized [52]

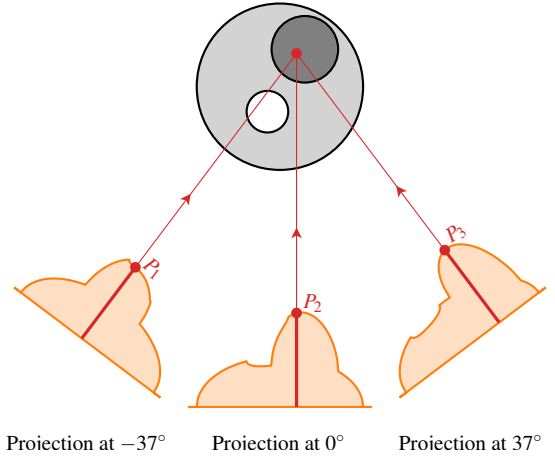


Figure 9: Illustration of the backprojection method. If three projections of the sample are available, the backprojected value at the marked point is the sum $P_1 + P_2 + P_3$.

1. 0 or 1, depending on whether or not the ray under consideration intersects the pixel,
2. the length of the intersection of the pixel and the ray under consideration,
3. the area of the intersection of the pixel and the pencil of rays under consideration.

The resulting linear system is extremely large, but sparse, and is usually solved iteratively. Dedicated solvers were initially proposed, such as the *Algebraic Reconstruction Technique* (ART) [50] and its relaxed version [53], the *Simultaneous Iterative Reconstruction Technique* (SIRT) [54] or the *Simultaneous Algebraic Reconstruction Technique* (SART) [55]. General-purpose solvers such as conjugate gradient can also be used [56–58].

As always with iterative algorithms, attention must be paid to the stopping criterion. Besides classical “no-improvement criteria”, Morozov’s discrepancy principle can be valuable if an estimate of the noise level is available. Also, it should be noted that early termination of the iterations can have a beneficial effect on the robustness to noise of some iterative methods [57].

Being more computationally intensive, algebraic reconstruction methods have long been neglected. However, the asset of such methods lies in their flexibility. It is possible to introduce box constraints [59, 60], various regularization terms [59, 61], or even perform reconstruction and segmentation simultaneously [62, 63]. It is also possible to introduce a refined model which better accounts for the actual tomography setup (source, detector) as well as a priori information on the imaged object [64–67].

2.4. Reconstruction techniques for cone-beam projections

For cone-beam projections, an explicit inversion formula was proposed by Tuy [68]. This formula holds only under some conditions that apply to the curve described by the point source. In the most common case of *circular* scans, Tuy’s condition is not fulfilled. Finch [69] has shown that reconstruction might

still be possible if the source is sufficiently far from the object; it is, however, *unstable* (hence, sensitive to noise).

Even if some techniques are known to produce convincing reconstructions, it should be kept in mind that for cone-beam projections with circular scans, these techniques are *inexact*; in particular artefacts and severe distortions might be observed for slices that are far-off from the central plane (see Section 3.4).

Furthermore, for cone-beam projections, horizontal slices are not independent and reconstruction can in principle no longer proceed slice by slice. Of course, algebraic reconstruction methods discussed above apply equally well here, provided that the *full*, 3D dataset is processed simultaneously. This however results in CPU- and memory-intensive computations.

Despite the fact that the Fourier slice theorem does not hold in that case, Feldkamp et al. [70] have proposed a filtered backprojection reconstruction method for cone-beam projections. The algorithm is extremely efficient, as horizontal slices are again reconstructed independently.

Note that an exact filtered backprojection formula can be retrieved for *helical tomography*, where the sample is translated vertically while being rotated about the vertical axis [71–73]. However, this technique is not widely spread in materials sciences labs.

2.5. Reconstruction techniques for incomplete datasets

The reconstruction techniques discussed in Sections 2.3 and 2.4 require full datasets, meaning that:

1. the sample is fully contained in the field of view,
2. the sample is fully rotated (180° for parallel tomography, 360° for cone-beam tomography),
3. the angular sampling rate is selected according to the Nyquist criterion. For parallel tomography, the minimum number of equally spaced projections is $W\pi/2$, where W denotes the width of the detector, in pixels (see Reference [22], page 219).

Local tomography [74] addresses acquisitions that fail to comply with item 1. Typical reconstruction techniques are sinogram extrapolation [75, 76], differential backprojection [77, 78], total variation minimization [79–81] or regularization with other prior knowledge on the sample [82–84]. Heußner et al. [85], dealing with medical applications, proposed to complement the dataset with a previous scan of the same patient; they even showed that scans of *similar* (but different) patients provide relevant priors. For synchrotron tomography, an alternative approach is to “stitch” together several tomograms of adjacent regions of interest [86, 87], registration being then the critical issue [88].

Limited angle tomography refers to experiments that do not cover the whole $180^\circ/360^\circ$ range (see item 2) as is usually the case of flat samples. The artefacts that result from the so-called *missing wedge* are well-known in electron tomography, where the sample can never be fully rotated [89]. The reconstruction problem then becomes extremely ill-conditioned [90] and some regularization must be provided in order to compensate

for the missing data. Classical techniques include total variation minimization [59, 91, 92], ℓ_0 sparse regularization [93] and wavelet/curvelet expansions [94, 95].

To close this discussion on incomplete datasets, it should be noted that many recent developments in both synchrotron and laboratory tomography aim at fast acquisitions. In synchrotron facilities, it is possible to take advantage of the high flux of photons to reduce the total acquisition time by shortening the exposure time of each single projection [96], the limiting factor often being the bandwidth of the detection and readout system [97]. This is unfortunately not an option with laboratory instruments, where the overall acquisition time must be shortened by reducing the total number of projections. Similarly to limited angle tomography, it is then necessary to regularize the ill-posed reconstruction problem. The same generic techniques as for limited angle tomography apply here. Some application dependent techniques have also been developed, which mostly amount to reconstruction under the constraint of prior knowledge on the microstructure in some “reference” state: dry [64, 98], unloaded [65–67].

3. Practical aspects of a x-ray CT experiment

3.1. Geometric considerations

Samples are preferably of circular cylindrical shape, for two main reasons. First, it best accommodates the geometric requirement that the sample should be fully projected onto the detector for all projection angles (unless local tomography is performed). Second, edges are more likely to produce reconstruction artefacts.

The size of the sample is determined by the above-mentioned geometric constraint as well as the total attenuation of the sample. Indeed, the transmission should be large enough to ensure a satisfactory signal-to-noise ratio, which behaves as $N_0^{1/2} \exp(-\mu D/2)$ for homogeneous samples of diameter D and linear attenuation coefficient μ (N_0 : total number of incident photons per pixel).

For cone-beam tomography, magnification is purely geometric. Indeed, it is related to the source-to-sample distance through the relation

$$\text{magnification} = \frac{\text{source-to-sample distance}}{\text{source-to-detector distance}},$$

and the voxel-size of the reconstructed image is given by the pixel-size of the detector, divided by the magnification. Optical magnification devices are used in synchrotron tomography.

3.2. Calibration

Calibration is a necessary step that allows the determination of the normalized intensity $N = I/I_0$. The projection images, to be fed to the reconstruction algorithm, are then evaluated as the logarithm of the normalized data [see equation (3)]. In principle, the incident intensity I_0 can be measured through removal of the sample. However, owing to the thermally induced dark current of the CCD pixels, the measured intensity is never

rigorously zero, even when the incident beam is turned off. Assuming linearity of the detector pixels, this is accounted for by the so-called *flat-field correction* [33]

$$N = \frac{I - D}{F - D}, \quad (8)$$

where I denotes the intensity measured with the sample in place, F (flat field) is the intensity measured after removal of the sample, and D (dark field) is the intensity measured after turning off the x-ray source. Note that, in order to account for the non-uniformity of both the incident beam and the CCD response that can result in ring artefacts in the reconstruction (see Section 3.4), the values of F and D in equation (8) must be considered as pixel-dependent (F and D are effectively *images*) [99]. More sophisticated normalization procedures have recently been proposed to account for the non-stationarity of the incident beam [100, 101]. Also, the advent of photon counting detectors should remove the need for dark-field corrections [102, 103].

3.3. Voxel size vs. resolution

It should be emphasized that voxel size and resolution refer to two different concepts. In a x-ray CT experiment, the voxel size results from an essentially geometrical calculation, that relates the true dimensions of the sample to the size (in voxels) of its 3D reconstruction. Resolution, on the other hand, is an optical quantity that quantifies the ability of an imaging setup to separate close objects. Resolution is affected by noise, spot size and other physical effects. This is best explained by Cnudde and Boone [36]: “*voxel size is often confused with spatial resolution. The latter is a measure for the resolving power of an imaging system based on the modulation transfer function (MTF) of the complete imaging system, expressed in line pairs per distance unit*”.

3.4. Artefacts

The present section is restricted to the most significant source of artefacts that affect the reconstructed volumes, namely: rings, streaks, partial-volume effects, beam-hardening and cone-beam reconstruction errors. For a more thorough review of this subject, see References [22, 34, 104] (textbooks) or [105–109] (papers).

Ring artefacts. Ring artefacts (see Figure 10, bottom right) are induced by variations in the acquisition system: temporal variations (the intensity of the source may vary with time), spatial variations (the various pixels of the detector may have slightly different response functions; some pixels could even be defunct) or spectral (the sensitivity of the pixels may depend non-linearly on the energy of the photons). These variations can cause in the reconstructed volume circular rings centered on the axis of rotation.

The flat-field correction discussed in Section 3.2 accounts for spatial variations of the pixels of the detector. If the time variations of the source are important, this correction must be renewed frequently during acquisition [100, 101]. Also, to account for defective pixels, the detector may be slightly shifted in its plane between the acquisition of two projections [110].

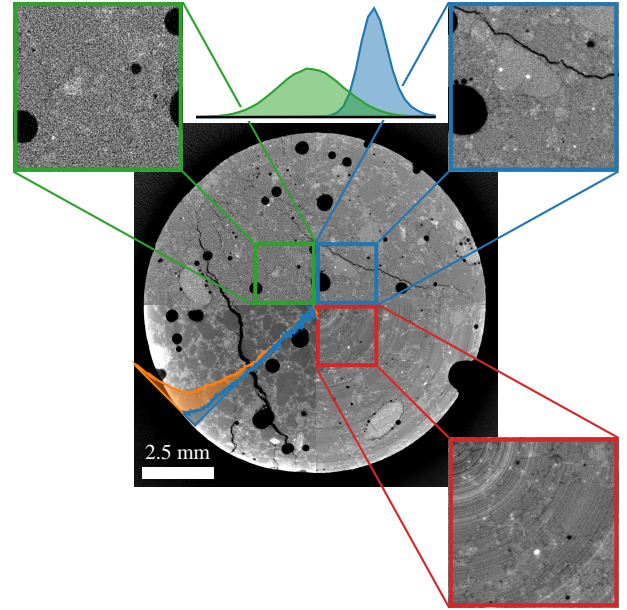


Figure 10: Noise, beam-hardening and ring artefacts. This slice through the 3D reconstruction of the sample shown in Figure 2 is a composite image combining 4 different tomograms of the same sample. Each time, the acquisition parameters were adjusted so as to emphasize a specific type of artefact. *Top right*: the reference image (voltage: 100 kV, current: 120 μ A, frame rate: 1 s^{-1} , averaging: 4 frames). *Top left*: the grainy texture is the signature of the increased noise induced by a reduction of the acquisition time (voltage: 100 kV, current: 120 μ A, frame rate: 4 s^{-1} , averaging: none). The histograms of the reference (blue) and noisy (green) images show that the overall signal is reduced (the peak is shifted to the left), while noise increases (the peak is wider), both effects leading to a deterioration of the signal-to-noise ratio. *Bottom right*: cancelling the calibration of the tomograph and stopping the wobbling of the detector results in very noticeable ring artefacts (voltage: 100 kV, current: 120 μ A, frame rate: 1 s^{-1} , averaging: 4 frames). *Bottom left*: low-energy, unfiltered scans lead to pronounced beam-hardening artefacts (voltage: 100 kV, current: 120 μ A, frame rate: 1 s^{-1} , averaging: 4 frames). The rim of the sample appears brighter than its core. This is confirmed by the two profiles, which are circular averages of the gray level within the cement matrix (pores and cracks excluded) of the reference (blue) image and the image affected by beam-hardening (orange). While the profile of the former is nearly flat as expected, the profile of the latter is peaked at the border. For all tomograms, the voxel size was approx. 12 μ m; unless otherwise specified, a 0.1 mm thick Cu filter was used.

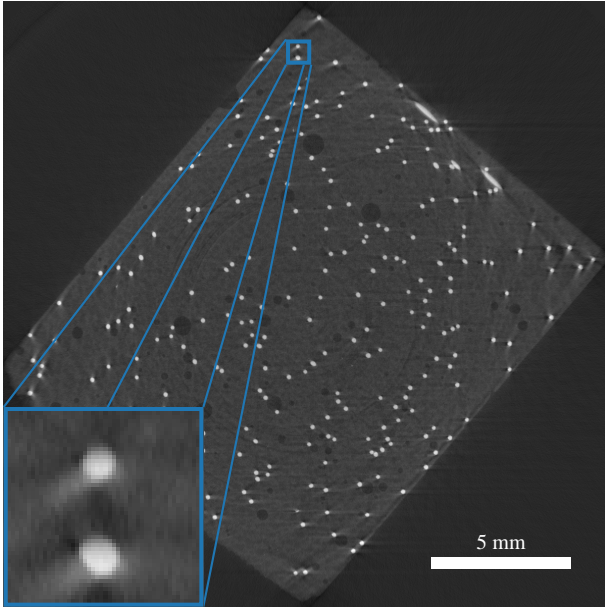


Figure 11: Illustration of streak artefacts. Reconstruction of a 20 mm×20 mm×20 mm sample of ultra-high performance concrete, with 2 % vol. steel fibers (0.2 mm diam.). Images were acquired at the Advanced Light Source in Berkeley, 2007, in white-beam mode with a 6 mm aluminum filter.

Streaks. Streak artefacts (see Figure 11) may appear in the neighborhood of *i.* sharp edges of the sample [35] and *ii.* highly attenuating phases (typically, metals). Item *i.* again reinforces the advantage of using cylindrical samples.

Item *ii.* is usually referred to as “metal artefacts” [111]. The reason why high attenuation may be detrimental to the reconstruction is best understood in the case of a fully opaque phase [104, §4.4.4]. Indeed, in this case, the opaque phase acts as a screen, which effectively results in missing data in the projections and artefacts similar to those observed in limited angle tomography. Similar reconstruction techniques can therefore also be adopted in order to reduce metal artefacts [112–114]. Metal artefacts may also be attributed to beam hardening [34, §5.2.4] (see below). Dual-energy CT therefore helps reducing these artefacts [115, 116].

Partial volume effect. The reconstructed volume is effectively an assembly of voxels with constant attenuation. However, the underlying material might well be heterogeneous at a much smaller scale than the voxel size. One voxel of the reconstructed volume then represents a heterogeneous region of the sample, and the gray level of the voxel represents an “effective” linear attenuation. This is known as the partial volume effect, which results among others effects in blurred interfaces. The resolution of the setup is generally larger than the voxel size, which tends to increase these artefacts.

As argued by Ketcham and Carlson [35, §4.4] (see also more recently [117]), it is possible to take advantage of partial volume effects to estimate the chemical composition of each voxel of the material. To this end, the “effective” attenuation is generally estimated through a simple mixture law (see also [118] for an alternative, more elaborate, approach).

Beam hardening. Beam hardening is caused by the lack of monochromaticity of the incident beam. Therefore, it can safely be assumed that synchrotron tomography reconstructions are devoid of such artefacts when operating in monochromatic or pink beam modes [119]. Conversely, synchrotron tomography operating in white beam mode and laboratory (cone-beam) tomography both suffer from beam hardening artefacts, which must be corrected.

Owing to the fact that the linear attenuation coefficient is energy-dependent (see e.g. Figure 8), equation (4) must be adapted to account for the spectrum of the source [104, §4.4.1]. Since the linear attenuation coefficient decreases when the energy increases, the spectrum tends to be shifted towards higher energies. This shift is more pronounced for thick samples. Most reconstruction algorithms are inexact when beam-hardening occurs, and the sample seems brighter on its rim than at its center (see e.g. [35, 107] and Figure 10, bottom left).

To prevent beam hardening, copper, brass or aluminum plates are often placed between the source and the sample to filter out lower energies [35]. The price to pay is a lower signal-to-noise ratio (which can be compensated for by a longer acquisition time).

Algorithmic correction is also possible. Although inexact, this approach is quite effective in removing beam-hardening artefacts [120]. In the so-called *linearization technique*, a polynomial correction is applied to the raw projections [34, §5.3.1.2]. The coefficients of this polynomial are usually first calibrated using a reference sample that is similar to the sample of interest [see also 121, for an alternative approach]. More rigorous, iterative methods should also be mentioned [122–124].

Cone-beam reconstruction errors. Cone-beam reconstruction errors result from the fact that (even disregarding issues relating to resolution) tomography reconstruction is not exact in a circular cone-beam setup (see References [68, 69] or §5.2.1 in Reference [34]). Such errors are sometimes called inappropriately Feldkamp artefacts, despite the fact that they result from the acquisition itself, regardless of the reconstruction technique.

Missing projection data causes blurring in the direction of the rotation axis. This effect is more pronounced for large cone angles [107].

In order to reduce the adverse effect of reconstruction errors, one should make sure that the region of interest remains close to the plane that is perpendicular to the axis of rotation and contains the x-ray source.

Noise. Noise affects any tomography experiment [34, §5.2.6]. Like any optical devices, increasing the acquisition time classically results in an improved signal-to-noise ratio (SNR) for each projection. As a rule of thumb, Davis and Elliott [107] claim that the SNR is optimal when the transmission is about 16 % at the center of the sample.

Tomography reconstruction is a complex process, and there are few studies on how noise propagates from the projections to the 3D reconstruction. It is known that noise is anisotropic [107], resulting in random streaks in the long direction of elongated features. More quantitatively, the seminal paper of Hegerl and

Hoppe [125] relates the noise level in the reconstruction to the noise level in the projections. The authors prove the somewhat counter-intuitive dose-fractionation theorem, which states that the SNR in the reconstruction is proportional to the total radiation dose used during the whole scan. In other words, the dose can be “shared” amongst the projections: if the total number of projections is multiplied by two, the exposure time per projection can be divided by two to achieve the same final SNR. Although debated [126], this result has been confirmed (and extended) numerically by McEwen et al. [127]. Further studies [128–132] show that for fixed SNR, increasing the spatial resolution requires to increase the dose [see also 104, §4.4.5].

Iterative reconstruction techniques are usually less sensitive to noise than analytical ones (since a noise model can be incorporated). Regardless of the reconstruction process, post-reconstruction filtering of the images can be applied to reduce the adverse effects of noise (see Section 4).

4. Image analysis of the 3D reconstructions

Image analysis is a vast topic that cannot be covered exhaustively here, and the interested reader might find supplemental material in numerous textbooks, see e.g. References [133–136] among others. We start with a brief list of available software programs (see Section 4.1). Then, a typical image processing workflow is sketched out: *i.* denoising (Section 4.2), *ii.* segmentation (Section 4.3), *iii.* clean-up (Section 4.4), *iv.* labelling (Section 4.5) and *v.* quantification (Section 4.6).

This workflow is by no means universal. For example, full-field measurement of the local kinematics is not covered here [65, 67, 137–142]. Furthermore, the present section is restricted to fairly classical techniques. In particular, graphs are not discussed, although they recently “*have emerged as a unified representation for the processing and the analysis of images. [...] This research topic is timely, very influential in computer science and has led to many applications in denoising, enhancement, restoration, and object extraction. Consequently, graphs have become indispensable for the development of cutting-edge research and applications in image processing and analysis.*” (quoted from the introduction to Reference [143]). Graph-based approaches fall well outside the scope of this paper and the interested reader is referred to Reference [143] (textbook) for a complete overview. It is the opinion of the authors that these techniques should be considered extremely seriously, despite the mathematical framework that may seem intimidating (see e.g. Reference [144] for an application to *power-watershed*).

Also, machine-learning approaches are not covered here, although they deliver promising results [145, 146].

4.1. Available software

In the present section, we list a few available software programs to carry out analysis/visualization tasks. This list is by no means exhaustive; it merely reflects the typical workflow of the authors and excludes commercial products.

Interactive tools. ImageJ³ is probably the most widely used interactive image analysis toolbox. It comes with a lot of standard tools out-of-the-box, and is extensible through a flexible plugin interface. Fiji⁴ is a “batteries-included” distribution of ImageJ, which is bundled with many popular third-party plugins. Unlike ImageJ, which is distributed under a permissive BSD license, it should be noted that Fiji is distributed under a GNU General Public License.

Libraries. For those willing to perform their analyses through a programming/scripting interface, several libraries are available. First, it is emphasized that ImageJ can be used as both an interactive tool and a library.

The Insight Toolkit (ITK)⁵ is a full-featured C++ library, initially developed for medical imaging. Its object-oriented architecture can be intimidating at times and SimpleITK⁶ offers a somewhat more accessible application programming interface (API) to ITK. It should be noted that both ITK and SimpleITK are C++ libraries with bindings for many other programming languages (including Python, C# and Java). Both are released under the Apache 2.0 License.

Finally, scikit-image⁷ [147] is a full-featured, community-driven Python image processing library that takes advantage of the flexible multi-dimensional array structure exposed by the NumPy⁸ library. It is released under a BSD license.

Visualization. ParaView⁹ [148], VisIt¹⁰ [149], VisNow¹¹ [150] and 3D Slicer¹² [151] are open-source, general purpose, interactive software programs for visualization of large, multi-dimensional datasets. ParaView, VisIt and 3D Slicer are released under a BSD license; VisNow is distributed under a GNU General Public License. Finally, Dragonfly¹³ is a commercial software that grants free-of-charge licenses to “*qualified researchers, academics, and non-commercial developers for non-profit research or development purposes*”. All these software programs allow for custom extensions through ad-hoc plugin systems.

4.2. Denoising

Even when the acquisition parameters are optimized for image quality, denoising is almost always required as a first step. This operation is also called improperly “noise removal”. In reality, noise is not *removed*; it is merely smoothed out, which

³<https://imagej.net/>, last retrieved 2019-06-19.

⁴<https://imagej.net/Fiji>, last retrieved 2019-06-19.

⁵<https://itk.org/>, last retrieved 2019-06-19.

⁶<http://www.simpleitk.org/>, last retrieved 2019-06-19.

⁷<http://scikit-image.org/>, last retrieved 2019-06-19.

⁸<http://www.numpy.org/>, last retrieved 2019-06-19.

⁹<https://www.paraview.org/>, last retrieved 2019-06-19.

¹⁰<https://wci.llnl.gov/simulation/computer-codes/visit>, last retrieved 2019-06-19.

¹¹<https://visnow.icm.edu.pl/>, last retrieved 2019-06-19.

¹²<http://www.slicer.org/>, last retrieved 2019-06-19.

¹³<http://www.theobjects.com/dragonfly/index.html>, last retrieved 2019-06-19.

generally affects the resolution of the image. There are numerous denoising techniques, and we only list a few of them (see e.g. Reference [152] for a more complete review).

Low-pass filtering is probably the most simple denoising procedure. Commonly used kernels are uniform (mean filter) and gaussian. The latter is backed by strong theoretical background based on the scale-space theory [153–156]. While simple, these filters are known to blur the image. In particular, edges are smoothed. *Median* [157] and *bilateral* [158] filtering are known to better preserve edges.

Nowadays, local, non-linear procedures are preferred over the previous approaches. *Anisotropic diffusion* is designed to smooth images preferably along directions of weak gradient [159]. Constrained minimization of the *total variation* is also extremely efficient for images that are expected to be blocky [160, 161]. In *block-matching 3D algorithms* (BM3D), images are modeled through nonlocal patches [162]. Finally, *non-local means* filtering [152] is known to preserve both edges and textures, owing to the fact that it performs weighted averages over *similar* pixels.

4.3. Segmentation of images

Segmentation refers to the process of classifying all voxels of the reconstructed image into a finite number of groups (typically: the material phases, voids, cracks, ...). Segmentation into two classes is usually called *binarization*, as it returns a binary (black-and-white) image from a gray-level input.

Note that segmentation relies on the strong assumption that the microstructure is *fully resolved*. In other words, each voxel represents a single phase. In many situations, the voxel size is greater than the characteristic size of the material features. This assumption thus fails to be true, and each voxel might be a mixture of many phases. The reconstructed volume is then truly a gray level, three-dimensional image, where the gray level of each voxel is related to its chemical composition. Recovering the chemical composition from this gray level would allow to bypass segmentation altogether (References [117] and [118] are early examples of such inverse analyses). This is a very active research area in x-ray CT, which requires accurate control of the spectrum of the source as well as refined models of the interaction between x-rays and matter. The recent advent of photon-counting detectors further opens new exciting perspectives [163–165].

Thresholding is the most simple segmentation procedure. In the case of binarization a threshold t is defined. All voxels with gray-level lower (resp. greater) than t are then affected to one class (resp. the other class). In order to ensure reproducibility and user-independence, it is preferable that the threshold be selected automatically. Many automatic threshold selection algorithms have been proposed [166, 167]. To cite but a few: Otsu's method [168], entropy-based methods [169–172] and mixture-modeling methods [173] are widely available in most image processing software programs and libraries. Alternatively, if the volume fraction of the various phases can be measured independently, the threshold(s) can be selected in order to ensure that the proportion of each segmented phase matches the expected value [142].

Figure 12: Owing to noise, the gray-levels histograms of air and aggregate overlap in the above 3D reconstruction of Hostun sand HN31. The threshold was selected so as to minimize the misclassification errors. (Reproduced from Reference [118], with permission.)

Thresholding is extremely simple and provides convincing results in many use-cases. As such, it should probably always be tested first on a new set of images; if the resulting segmentation is not satisfactory, then more advanced techniques may be used. However, the reader should keep in mind that thresholding will usually result in misclassification of some voxels. Indeed, owing to noise, the gray levels of each phase spread around a mean value. The tails of the gray-level distributions of various phases may overlap (see Figure 12), in which case the voxels whose gray-level belongs to the overlap region are undecidable. This is acknowledged by mixture-modeling approaches [173] that aim at minimizing the misclassification errors.

To overcome these shortcomings, topological or geometrical informations must be accounted for. In other words, classification of a specific voxel must be based on its gray level *and* the gray levels of its neighborhood. A straightforward extension is *local* thresholding [174], where, for each voxel, the threshold is found by analyzing the histogram of gray-levels in a neighborhood (rather than the whole image). In the same spirit, Stamati et al. [175], apply a threshold to the local *variance* of the gray levels.

Since their introduction by L. Grady [176], segmentation techniques using random walkers have been gaining in popularity. Although more involved computationally, they often result in very accurate segmentations, and should probably be considered as state-of-the-art.

4.4. Cleaning-up the segmented images

Once segmentation has been performed, it is usually necessary to clean-up the image, if only to remove isolated voxels. Standard tools of the mathematical morphology theory such as dilation, erosion, opening and closing are usually invoked for this task. The literature is very wide on this topic, and the reader is referred to e.g. the online course by J. Serra¹⁴ as well as references [177–179] (textbooks) and [180, 181] (review papers) for more details.

4.5. Labelling

Segmentation (see Section 4.3) delivers an image where each voxel belongs to one out of a user-defined number of classes (the material phases). In the present paper, identification of individual features within a specific phase is referred to as labelling. It should be noted that, although widely spread, this

¹⁴<http://cmm.enscm.fr/~serra/cours/>, last retrieved 2019-06-19.

terminology is not universally accepted. Labelling and segmentation are thus often collectively referred to as segmentation, although both tasks have different goals, and use different tools.

To illustrate this point, we consider a sample of fibre reinforced concrete. Binarization of its 3D image would result in a steel phase and a concrete phase. Therefore, at the end of the segmentation step, it is possible to check the overall fiber volume content, as well as its local fluctuations. However, it is essential to identify (label) each individual fiber to quantify their angular distribution.

Being application-dependent, labelling is usually the most difficult step of the whole image processing. In other words, there is no general strategy that works out-of-the-box for any images. Rather, the user must test different techniques until the desired result is obtained. The discussion is restricted here to connected components labelling and basins labelling through watershed.

Connected components labelling is a simple procedure that sometimes delivers surprisingly accurate results. In this approach, two neighbor voxels (6-, 18- or 26-connectivity) that belong to the same phase are attributed the same label. Of course, this approach fails to separate two objects that are in contact. Analysis of simple shape descriptors (principal moment of inertia, for example) might help identify these pathological cases, and develop a heuristics to split the objects that were unduly merged. It should be noted that most image processing software programs and libraries offer simple and efficient implementations of connected components labelling [182].

When connectivity analysis fails to discriminate the various features of the image, the *watershed* transform can be used [183, 184]. This method belongs to the wide class of *superpixel methods* (not discussed here), which can be quite effective at grouping pixels/voxels based on topology constraints and perceptual similarity [185]. In the watershed approach, a topography map is first constructed – typically: gradient of the original image or distance transform of the binarized image [186]. Then, this topography is “flooded”, and the features are the resulting catchment basins. Various algorithms have been proposed to compute the watershed transform efficiently [187, 188]; it is usually available in most image processing packages. Watershed usually results in over-segmented images, and the selection of appropriate markers (from which the flooding process is initiated) is critical [189, 190].

4.6. Quantification of the processed images

Quantification is the last step of the image analysis process, where figures are extracted from the image, which is then effectively considered as a measurement. Of course, the involved computations are extremely dependent on the nature of the information that is sought; we therefore only hint at a few classical analyses, many examples being cited in the remainder of this paper.

Volume fractions of the constituents are a direct product of the histogram of the image. The marching cube algorithm [191] delivers estimates of the specific surface areas. Spectral approaches (relying on the fast Fourier transform) can be used to

Not reproduced

Figure 13: 3D visualization of control mortar and mortar with the addition of expanded perlite (M-EP), expanded glass (M-EG) and cenospheres (M-CS). The largest pores are displayed in red, and the smallest in blue. (Reproduced from Reference [195], with permission.)

Not reproduced

Figure 14: XCT images of UHPFRC showing clear difference between steel fibres, voids and cementitious matrix, due to their significant difference in density and x-ray attenuation coefficient. (Reproduced from Reference [196], with permission.)

compute the two-point correlation functions. Once labelled, the size and shapes of individual features can be estimated through well-defined quantities, such as Feret diameters, principal moments of inertia, ... [192].

Finally, the segmented/labelled image may be used as the input geometry for a full-field computation (see Reference [193] among others for an application to linear elasticity).

B. RECENT APPLICATIONS OF X-RAY COMPUTED TOMOGRAPHY TO CEMENTITIOUS MATERIALS

5. What can you expect to see? Contrast is of the essence

It was realized as early as the late 1970s [28, 29] that x-ray CT carried immense potential for the investigation of cementitious materials. Nearly four decades later, the maturity reached by this imaging technique allows for quite advanced, *quantitative* applications, that go far beyond the mere *qualitative* visualization of the various constituents, as will be discussed in the remainder of this paper.

The crucial point that must be addressed when dealing with x-ray CT is the contrast within the various features of interest. Figure 8 shows that the contrast between the hydration products on the one hand, and air, water and steel on the other hand is quite high. Note that in Figure 8, the following typical composition of ordinary concrete was assumed (atomic number Z: fraction by weight): 1: 0.022100, 6: 0.002484, 8: 0.574930, 11: 0.015208, 12: 0.001266, 13: 0.019953, 14: 0.304627, 19: 0.010045, 20: 0.042951, 26: 0.006435 (see Reference [194], Table 2).

It results from the above discussion that x-ray CT is extremely well-suited to analyze the porous network or the distribution of steel reinforcement, as illustrated for example by Lanzón et al. [195] (see Figure 13) and Qsymah et al. [196] (see Figure 14). The former studied the modification of the pore size distribution in mortar induced by the addition of expanded perlite, while the latter analyzed the distribution of steel fibres in a sample of ultra-high performance concrete. Analysis of the porous network and of steel reinforcement will be discussed more thoroughly in Sections 6.1 and 6.2, respectively.

Hydration and degradation can also induce changes in the

contrast between the various phases of the cementitious matrix. x-ray CT has been successfully applied to the dynamic observation of hydration, as well as degradation of cementitious materials. Both of these applications will be discussed in detail in sections 7.1 and 7.2, respectively. Similar to air filled pores, air filled cracks can also be easily observed with x-ray CT, which led to the application of the method to study cracking of cementitious materials, covered in section 7.3.

Contrast (or rather, the lack of it) becomes an issue when a segmentation of fluid-filled pores is required. One possible cure when dealing with moisture penetration experiments is to use contrast enhancers mixed with the water to be absorbed. Examples include cesium chloride (see Reference [197] and Figure 15) and potassium iodide (see Reference [198]). In such cases, attention must be paid to the fact that chemical interactions might occur between the cement paste and the contrast agents, which might bias the observations. In the above cited papers, the samples were cured for 14 to 60 days before being submitted to water (+ contrast agent) imbibition. At this time, most of the hydration has already taken place, and chemical interactions may be neglected.

X-ray CT can also be combined with other techniques that are more sensitive to water, such as neutron tomography [199], or fast, Talbot interferometry-based multi-contrast x-ray micro-CT [200].

Contrast enhancers are also relevant when the distinction between aggregate and cementitious matrix needs to be highlighted. For example, Carrara et al. [201] used a small amount of baryte powder as a substitution to fine aggregates, which resulted in a better contrast and more reliable image segmentation. The authors also considered hematite substitution. However, hydration of the cement paste is strongly affected by hematite, which must therefore be discarded.

Contrast becomes an even greater challenge when aiming at distinguishing the various phases that form the cementitious matrix. The size of the corresponding features typically approaches the present spatial resolution limit of x-ray micro-CT, which makes the situation even worse, since one voxel might represent a mixture of several phases [202]. This led to the development of x-ray nano-CT, which is covered in more detail in section 8.

Finally, (“multispectral”) observations that combine multiple techniques have proved extremely helpful when attenuation contrast is too limited or when chemically-resolved images are desired. As a first example, micro-CT can be coupled with x-ray diffraction (XRD) in so-called “pencil-beam” x-ray diffraction tomography [203]; the 3D image is obtained from tomographic inversion of the x-ray diffraction (rather than attenuation) signal. Another example is non-destructive integrated CT-XRD instrument [204, 205], in which first the CT measurement is carried out followed by XRD targeting the ROI. Tomography Assisted Chemical Correlation (TACCo) enables simultaneous visualisation and chemical analysis of complex materials [206]. This technique combines x-ray micro-CT and electron probe microanalysis (EPMA) to produce 3D maps of the micro-structure and distribution of chemical constituents within tested materials. The combination of tomography and chemi-

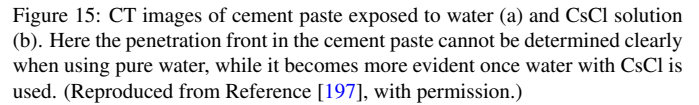


Figure 15: CT images of cement paste exposed to water (a) and CsCl solution (b). Here the penetration front in the cement paste cannot be determined clearly when using pure water, while it becomes more evident once water with CsCl is used. (Reproduced from Reference [197], with permission.)

cal or mineralogical analysis techniques has great potential to provide new insights on the degradation of concrete [207], by providing detailed information on the altered layers of concrete affected by carbonation, corrosion, leaching or sulphate attack.

6. Static observations

In the present section, we discuss *static* applications of micro-CT to cementitious materials. By “static”, we mean applications where only one snapshot of the sample is considered, possible evolutions of the microstructures being disregarded. We first discuss observations of well-contrasted features (pores and various non-cementitious inclusions) that are embedded in (but not part of) the cementitious matrix. The section closes on the more challenging quantification of the cementitious matrix itself.

6.1. Observation of well-contrasted features

The macroscopic properties of cementitious materials are controlled by the structure of their porous network, and many studies have been focused on the analysis of the porous network in relation with e.g. mechanical or durability macroscopic properties. The pore-size distribution typically ranges from a few tens of nanometres to few millimetres, which makes this investigation all the more challenging. Owing to the excellent resolution and contrast between air and cement paste, x-ray micro-CT is well-suited to characterize the three-dimensional structure of the porous network and extract various microstructural parameters such as total porosity, pore-size distribution, connectivity, tortuosity, ...

The contrast between air and hydration products results in images that can be readily segmented, and that allow for reliable estimation of microstructural parameters such as the pore-size distribution. As an example, Leite and Monteiro [208] used micro-CT to evaluate the influence of recycled aggregate preconditioning on the pore size distribution of new concrete (see Figure 16). X-ray micro-CT has been used to characterize: *i.* concrete samples cast with different w/c ratios [209], *ii.* systems containing different chemical [210–214] or mineral [195, 215–221] additions, *iii.* cementitious materials based on novel binders [5, 222–227]. Recently, the porosity of cement grains was also analysed using x-ray micro-CT [228].

X-ray micro-CT has also received a lot of attention in the field of cementitious materials containing additional engineered porosity, such as insulating materials [229–231], aerated cement paste [232], porous concrete [233, 234], [230] lightweight mortar containing polymer waste aggregates [235], foamed concrete [236, 237], alkali-activated foams [238, 239] (see Figure 17 as an example). The resulting 3D images have then been

Not reproduced

Figure 16: Micro-CT images of concrete prisms ($5500 \times 7500 \times 2100$ μm) showing the size and spatial distribution of the pores as well as the corresponding pore-size distributions. Samples are new concrete cast with aggregates recycled from high strength original concrete with various preconditioning (DRY – dry aggregate, SSD – saturated surface dry aggregate). (Reproduced from Reference [208], with permission.)

Not reproduced

Figure 17: Void distribution of the specimen insulating cement paste specimens with Aer solids depending on the void size: (a) voids with radius of 10–30 μm , (b) voids with radius of 30–50 μm , (c) voids with radius larger than 50 μm . (Reproduced from Reference [230], with permission.)

used to estimate macroscopic properties such as air permeability [229, 240] and thermal conductivity [236] of such porous cementitious materials.

Tomographic images can also provide information on the pore connectivity, pore spacing factor, tortuosity of pores and extent of percolation of the pore network [241–243]. For these purposes, mostly lower energies (15–25 keV) resulting in higher resolutions (0.5–1 μm), owing to the smaller focal spot size, were used. For the analysis of pore connectivity, after carrying out the pore segmentation and identification, the connected pore clusters are labelled. The output of the pore cluster labelling can be the number of pore clusters and their sizes, their coordinates and the distance between disconnected pores, which can be correlated with macroscopic permeability properties of cementitious materials. There has been an effort to additionally quantify pore connectivity [244], specified as the number of void voxels in the largest percolating pore cluster divided by the total number of void voxels in the VOI. Thus, a pore connectivity of 1.0 indicates that all void voxels in the segmented porosity are interconnected. Tortuosity of the pore network is usually estimated using random-walker simulation in the 3D pore space [245–249]. To perform the simulation, a random pore voxel is chosen as the initial position of each walker, the migration of which is confined exclusively to voxels that have been identified as pore space. The diffusion tortuosity is measured as the ratio of the self-diffusion of a walker in free space to the self-diffusion of a walker in the porous medium [247].

With the increase in computer power and the development of sophisticated models, we believe that there is great opportunity to simulate complex phenomena in the cementitious matrix, based on the pore microstructure obtained using x-ray micro-CT. Besides the already mentioned random walker simulations, examples of such applications can be found in References [250–252].

Micro-CT is often complemented with other techniques in order to investigate the smallest pores, that would otherwise remain undetected. An example of integration of MIP and CT can be seen in the work by Das et al. [5], where MIP was used to determine the pore-size distribution in the range of 0.0036 μm

Not reproduced

Figure 18: Distribution of pores obtained using MIP and micro CT on fly ash geopolymer paste. The figure shows that both techniques are complementary in terms of size of pores. (Reproduced from Reference [5], with permission.)

to 10 μm to complement the CT studies that probed sizes in the range of 0.74 μm to 50 μm .

CT application to porosity studies has challenges, such as the dependency of the pore structure parameters on the scan resolution [246, 253]. Gallucci et al. [253] reported that porosity and pore connectivity measured by micro-CT strongly depended on the voxel size (spatial resolution). Indeed, they showed that decreasing the voxel size (from 2.67 to 2, 1.34 and 0.67 μm) induced an increase of the calculated pore network connectivity (from 0 to 66 and 82 to 95 % respectively) and calculated porosity (from 5.03 to 6.63 and 11.48 to 18.6 % respectively). Opposing results were obtained by du Plessis et al. [254], who reported that the pore size distribution histograms in the region of overlap are similar regardless of resolution and duration of scanning. Their conclusion was based on an experimental program where the spatial resolution varied from 5 to 100 microns and the duration of scanning from 5 min to 1 h. They concluded that CT can be an efficient, simple and cost-effective tool for the analysis of pore size distribution and porosity calculation and visualisation, especially when large pores of interest and large batches of samples need to be compared.

Pore structure was also found to show significant variations along the test specimen, meaning that the results are depended on the chosen region of interest (ROI) [255]. Due to the inherent heterogeneity of pore structure within the sample of cementitious material, the parameters estimated are significantly affected by the number of traverse lines selected for a single section and the number of sectional images selected across the volume of specimens [256]. Therefore, care should be taken to identify ROI when comparing changes in porosity in dynamic scanning (scanning with time lapses) and to analyse a sufficient number of traverse lines and sectional images to obtain a representative and reliable value with low standard deviation.

Besides pores, x-ray micro-CT has been used to investigate the dispersion in the cementitious matrix of various features and additions that are embedded in modern concrete to enhance its properties and create high-performance materials: wood [257], steel [258, 259], polymer [260], PET [261] and carbon fibres [262–265], recycled aggregates [208], phase changing materials [266, 267], cenospheres [268], hemp particles [269], graphene oxide agglomerates [270, 271], waterborne epoxy resin [272], dense (unhydrated cement grains) and porous parts of cement matrix [273] and even features within Imperial Roman architectural mortar [274]. Again, the rather good contrast in density and x-ray linear attenuation between the features of interest and the surrounding cementitious matrix is what made their x-ray imaging possible.

Steel fibre reinforced concrete is a canonical example of such applications, owing to the excellent contrast between steel,

Not reproduced

Figure 19: X-CT observation of the distribution of steel fibres in fibre reinforced concrete. (a) steel fibres aligned using electro-magnetic field, (b) non-aligned steel fibres. (Reproduced from Reference [281], with permission.)

cementitious matrix and air, as illustrated in Figure 19. Microstructural parameters such as fibre volume fraction, distance between fibres and distribution of fibre orientations [275] can be extracted from the 3D images and correlated to the material performance [196, 276–279]. Herrmann et al. [280] propose a procedure based on the analysis of the Hessian matrix of the image to retrieve the fibers and their orientations. This is illustrated by Oesch et al. [275] who demonstrate how the casting procedure affects the angular distribution of fibres. More advanced applications include the visualization of the fracture surface and computation of the energy dissipated by cracking in fibre reinforced specimens [258].

Wood and synthetic fibres, are more difficult to resolve, because their low x-ray attenuation is similar to that of voids. Such fibres are often segmented by means of shape and size-based filters [282]. Hernández-Cruz et al. [260, 283] visualized the preferred orientation of synthetic fibres, the ASR gel formation, the preferred crack initiation sites, the crack propagation paths and the aggregate dissolution due to ASR. Beltran and Schlange [257] showed that the curvature of wood fibres correlates with the strength of the matrix.

Another application of static observations is imaging of single components of cementitious materials, such as cement or aggregate particles, in order to incorporate a more realistic description of their shape in numerical simulations. Conventional numerical simulations of the hydration reaction often assume a spherical cement particle, because of the inherent simplification in algorithm formulations and corresponding reduced computer time. There is a strong motivation to use tomographic images to develop realistic but still cost-effective particle shapes of cement [284–287] and aggregate [288–290] (see Figure 20). Tomographic analysis showed that surface area vs. volume of cement particles differs from that of a spherical grains, with cement particles tending to be prolate, i.e. with one dimension greater than the two others [291–293]. Since the shape of cement particles plays a significant role in the hydration process, differences between assumed and real cement particle shape can lead to significant differences between simulated and experimental hydration studies. In the work of Holzer et al. [292] on cement particle shape and their influence on modeling, x-ray micro-CT was used to examine the 3D shape of particles in the 20–60 μm sieve range. Focused ion beam nano-tomography was used to examine the 3D shape of cement particles found in the 0.4–2.0 μm , leading to a statistical particle analysis across the full size range.

6.2. Intra-matrix observations

Investigation of the cementitious matrix itself is motivated by a recent trend in the cement and concrete industry which

Not reproduced

Figure 20: Two views each of two cement particles: (a) equivalent spherical diameter of about 36 μm , (b) equivalent spherical diameter of the particle of about 15 μm . (Reproduced from Reference [284], with permission.)

Not reproduced

Figure 21: (Left) Grayscale image of the four primary hydration products in portland cement, synthesized in the laboratory and layered on top of each other: C-S-H gel, calcium hydroxide (CH), monosulfate (AFm) and ettringite (AFt). The contrast between all four phases is rather low. (Right) Histogram of the gray levels for each pure phase. (Reproduced from Reference [296], with permission.)

aims at controlling the macroscopic properties of cementitious materials by carefully tuning their microstructure. This is no mean feat owing to the complex, multi-phase [294] and multi-scale [205] nature of these materials. The Visible Cement Data Set [295] was an early attempt at making 3D data of Portland cement pastes freely available to the scientific community.

The various phases in a cementitious matrix [244] are usually identified on the basis of their gray level. However, the contrast between the various hydration products is usually very low. Deboodt et al. [296] performed a thorough methodological work to overcome the limitations caused by low contrast between the four primary hydrated phases in portland cement, namely: C–S–H, calcium hydroxide, monosulfate and ettringite. To do so, they imaged the pure phases as well as binary and quaternary mixtures of phases (see Figure 21). Based on the gray-level histogram of the pure phases, they quantified the composition of binary and quaternary mixtures, thus paving the way to quantitative phase characterization. For now, such approaches are limited to monochromatic (synchrotron) experiments, where beam hardening can be neglected.

7. Dynamic observations

The present section is devoted to *dynamic* applications of x-ray micro-CT to cementitious materials. By “dynamic”, we mean applications that account for microstructural changes over time. Real-time dynamic observations are still rather challenging, as they require fast (or ultra-fast) tomography facilities. However, for sufficiently slow evolutions, dynamic observations may be achieved by acquiring conventional scans at intervals of several days (months, years). Such dynamic applications are of course only possible because tomography is a non-destructive technique. Image registration is the process that

Not reproduced

Figure 22: Evolution of the gray-level histograms during hydration of OPC and CSA cement. Hydration products are identified by their gray scale value. (Reproduced from Reference [297], with permission.)

matches corresponding regions of interest in two or more three-dimensional images of the sample; it is a crucial step of the analysis of dynamic observations [298].

7.1. Hydration

Monitoring the hydration is probably the most obvious (but maybe not the most easily performed) application of dynamic x-ray micro-CT to cementitious materials.

x-ray micro-CT has offered a deeper insight into the hydration of cementitious materials. For example, it has been used to measure the amount of reacting anhydrous cement grains, to monitor changes in the porosity of the hydrating matrix [253, 299–301] and to reveal the spatial and temporal relationship between different paste components depending on the composition of the cementitious mix [202, 297, 302]. X-ray micro-CT can be coupled with other techniques or used to support their findings, e.g. ultrasonic pulse velocity (UPV) [303], non-contact electrical resistivity (NER) [303] and acoustic emission (AE) [20]. In most cases energies of around 10–15 keV were used in order to ensure the required resolution (below 1 μm).

Chotard et al. [20] suggested that hydration is a heterogeneous process that may start at the core of the sample, and spread towards its boundaries. Helfen et al. [304] were able to observe the nucleation of cracks induced by autogeneous shrinkage and to quantify the development of porosity with time. More recently, Gastaldi et al. [297] measured time evolving gray-level histograms that were then used to obtain information about the evolution of the hydration products of OPC and CSA cement (see Figure 22). Parissatto et al. [202] used the same method to quantify the evolution of hydrating cement systems with two different water-to-cement ratio. Wang et al. [298] scanned three different cement mixes during the first 28 days of the hydration process (scans were performed at 1, 7, 14, 21 and 28 days). This enabled them to follow changes in the 3D microstructure during hydration, such as filling of air voids and decrease in the amount of unreacted anhydrous cement particles.

Using an advanced topological analysis of the complex porous network (albeit at the scale of the resolution of the experiment), Levitz et al. [305] observed an apparent “depercolation” of the porous network between 83h and 150h of setting, while the measured electric conductivity did not vanish. These results indicate that the smallest (sub-micron) pores play a significant role on the transport properties of cementitious materials.

7.2. Durability-related observations

Besides the hydration process, evolution of the microstructure and the physico-chemical properties can be induced by interactions with the surrounding environment (e.g. exposure to climatic conditions). At the macro-scale, these alterations result in variations of strength, permeability, ion diffusion coefficient and pore structure [244], which can impact the durability of the structure. X-ray micro-CT allows the observation of such changes at the micro-scale. Various degradation processes are discussed below.

Not reproduced

Figure 23: Cross-section through three different pastes exposed to acetic acid (top row) and butyric acid (bottom row), with clearly visible layers of degradation. (Reproduced from Reference [314], with permission.)

Leaching/acid attack. Concrete leaching is often the result of a fluid attack (pure water or water with much lower pH than that of the pore solution), and leads to the hydrolysis of cement paste hydrates [306, 307]. The main consequence of concrete leaching is a porosity increase of the cement matrix; new pores are formed in the altered layer after dissolution of anhydrous cement minerals (C_2S , C_3S) or hydration products (C-S-H , ettringite and portlandite). Altered layers are visible using x-ray micro-CT through changes in porosity [244, 308–310], changes in x-ray linear attenuation coefficient between sound and leached matrix [306, 311–313, 313–316] or internal cracking and damage [317–319]. Dyer [314] used x-ray micro-CT to evaluate the influence of cement type on its resistance to organic (butyric, acetic) acids. The resulting images (see Figure 23) clearly show the existence of three zones: a darker outer zone in which decalcification of the paste is essentially complete, a zone beyond this where the process of decalcification is ongoing, and a lighter inner zone which is currently unaffected by acid attack. Differences in the resistance to acid in the case of binder with fly ash and CSA cement was also observed. It was also observed by Rougelot et al. [311] that leaching can result in a drastic reduction of the strength of the cementitious matrix which can in turn induce microcracking.

Additionally, increase of porosity and degree of pore connectivity in cement matrix in contact with water during electrochemically accelerated leaching test were observed using x-ray micro-CT and quantified using random walker simulations [308], while the modeling of the phenomena was further developed in Reference [310]. Based on the tomography data it was possible to establish a correlation between CaO/SiO_2 molar ratio and the diffusion tortuosity of degraded matrix, calculated using random walk simulation.

Corrosion. During corrosion of the reinforcement embedded in concrete, two processes occur concurrently: *i.* formation of a corrosion layer around the rebars and *ii.* formation of cracks. Dynamic x-ray micro-CT experiments were performed to monitor the thickness of the corrosion layer [320, 321], cracking of the cementitious matrix [322–324], for various types of steel [323, 325, 326] or mixes of concrete [327, 328]. Such observations are quantitative: for example, the corroded surface area can be estimated [329, 330].

The critical issue for such applications is to find the optimal beam energy that allows the beam to pass through the sample while minimizing artefacts around the steel reinforcement. Furthermore, owing to the high absorption coefficient of steel, it is usually necessary to reduce the diameter of the rebars down to small values that may be deemed unrealistic.

Despite these restrictions, x-ray micro-CT usually delivers images that can readily be analyzed, owing to the high contrast

Not reproduced

Not reproduced

Figure 24: 2-phase segmentation of the carbon steel (CS) and the ferritic stainless steel (FSS) samples at different times. The steel is in light gray, the propagating corrosion products are in orange, and the propagating cracks and the air voids are in dark gray. (Reproduced from Reference [325], with permission.)

Figure 26: Carbonation front depth evolution of the specimen with different additions of slag. (Reproduced from Reference [344], with permission.)

Not reproduced

Figure 25: a) Volume rendering collating 'ASR phenomena' (in red); b) rendering of voids with deposited ASR gel (light blue). (Reproduced from Reference [336], with permission.)

Work by Han et al. [340] showed how more advanced methods, such as SEM, nanoindentation and x-ray micro-CT can also be used to evaluate carbonation of concrete. In Reference [341], the x-ray attenuation method (XRAM) was used to compute the local calcium carbonate content and reveal the spatial distribution of CaCO_3 formed during carbonation from the comparison of scans of the sound and carbonated sample. It should be mentioned that accelerated carbonation is usually preferred, as natural carbonation is too slow a process for in-situ monitoring [342]. In the above-mentioned works, the values obtained through x-ray micro-CT are shown to agree with thermogravimetric analysis and quantitative carbonation profiles. X-ray micro-CT was also used to follow the evolution of carbonation-induced cracks [343] and other microstructural changes [340]. Figure 26 (reproduced from Reference [344]) shows how the carbonation depth increases with exposure times and the addition of blast furnace slag (BFS) in the binder. Additionally, many cracks caused by carbonation shrinkage can be observed.

between steel, corrosion products and concrete. This is illustrated on Figure 24, where steel is shown in light gray, cracks and voids in dark gray and corrosion products in orange. In this research, Itty et al. [325] compared how corrosion propagates for two types of reinforcing steel (CS: carbon steel — FSS: ferritic stainless steel). It was shown that corrosion occurs in general around the whole surface of CS rebars, while it is more local on one side of the rebar in the case of FSS.

X-ray micro-CT shines at dynamical evaluation of corroding samples: formation of cracks and their filling with corrosion products [320, 323]. The information is of crucial importance for modeling and predicting time to cracking of the concrete due to reinforcement corrosion [331].

Alkali-silica reaction. Chemical reactions may develop between siliceous minerals contained in aggregates and alkali and hydroxyls ions from the cement paste. An expansive alkali-silica gel forms as a result around the grains. It reaches the surface of the concrete structure through pop-outs and cracks [332].

X-ray micro-CT has been applied to alkali-silica degraded samples to observe changes in void volume and type [333–335], grain detachment owing to ASR gel rims [334] and spatial distribution of alkali-silica gel within the matrix [283]. In the work performed by Marinoni et al. [336], micro CT was coupled with synchrotron radiation micro x-ray diffraction to characterize ASR gel morphologically and crystallographically in situ at the microscale. The authors were able to observe ASR phenomena throughout the sample and analyse specific voids with deposited ASR gel, as shown in Figure 25. Finally, x-ray micro-CT can deliver validation data for complex, multi-physics models of ASR induced failure [337].

Carbonation. Calcium bearing phases, such as portlandite and C–S–H, react with carbon dioxide to form carbonates. Depending on the amount of available portlandite, carbonation is followed by the densification of the matrix microstructure in the case of OPC cements or coarsening of pore structure in the case of low pH binders [6, 338, 339]. The amounts of calcium bearing phases decomposed and carbonates formed are typically quantified through traditional methods such as thermogravimetric analysis and XRD. Such techniques may be combined with mercury intrusion porosimetry to measure changes in pore size distribution.

Self-healing. The development of cementitious materials that present the potential for self-healing is a very active area of research. Self-healing ability is usually achieved by introduction of substances that are inert in sound concrete, but can be triggered by some changes within the material. These changes include formation of cracks or decrease of pH value of the pore solution. Once triggered, these substances react with the cementitious matrix to form hydration products or carbonates that precipitate in the cracks. Penetration of fluids into the matrix is thus reduced.

Since the process involves filling of existing voids and cracks (that offer excellent contrast with the surrounding solid matrix), x-ray micro-CT is well suited to assessing the efficiency of self-healing substances [345–349]. Microcapsules are presently the favored vessel for these self-healing substances, be it polymers [350–353], calcium sulfoaluminate cement (CSA) [354] or corrosion inhibitors [355]. Figure 27 shows the healing efficiency of hydrogel with and without encapsulated bacterial spores [347]. In this study, x-ray micro-CT allowed Wang et al. to evaluate and compare the amount and distribution of precipitate formed during self-healing for all samples.

Exposition to extreme temperatures. During continuous cycles of freezing and thawing, water in capillary cavities and voids gets frozen and melted, thereby causing micro-cracking, spalling and scaling in the cementitious matrix. Similarly, concrete exposed to very high temperatures induced by fire undergoes changes in pore structure, loss in compressive strength, cracking and spalling. In both cases, x-ray micro-CT observations of the resulting microstructural alterations (damage) is fairly straightforward, since the objects that need to be visualised (cracks,

Not reproduced

Not reproduced

Figure 27: 3D rendered view of the spatial distribution of healing products (in yellow) in the reference mortar (R) and mortars with hydrogels (m-h: without encapsulated bacterial spores; m-HS: with encapsulated bacterial spores). The images clearly show that sample m-HS produced the largest amount of precipitate, which is mostly located in a thick surface layer. Mortar cylinders were manually cracked and exposed to wetting/drying cycles before scanning. (Reproduced from Reference [347], with permission.)

Not reproduced

Figure 28: Extraction of connected crack system from microtomographic images of mortar exposed to frost. The whole crack network is displayed in black in the left image, while the largest connected crack system is displayed in the right image. (Reproduced from Reference [363], with permission.)

larger pores, disintegration of the matrix) are in the micro-scale range. For freeze-thaw cycles, it is thus possible to evaluate micro-porosity changes [356–361], calculate crack tortuosity [362, 363] or feed a model of frost-induced micro-structural damage [364]. Concerning exposure to very high temperatures, x-ray micro-CT was used to observe fracture and changes in micro-porosity [365–370]. Figure 28 shows a 3D image of cracks and air voids within mortar exposed to frost [363].

7.3. Cracking

Understanding the mechanical response of cementitious materials, including creep, damage and cracking, and the complex relationship between the multi-scale microstructure and the macroscopic mechanical properties is a long standing scientific challenge that remains widely open. Load-induced cracking of concrete can be quantified by various techniques such as acoustic emissions (AE) [371], computer vision, digital speckle pattern interferometry (DSPI) and digital image correlation (DIC) [372]. x-ray micro-CT being again extremely well suited to the task [373].

In ex-situ experiments, cracking is induced in the sample outside the tomography facility. In this approach, the whole range of loadings is available, from simple compressive testing [374–378] to indentation [379], fracture testing [274, 380] and drying [381, 382].

Even though ex-situ experiments provide invaluable information, it is deemed preferable to perform in-situ imaging, if only to allow for multiple loading steps. In other words, the sample undergoes loading while tomographic data are acquired. Numerous loading devices have been developed, the main technical issue being the fact that the opaque components should not prevent imaging of the ROI. Although in-situ compression tests have been clearly favored in the literature [380, 383–389], bending tests [390, 391] and split test [392] are also possible. In an example by Skarzyński [391], x-ray micro-CT was coupled with digital image correlation to evaluate fracture in a wedge-splitting test. Data from x-ray micro-CT were used to visualise crack width distribution in concrete, as shown in Figure 29 and to analyse fibre orientation and pore structure within concrete reinforced with industrial and recycled steel fibres.

Figure 29: Micro-CT analysis of an in-situ wedge splitting test. The images show the crack width distribution in concrete samples reinforced with: a) industrial steel fibers and b) recycled steel fibers (right). (Reproduced from Reference [391], with permission.)

Characterization of cracks by x-ray micro-CT can be challenging, owing to the fact that the size of micro-cracks and micro-pores can be close to the spatial resolution. In a recent work, Chateau et al. [393] proposed an alternative approach, based on a new image subtraction technique that allows the detection of sub-voxel cracks. These authors claim an accuracy of about one tenth of a voxel.

X-ray micro-CT data obtained can be used to feed 3D simulations or mechanical models [394–402]. For such applications, having reliable data on the internal changes in the microstructure of concrete as a function of load level is of paramount importance for both calibration and validation of models.

C. CUTTING-EDGE TOMOGRAPHY

8. Nanotomography

The wide range of applications described in the previous sections clearly shows that x-ray micro-CT with spatial resolutions of up to a half-micron is a well-established and mature technique. However, the hierarchical porous structure of cementitious materials ranges from nanometer to macroscopic scale [403], and there is pressing demand for x-ray *nano*-CT, that offers resolutions well below the micron.

Before we discuss x-ray nano-CT, though, grating-based x-ray dark-field tomography should be mentioned. This technique takes advantage of the fact that the dark-field signal can provide sub-pixel information [404].

Nanotomography is still evolving but the progress achieved in the last decade has been remarkable. Note, however, that the requirement of using small sample size demands careful sample preparation and the often low-quality of the nano-CT data is still challenging. The quantification of the 3D morphology on length scales ranging from less than 10 nanometers to one micron can provide unique information on the transport properties and mechanical strength. Brisard et al. [405] reported the first 3D synchrotron soft x-ray nano-CT of cement paste with a 30 nm spatial resolution (see Figure 30) and were able to estimate the small angle-scattering spectrum from the power spectrum of the projection image. This direct application of the Fourier slice theorem was successfully validated with the morphological quantification of calcium silicate hydrates using soft x-ray ptychographic imaging [406], a new technique that will be presented later on. Note that soft (resp. hard) x-rays refer to x-rays with low (resp. high) energy. It is convenient to define the limits of the soft x-ray energy range as the carbon and sulfur K-edges (about 300 eV and 2500 eV, respectively).

Soft x-ray nano-CT was also used to characterize the nanoscale

Not reproduced

Figure 30: Left: x-ray nano-CT of a two-month-old Portland cement paste reconstructed from 101 projections spanning -50° to $+50^\circ$. The region of interest is about $2\ \mu\text{m}$; Right: computed small-angle scattering using the 3D reconstruction image shown on the left. In continuous black line: 3D spectral density of the gray-level field is used for the $I(q)$ computation. In dotted red line: 3D spectral density of a two-level structure obtained after a segmentation of the 3D gray-level image preserving the external envelop of the cluster. (Reproduced from Reference [405], with permission.)

Not reproduced

Figure 31: 3D Al-tobermorite crystal clusters in a relict lime clast. (a) typical XM transmission image obtained with 280 eV incident x-ray. (b) high-resolution nano-CT reconstruction obtained with 510 eV incident x-ray. (c) associated topological skeleton. (Reproduced from Reference [407], with permission.)

structure of Al-tobermorite clusters in ancient Roman concrete (see Reference [407] and Figure 31). The 3D image (Figure 31b) was obtained by reconstructing the transmission images taken at successive tilt angles. Experimentally, it is not possible to access all tilt angles and that leads to a case of limited angle nano-CT. Precise alignment of the images is critical for convergence of the reconstruction so gold beads were dispersed over the sample to provide fiduciary markers (see Figure 31a). To study the topology of the cluster, a three-dimensional skeleton graph (see Figure 31c), formed by vertexes and links, was generated from the nanotomographic image. The connectedness number¹⁵ $C \simeq 0.65$ for the cluster indicates a well-connected solid mass.

Provis et al. [408] did pioneering hard x-ray nano-CT to characterize the three-dimensional pore structure of the aluminosilicate geopolymer gel and to demonstrate the direct binding of geopolymer gel onto unreacted fly ash precursor particles (see Figure 32). Note that, unlike the limited angle tomography described previously, their technique allows for experimental measurements over the full 360° rotation.

Hu et al. [409] were able to integrate synchrotron-based x-ray nano-CT and nano x-ray fluorescence to obtain high-resolution 3D images containing detailed chemical information. Their approach was able to distinguish seven nano-inclusions with different chemical compositions within a single fly-ash particle. This technique was also successfully applied to the study of

¹⁵ $C = -(a - b)/a$, where a is the number of vertexes (isolated or not) and b is the number of links.

Not reproduced

Figure 32: Cross-section through the fly ash particle, showing the hollow fly ash cenosphere particle structure, inhomogeneous particle wall and aluminosilicate geopolymer gel attached. (Reproduced from Reference [408], with permission.)

Not reproduced

Figure 33: Comparison between 3D images obtained by experiments and by modeling. (A) particles on a tungsten needle at the beginning of the experiment; (B) hydrating system after 7 h. C_3S particles are shown in dark gray, tungsten needle in light gray and hydration products transparent; (C) simulation of the particles shown in (A); (D) entire volume of simulated hydration product after 7 h shown in transparent gray; (E) distribution of simulated C–S–H (transparent gray) and $\text{Ca}(\text{OH})_2$ (light green) after 7 h. (Reproduced from Reference [412], with permission.)

early hydration of triclinic C_3S [410, 411] and the results provided new insights on the rate of reaction and morphology of the early hydration products.

A recent paper by Bullard et al. [412] shows the great potential of integrating high-performance computing and the synchrotron experimental of early hydration of C_3S . Figure 33 compares the solid phase volume fractions, spatial distribution and morphology of the hydration products obtained by the modeling and the experimental results.

There is great interest to study the topology of the hydration products, particularly C–S–H, in the range of $1 - 100\ \text{nm}$. Progress towards the development of Fresnel lenses capable of producing spatial resolution of a few nanometers [413] has been slow so the use of coherent lensless x-ray imaging, or Coherent Diffraction Imaging (CDI) becomes very attractive (Chapman and Nugent [414] give a good introduction to this approach). Fast developments in CDI led to great progress in solving the “phase problem” created by the fact that CCD detectors or photographic only measure the intensity of the light so the phase information is lost. Phase retrieval methods have been developed to recover the phase information from data containing only intensity information. These methods mainly use Fourier transform-based iterative algorithms that converge to a real-space image containing both the phase and intensity information.

The advances in CDI and traditional scanning transmission microscopy (STXM) were combined to create x-ray ptychographic microscopy. The mathematical formulation of ptychography is complex so for interested reader we recommend: *i.* a comprehensive review (up to 2008) by Rodenburg [415] and the early developments of Hoppe [416], the pioneer in the field, *ii.* the book of Zheng [417] on Fourier Ptychographic Imaging that contains many MATLAB® routines to illustrate the formulations and *iii.* a recent review of x-ray ptychography by Pfeiffer [418].

The first studies of ptychography imaging of cements were reported by Trtik et al. [419] using hard x-rays and Bae et al. [406] using soft x-rays. Silva et al. [420] presented a careful study of 3D nano-CT using ptychography to determine the spatially resolved mass density and water content of the C–S–H in a cement paste (Figure 34). This technique was also used successfully to characterize the in-situ hydration of Ye’elimite [421] and the chemistry and mass density of aluminum hydroxide gel in eco-cements [422].

Not reproduced

Figure 34: (a) phase contrast and (b) absorption images of a hydrated cement paste. UN: Unhydrated C3S; CH: calcium hydroxide; C-S-H: calcium silicate hydrate; Q: quartz capillary; and W: pore solution. (c) 3D images of phases in the hydrated cement paste. (Reproduced from Reference [420], with permission.)

9. Challenges and opportunities

Our review of more than 400 papers shows that many applications of x-ray micro-CT to cementitious materials can now be considered as routine experiments, in the sense that they are performed within a fairly standard x-ray micro-CT facility and do not require advanced sample preparation nor image processing techniques. In this section, we first select a few papers that best illustrate these routine applications, and then hint at some challenges that we believe x-ray micro-CT will have to face in the coming years, such as: ultra-fast experiments, gray-level imaging, coupling with other characterization techniques, and making the best out of the large amounts of generated data.

Static imaging of well-contrasted features (pores, steel fibres) was first performed about two decades ago [222, 383] and is nowadays fairly standard. The challenge in this area is now to go beyond the production of pretty images and carry out *quantitative* analyses to extract microstructural parameters or even simulate physical processes. Such advanced applications were illustrated by Promentilla et al. [245, 246] (tortuosity of pore network) or Ponikiewski et al. [277] (distribution of steel fibres).

Cementitious materials evolve in time (owing to the hydration process itself and various degradations induced by the surrounding environment). Monitoring this evolution usually requires non-destructive techniques such as x-ray micro-CT. As illustrated above, dynamic observations have already been performed (see the remarkable works of e.g. Gallucci et al. [253] for hydration; Bentz et al. [423] for degradation by sulfate attack; Han et al. [424] for carbonation). However, we do believe that x-ray micro-CT has not yet revealed its full potential in this area and will continue to deliver spectacular advances in the years to come.

In particular, there is a strong motivation for acquiring ultra-fast in-situ data of cement hydration with very high spatial resolution. Currently, the time resolution is around 20 seconds per square micron with a 10 nm spatial resolution; however, the development of faster detectors coupled with improvements in robust data analysis can make such ultra-fast experiments a reality.

Gray level imaging, by which we mean: analysing quantitatively (in terms of chemical composition, local porosity, ...) the gray level of each single voxel of the 3D reconstruction is also a topic with immense potential. For cementitious materials, a first step has recently been made by Deboodt et al. [296].

John Donne wrote in 1624 that “No Man is an Island”. Likewise, x-ray micro-CT is part of a whole range of characterization techniques that ought to be cross-correlated. The com-

plex cement hydration reactions produce a hierarchical material that develops over many time scales, with a microstructure that also spans several orders of magnitude in length scales. One single characterization technique cannot possibly cover such large ranges and there is a need to combine the data obtained from various techniques across different length- and time-scales in order to deliver a synergetic description of cementitious materials. From this perspective, it is necessary to ensure that sufficient overlap exists between the various characterization techniques involved. For example, there has been for a long time a gap between TEM nanoscale imaging and x-ray micro-CT microscale imaging. Owing to recent developments, we believe that ptychography might provide the missing link between these two essential characterization techniques, while also providing chemical distributions not otherwise available [19].

Even though the use of chemical admixtures, such as air-entraining and superplasticizers, is prevalent in a modern concrete mixture proportion, how they are incorporated into the cement hydration products is still poorly understood. Using the C 1s-edge in a soft x-ray scanning transmission x-ray microscope, it is possible to combine ptychographic imaging and computed spectro-tomography to image the 3D morphology of the hydration products and the oxidation states of the organic molecules as they interact with inorganic products. Special care should be taken to avoid radiation damage, so the use of a cryo-stage is highly recommended.

Finally, x-ray micro-CT and cementitious materials fit perfectly in our Big Data era. Indeed, over the last two decades, x-ray micro-CT has become main stream in the field of cementitious materials and each tomography experiment that is reported in the literature generates large datasets. As a consequence, in total, a huge amount of data is now available. This data is often collected for very specific needs, which means that most of the information that it contains remains to be exploited. Sharing this data across various laboratories would allow for further analysis by other groups; naturally the researchers that initially produced the data would have to be properly credited. Clearly, there is a need for *i.* a global, comprehensive repository of cement and concrete 3D images and *ii.* application of data mining and machine learning techniques to the resulting datasets.

Regarding item *i.*, NASA has already set up a database¹⁶ that stores the metadata of available datasets, including how to access these datasets. Regarding item *ii.*, Pelt and Sethian [425] have recently developed a powerful mixed-scale dense convolutional neural network, which significantly improved on traditional image-processing neural networks. The proposed scheme is easy to train and requires few parameters. Although the method has only been applied to 2D images and small collections of slices through 3D images, it has great potential to be successfully used in the complex segmentation and labeling of concrete containing various phases (ie, pores, lightweight aggregate, microcracks, cracks, fibers).

¹⁶<https://data.nasa.gov/>, last retrieved 2019-06-19.

Conclusion

The present review shows that, in the last 15 to 20 years, x-ray computed tomography has become a *de facto* tool for non-destructive imaging of cementitious materials. The technique is routinely used to e.g. *i.* analyse the microstructure: 3D geometry of the porous network, spatial distribution of phases, angular distribution of steel reinforcement (fibers), or *ii.* monitor the evolution of mechanical and chemical damage: cracking and degradation through leaching, alkali-silica reaction, carbonation, It should be emphasized that in most cases, the resulting 3D images can –and in our view, should always– be analysed *quantitatively*; in other words, a tomography experiment delivers a *measurement*, rather than a mere (albeit attractive) image.

X-ray computed tomography must face in the coming years a few exciting challenges. Improvements of the spatial resolution are of course always welcome, considering the multiscale nature of cementitious materials. Time resolution has also recently received a lot of attention, and we believe that

developments would undoubtedly offer a new perspective on such problems as hydration of the cement paste, or creep of the cementitious matrix. We also have high hopes regarding 3D chemical mapping.

X-ray computed tomography is known for generating a large amount of data. This will only get worse with time- and chemically-resolved experiments, which deliver 4D and multispectral images, respectively. Processing this data is a task that should not be overlooked, and for which innovative computational techniques such as machine-learning will probably play a key role.

Acknowledgements

Paulo J.M. Monteiro acknowledges the financial support given by the National Research Foundation-Prime Minister's office, Republic of Singapore through a grant to the Berkeley Education Alliance for Research in Singapore (BEARS) for the Singapore-Berkeley Building Efficiency and Sustainability in the Tropics (SinBerBEST) Program.

The authors would like to thank Edward Andò, Camille Chateau and Simo A. Mäkiharju for their insightful comments on early drafts of the manuscript.

References

- [1] K. L. Scrivener, Backscattered electron imaging of cementitious microstructures: understanding and quantification, *Cement and Concrete Composites* 26 (8) (2004) 935–945. doi:10.1016/j.cemconcomp.2004.02.029.
- [2] I. Richardson, Tobermorite/jennite- and tobermorite/calcium hydroxide-based models for the structure of C-S-H: applicability to hardened pastes of tricalcium silicate, β -dicalcium silicate, Portland cement, and blends of Portland cement with blast-furnace slag, metakaolin, or silica fume, *Cement and Concrete Research* 34 (9) (2004) 1733–1777. doi:10.1016/j.cemconres.2004.05.034.
- [3] M. Head, N. Buenfeld, Confocal imaging of porosity in hardened concrete, *Cement and Concrete Research* 36 (5) (2006) 896–911. doi:10.1016/j.cemconres.2005.06.006.
- [4] J. Zhou, G. Ye, K. van Breugel, Characterization of pore structure in cement-based materials using pressurization–depressurization cycling mercury intrusion porosimetry (PDC-MIP), *Cement and Concrete Research* 40 (7) (2010) 1120–1128. doi:10.1016/j.cemconres.2010.02.011.
- [5] S. Das, P. Yang, S. S. Singh, J. C. Mertens, X. Xiao, N. Chawla, N. Neithalath, Effective properties of a fly ash geopolymer: Synergistic application of X-ray synchrotron tomography, nanoindentation, and homogenization models, *Cement and Concrete Research* 78 (2015) 252–262. doi:10.1016/j.cemconres.2015.08.004.
- [6] M. Auroy, S. Poyet, P. Le Bescop, J.-M. Torrenti, T. Charpentier, M. Moskura, X. Bourbon, Impact of carbonation on unsaturated water transport properties of cement-based materials, *Cement and Concrete Research* 74 (2015) 44–58. doi:10.1016/j.cemconres.2015.04.002.
- [7] Q. Zeng, K. Li, T. Fen-chong, P. Dangla, Pore structure characterization of cement pastes blended with high-volume fly-ash, *Cement and Concrete Research* 42 (1) (2012) 194–204. doi:10.1016/j.cemconres.2011.09.012.
- [8] S. Tang, Z. He, X. Cai, R. Cai, W. Zhou, Z. Li, H. Shao, T. Wu, E. Chen, Volume and surface fractal dimensions of pore structure by NAD and LT-DSC in calcium sulfoaluminate cement pastes, *Construction and Building Materials* 143 (2017) 395–418. doi:10.1016/j.conbuildmat.2017.03.140.
- [9] L. Alarcon-Ruiz, G. Platret, E. Massieu, A. Ehrlicher, The use of thermal analysis in assessing the effect of temperature on a cement paste, *Cement and Concrete Research* 35 (3) (2005) 609–613. doi:10.1016/j.cemconres.2004.06.015.
- [10] C. Meral, C. J. Benmore, P. J. M. Monteiro, The study of disorder and nanocrystallinity in C–S–H, supplementary cementitious materials and geopolymers using pair distribution function analysis, *Cement and Concrete Research* 41 (7) (2011) 696–710. doi:10.1016/j.cemconres.2011.03.027.
- [11] D. L. Rayment, A. J. Majumdar, The composition of the C-S-H phases in portland cement pastes, *Cement and Concrete Research* 12 (6) (1982) 753–764. doi:10.1016/0008-8846(82)90039-4.
- [12] K. Shomglin, L. Turanli, H. R. Wenk, P. J. M. Monteiro, G. Sposito, The effects of potassium and rubidium hydroxide on the alkali–silica reaction, *Cement and Concrete Research* 33 (11) (2003) 1825–1830. doi:10.1016/S0008-8846(03)00204-7.
- [13] J.-P. Korb, L. Monteilhet, P. McDonald, J. Mitchell, Microstructure and texture of hydrated cement-based materials: A proton field cycling relaxometry approach, *Cement and Concrete Research* 37 (3) (2007) 295–302. doi:10.1016/j.cemconres.2006.08.002.
- [14] A. Valori, P. J. McDonald, K. L. Scrivener, The morphology of C–S–H: Lessons from 1h nuclear magnetic resonance relaxometry, *Cement and Concrete Research* 49 (2013) 65–81. doi:10.1016/j.cemconres.2013.03.011.
- [15] Y. Wang, Q. Yuan, D. Deng, T. Ye, L. Fang, Measuring the pore structure of cement asphalt mortar by nuclear magnetic resonance, *Construction and Building Materials* 137 (2017) 450–458. doi:10.1016/j.conbuildmat.2017.01.109.
- [16] B. Zhou, S. Komulainen, J. Vaara, V.-V. Telkki, Characterization of pore structures of hydrated cements and natural shales by 129 Xe NMR spectroscopy, *Microporous and Mesoporous Materials* 253 (2017) 49–54. doi:10.1016/j.micromeso.2017.06.038.
- [17] A. J. Allen, Characterization of Ceramics by X-Ray and Neutron Small-Angle Scattering, *Journal of the American Ceramic Society* 88 (6) (2005) 1367–1381. doi:10.1111/j.1551-2916.2005.00463.x.
- [18] A. J. Allen, J. J. Thomas, H. M. Jennings, Composition and density of nanoscale calcium–silicate–hydrate in cement, *Nature Materials* 6 (4) (2007) 311–316. doi:10.1038/nmat1871.
- [19] G. Geng, R. J. Myers, Y.-S. Yu, D. A. Shapiro, R. Winarski, P. E. Levitz, D. A. L. Kilcoyne, P. J. M. Monteiro, Synchrotron X-ray nanotomographic and spectromicroscopic study of the tricalcium aluminate hydration in the presence of gypsum, *Cement and Concrete Research* 111 (2018) 130–137. doi:10.1016/j.cemconres.2018.06.002.
- [20] T. Chotard, A. Smith, M. Boncoeur, D. Fargeot, C. Gault, Characterisation of early stage calcium aluminate cement hydration by combination of non-destructive techniques: acoustic emission and X-ray tomography, *Journal of the European Ceramic Society* 23 (13) (2003) 2211–2223.

- doi:10.1016/S0955-2219(03)00082-7.
- [21] M. Kemerink, T. J. Dierichs, J. Dierichs, H. J. Huynen, J. E. Wildberger, J. M. A. van Engelsen, G. J. Kemerink, Characteristics of a First-Generation X-Ray System, *Radiology* 259 (2) (2011) 534–539. doi:10.1148/radiol.11101899.
- [22] J. Hsieh, *Computed Tomography Principles, Design, Artifacts, and Recent Advances*, 2nd Edition, SPIE and John Wiley & Sons, Inc., 2009.
- [23] P. Mercier, André Bocage et la tomographie ou la vie d'un homme qui aurait dû être illustre, *Histoire des sciences médicales XXXII* (2) (1998) 169–173.
- [24] B. Pollak, Experiences with Planography, *CHEST* 24 (6) (1953) 663–669. doi:10.1378/chest.24.6.663.
- [25] J. Radon, Über die Bestimmung von Funktionen durch ihre Integralwerte längs gewisser Mannigfaltigkeiten, *Berichte über die Verhandlungen der Königlich-Sächsischen Gesellschaft der Wissenschaften zu Leipzig. Mathematisch-Physische Klasse* 69 (1917) 262–277.
- [26] R. N. Bracewell, Strip Integration in Radio Astronomy, *Australian Journal of Physics* 9 (2) (1956) 198–217. doi:10.1071/ph560198.
- [27] G. N. Hounsfield, Computerized transverse axial scanning (tomography): Part 1. Description of system, *The British Journal of Radiology* 46 (552) (1973) 1016–1022. doi:10.1259/0007-1285-46-552-1016.
- [28] I. L. Morgan, H. Ellinger, R. Klinskiak, J. N. Thompson, Examination of Steel and Concrete by Computerized Tomography, *Metal Construction* 2 (1979) 115–123. doi:10.14359/6987.
- [29] I. L. Morgan, H. Ellinger, R. Klinskiak, J. N. Thompson, Examination of Concrete by Computerized Tomography, *Journal of the American Concrete Institute* 77 (1) (1980) 23–27. doi:10.14359/6987.
- [30] A. C. Kak, M. Slaney, *Principles of Computerized Tomographic Imaging*, IEEE Press, New York, NY, USA, 1988.
- [31] J. Banhart (Ed.), *Advanced Tomographic Methods in Materials Research and Engineering*, Monographs on the Physics and Chemistry of Materials, Oxford University Press, Oxford, New York, 2008.
- [32] T. M. Buzug, *Computed Tomography: From Photon Statistics to Modern Cone-Beam CT*, Springer-Verlag Berlin Heidelberg, 2008.
- [33] S. Stock, R., *Microcomputed Tomography — Methodology and Applications*, CRC Press, Boca Raton, 2009.
- [34] S. Carmignato, W. Dewulf, R. Leach (Eds.), *Industrial X-Ray Computed Tomography*, Springer International Publishing, 2018.
- [35] R. A. Ketcham, W. D. Carlson, Acquisition, optimization and interpretation of X-ray computed tomographic imagery: applications to the geosciences, *Computers & Geosciences* 27 (4) (2001) 381–400. doi:10.1016/S0098-3004(00)00116-3.
- [36] V. Cnudde, M. N. Boone, High-resolution X-ray computed tomography in geosciences: A review of the current technology and applications, *Earth-Science Reviews* 123 (2013) 1–17. doi:10.1016/j.earscirev.2013.04.003.
- [37] E. Maire, P. J. Withers, Quantitative X-ray tomography, *International Materials Reviews* 59 (1) (2014) 1–43. doi:10.1179/1743280413Y.000000023.
- [38] B. L. Henke, E. M. Gullikson, J. C. Davis, X-Ray Interactions: Photoabsorption, Scattering, Transmission, and Reflection at $E = 50$ –30,000 eV, $Z = 1$ –92, *Atomic Data and Nuclear Data Tables* 54 (2) (1993) 181–342. doi:10.1006/adnd.1993.1013.
- [39] D. J. De Rosier, A. Klug, Reconstruction of Three Dimensional Structures from Electron Micrographs, *Nature* 217 (5124) (1968) 130–134. doi:10.1038/217130a0.
- [40] M. Magnusson, P. E. Danielsson, P. Edholm, Artefacts and remedies in direct Fourier tomographic reconstruction, in: *Nuclear Science Symposium and Medical Imaging Conference*, IEEE, Orlando, FL, USA, 1992, pp. 1138–1140 vol.2. doi:10.1109/NSSMIC.1992.301056.
- [41] K. Fourmont, Non-Equispaced Fast Fourier Transforms with Applications to Tomography, *Journal of Fourier Analysis and Applications* 9 (5) (2003) 431–450. doi:10.1007/s00041-003-0021-1.
- [42] F. Natterer, Fourier reconstruction in tomography, *Numerische Mathematik* 47 (3) (1985) 343–353. doi:10.1007/BF01389583.
- [43] P. R. Edholm, G. T. Herman, Linograms in Image Reconstruction from Projections, *IEEE Transactions on Medical Imaging* 6 (4) (1987) 301–307. doi:10.1109/TMI.1987.4307847.
- [44] P. R. Edholm, G. T. Herman, D. A. Roberts, Image reconstruction from linograms: implementation and evaluation, *IEEE Transactions on Medical Imaging* 7 (3) (1988) 239–246. doi:10.1109/42.7788.
- [45] D. Potts, G. Steidl, New Fourier reconstruction algorithms for computerized tomography, in: *Proceedings of the SPIE*, Vol. 4119, SPIE, San Diego, CA, United States, 2000, pp. 13–23. doi:10.1117/12.408606.
- [46] S. De Francesco, A. Silva, NUFFT-based Direct Fourier methods and regional tomography, in: *Proceedings of the 14th Annual Scientific Conference on Web Technology, New Media Communications and Telematics Theory Methods, Tools and Applications Medical Imaging and D-TV (EUROMEDIA 2008)*, 2008, pp. 118–122.
- [47] G. N. Ramachandran, A. V. Lakshminarayanan, Three-dimensional Reconstruction from Radiographs and Electron Micrographs: Application of Convolutions instead of Fourier Transforms, *Proceedings of the National Academy of Sciences of the United States of America* 68 (9) (1971) 2236–2240.
- [48] L. A. Shepp, B. F. Logan, The Fourier reconstruction of a head section, *IEEE Transactions on Nuclear Science* 21 (3) (1974) 21–43. doi:10.1109/TNS.1974.6499235.
- [49] G. Pratz, L. Xing, GPU computing in medical physics: A review, *Medical Physics* 38 (5) (2011) 2685–2697. doi:10.1118/1.3578605.
- [50] R. Gordon, R. Bender, G. T. Herman, Algebraic Reconstruction Techniques (ART) for three-dimensional electron microscopy and X-ray photography, *Journal of Theoretical Biology* 29 (3) (1970) 471–481. doi:10.1016/0022-5193(70)90109-8.
- [51] M. Beister, D. Kolditz, W. A. Kalender, Iterative reconstruction methods in X-ray CT, *Physica Medica* 28 (2) (2012) 94–108. doi:10.1016/j.ejmp.2012.01.003.
- [52] F. Xu, K. Mueller, A comparative study of popular interpolation and integration methods for use in computed tomography, in: *Proceedings of the 3rd IEEE International Symposium on Biomedical Imaging: Nano to Macro*, IEEE, Arlington, VA, USA, 2006, pp. 1252–1255. doi:10.1109/ISBI.2006.1625152.
- [53] G. T. Herman, A relaxation method for reconstructing objects from noisy X-rays, *Mathematical Programming* 8 (1) (1975) 1–19. doi:10.1007/BF01580425.
- [54] P. Gilbert, Iterative methods for the three-dimensional reconstruction of an object from projections, *Journal of Theoretical Biology* 36 (1) (1972) 105–117. doi:10.1016/0022-5193(72)90180-4.
- [55] A. H. Andersen, A. C. Kak, Simultaneous Algebraic Reconstruction Technique (SART): A superior implementation of the ART algorithm, *Ultrasonic Imaging* 6 (1) (1984) 81–94. doi:10.1016/0161-7346(84)90008-7.
- [56] J. A. Scales, Tomographic inversion via the conjugate gradient method, *Geophysics* 52 (2) (1987) 179–185. doi:10.1190/1.1442293.
- [57] E. L. Piccolomini, F. Zama, The conjugate gradient regularization method in Computed Tomography problems, *Applied Mathematics and Computation* 102 (1) (1999) 87–99. doi:10.1016/S0096-3003(98)10007-3.
- [58] R. J. Santos, Preconditioning conjugate gradient with symmetric algebraic reconstruction technique (ART) in computerized tomography, *Applied Numerical Mathematics* 47 (2) (2003) 255–263. doi:10.1016/S0168-9274(03)00056-4.
- [59] E. Y. Sidky, X. Pan, Image reconstruction in circular cone-beam computed tomography by constrained, total-variation minimization, *Physics in Medicine and Biology* 53 (17) (2008) 4777. doi:10.1088/0031-9155/53/17/021.
- [60] Y. Teng, S. Qi, D. Xiao, L. Xu, J. Li, Y. Kang, A General Solution to Least Squares Problems with Box Constraints and Its Applications, *Mathematical Problems in Engineering* 2016 (2016) 3934872. doi:10.1155/2016/3934872.
- [61] W. Xu, K. Mueller, Evaluating popular non-linear image processing filters for their use in regularized iterative CT, in: *Nuclear Science Symposium Conference Record (NSS/MIC)*, IEEE, Knoxville, TN, USA, 2010, pp. 2864–2865. doi:10.1109/NSSMIC.2010.5874318.
- [62] K. J. Batenburg, J. Sijbers, DART: A Practical Reconstruction Algorithm for Discrete Tomography, *IEEE Transactions on Image Processing* 20 (9) (2011) 2542–2553. doi:10.1109/TIP.2011.2131661.
- [63] S. Roux, H. Leclerc, F. Hild, Efficient Binary Tomographic Reconstruction, *Journal of Mathematical Imaging and Vision* 49 (2) (2014) 335–351. doi:10.1007/s10851-013-0465-0.
- [64] G. R. Myers, A. M. Kingston, T. K. Varslot, M. L. Turner, A. P. Shep-

- pard, Dynamic tomography with a priori information, *Applied Optics* 50 (20) (2011) 3685–3690. doi:10.1364/AO.50.003685.
- [65] H. Leclerc, S. Roux, F. Hild, Projection Savings in CT-based Digital Volume Correlation, *Experimental Mechanics* 55 (1) (2014) 275–287. doi:10.1007/s11340-014-9871-5.
- [66] T. Taillandier-Thomas, S. Roux, F. Hild, Soft Route to 4d Tomography, *Physical Review Letters* 117 (2) (2016) 025501. doi:10.1103/PhysRevLett.117.025501.
- [67] M. H. Khalili, S. Brisard, M. Bornert, P. Aimeidieu, J.-M. Pereira, J.-N. Roux, Discrete Digital Projections Correlation: A Reconstruction-Free Method to Quantify Local Kinematics in Granular Media by X-ray Tomography, *Experimental Mechanics* 57 (6) (2017) 819–830. doi:10.1007/s11340-017-0263-5.
- [68] H. Tuy, An Inversion Formula for Cone-Beam Reconstruction, *SIAM Journal on Applied Mathematics* 43 (3) (1983) 546–552. doi:10.1137/0143035.
- [69] D. Finch, Cone Beam Reconstruction with Sources on a Curve, *SIAM Journal on Applied Mathematics* 45 (4) (1985) 665–673. doi:10.1137/0145039.
- [70] L. A. Feldkamp, L. C. Davis, J. W. Kress, Practical cone-beam algorithm, *Journal of the Optical Society of America A* 1 (6) (1984) 612–619. doi:10.1364/JOSA.A.1.000612.
- [71] A. Katsevich, Theoretically Exact Filtered Backprojection-Type Inversion Algorithm for Spiral CT, *SIAM Journal on Applied Mathematics* 62 (6) (2002) 2012–2026, articleType: research-article / Full publication date: Jul. - Aug., 2002 / Copyright © 2002 Society for Industrial and Applied Mathematics. doi:10.2307/3648749.
- [72] A. Katsevich, Analysis of an exact inversion algorithm for spiral cone-beam CT, *Physics in Medicine and Biology* 47 (15) (2002) 2583. doi:10.1088/0031-9155/47/15/302.
- [73] F. Noo, J. Pack, D. Heuscher, Exact helical reconstruction using native cone-beam geometries, *Physics in Medicine and Biology* 48 (23) (2003) 3787. doi:10.1088/0031-9155/48/23/001.
- [74] H. Kudo, T. Suzuki, E. A. Rashed, Image reconstruction for sparse-view CT and interior CT—introduction to compressed sensing and differentiated backprojection, *Quantitative Imaging in Medicine and Surgery* 3 (3) (2013) 147–161. doi:10.3978/j.issn.2223-4292.2013.06.01.
- [75] A. Kyrieleis, V. Titarenko, M. Ibson, T. Connolley, P. Withers, Region-of-interest tomography using filtered backprojection: assessing the practical limits, *Journal of Microscopy* 241 (1) (2011) 69–82. doi:10.1111/j.1365-2818.2010.03408.x.
- [76] P. Paleo, M. Desvignes, A. Miron, A practical local tomography reconstruction algorithm based on a known sub-region, *Journal of Synchrotron Radiation* 24 (1) (2017) 257–268. doi:10.1107/S1600577516016556.
- [77] F. Noo, R. Clackdoyle, J. D. Pack, A two-step Hilbert transform method for 2d image reconstruction, *Physics in Medicine & Biology* 49 (17) (2004) 3903. doi:10.1088/0031-9155/49/17/006.
- [78] M. Defrise, F. Noo, R. Clackdoyle, H. Kudo, Truncated Hilbert transform and image reconstruction from limited tomographic data, *Inverse Problems* 22 (3) (2006) 1037. doi:10.1088/0266-5611/22/3/019.
- [79] H. Yu, G. Wang, Compressed sensing based interior tomography, *Physics in Medicine & Biology* 54 (9) (2009) 2791. doi:10.1088/0031-9155/54/9/014.
- [80] J. Yang, H. Yu, M. Jiang, G. Wang, High-order total variation minimization for interior tomography, *Inverse Problems* 26 (3) (2010) 035013. doi:10.1088/0266-5611/26/3/035013.
- [81] Q. Xu, X. Mou, G. Wang, J. Sieren, E. A. Hoffman, H. Yu, Statistical Interior Tomography, *IEEE transactions on medical imaging* 30 (5) (2011) 1116–1128. doi:10.1109/TMI.2011.2106161.
- [82] Y. Ye, H. Yu, Y. Wei, G. Wang, A General Local Reconstruction Approach Based on a Truncated Hilbert Transform, *International Journal of Biomedical Imaging* (2007) 63634doi:10.1155/2007/63634.
- [83] H. Kudo, M. Courdurier, F. Noo, M. Defrise, Tiny a priori knowledge solves the interior problem in computed tomography, *Physics in Medicine & Biology* 53 (9) (2008) 2207. doi:10.1088/0031-9155/53/9/001.
- [84] L. C. B. dos Santos, E. Guillard, H. Talbot, Combining interior tomography reconstruction and spatial regularization, in: *Image Processing (ICIP)*, IEEE, Paris, France, 2014, pp. 1768–1772. doi:10.1109/ICIP.2014.7025354.
- [85] T. Heußer, M. Brehm, S. Sawall, M. Kachelrieß, CT data completion based on prior scans, in: *2012 IEEE Nuclear Science Symposium and Medical Imaging Conference Record (NSS/MIC)*, 2012, pp. 2969–2976. doi:10.1109/NSSMIC.2012.6551679.
- [86] A. Kyrieleis, M. Ibson, V. Titarenko, P. J. Withers, Image stitching strategies for tomographic imaging of large objects at high resolution at synchrotron sources, *Nuclear Instruments and Methods in Physics Research Section A: Accelerators, Spectrometers, Detectors and Associated Equipment* 607 (3) (2009) 677–684. doi:10.1016/j.nima.2009.06.030.
- [87] D. Haberthür, C. Hintermüller, F. Marone, J. C. Schittny, M. Stamparoni, Radiation dose optimized lateral expansion of the field of view in synchrotron radiation X-ray tomographic microscopy, *Journal of Synchrotron Radiation* 17 (5) (2010) 590–599. doi:10.1107/S0909049510019618.
- [88] I. V. Oikonomidis, G. Lovric, T. P. Cremona, F. Arcadu, Alessandra Patera, J. C. Schittny, M. Stamparoni, Imaging samples larger than the field of view: the SLS experience, *Journal of Physics: Conference Series* 849 (1) (2017) 012004. doi:10.1088/1742-6596/849/1/012004.
- [89] J. Frank, *Electron Tomography*, second edition Edition, Springer, 2005.
- [90] M. E. Davison, The Ill-Conditioned Nature of the Limited Angle Tomography Problem, *SIAM Journal on Applied Mathematics* 43 (2) (1983) 428–448. doi:10.1137/0143028.
- [91] G. T. Herman, R. Davidi, Image reconstruction from a small number of projections, *Inverse Problems* 24 (4) (2008) 045011. doi:10.1088/0266-5611/24/4/045011.
- [92] J. Yang, Y. Zhang, W. Yin, A Fast Alternating Direction Method for TVL1-L2 Signal Reconstruction From Partial Fourier Data, *IEEE Journal of Selected Topics in Signal Processing* 4 (2) (2010) 288–297. doi:10.1109/JSTSP.2010.2042333.
- [93] W. Yu, C. Wang, X. Nie, M. Huang, L. Wu, Image Reconstruction for Few-view Computed Tomography Based on l0 Sparse Regularization, *Procedia Computer Science* 107 (2017) 808–813. doi:10.1016/j.procs.2017.03.178.
- [94] M. Rantala, S. Vanska, S. Jarvenpaa, M. Kalke, M. Lassas, J. Moberg, S. Siltanen, Wavelet-based reconstruction for limited-angle X-ray tomography, *IEEE Transactions on Medical Imaging* 25 (2) (2006) 210–217. doi:10.1109/TMI.2005.862206.
- [95] J. Friel, Sparse regularization in limited angle tomography, *Applied and Computational Harmonic Analysis* 34 (1) (2013) 117–141. doi:10.1016/j.acha.2012.03.005.
- [96] E. Maire, C. L. Bourlot, J. Adrien, A. Mortensen, R. Mokso, 20 Hz X-ray tomography during an in situ tensile test, *International Journal of Fracture* 200 (1-2) (2016) 3–12. doi:10.1007/s10704-016-0077-y.
- [97] R. Mokso, C. M. Schlepütz, G. Theidel, H. Billich, E. Schmid, T. Celcer, G. Mikuljan, L. Sala, F. Marone, N. Schlumpf, M. Stamparoni, GigaFRoST: the gigabit fast readout system for tomography, *Journal of Synchrotron Radiation* 24 (6) (2017) 1250–1259. doi:10.1107/S1600577517013522.
- [98] T. Bultreys, M. A. Boone, M. N. Boone, T. De Schryver, B. Masschaele, L. Van Hoorebeke, V. Cnudde, Fast laboratory-based micro-computed tomography for pore-scale research: Illustrative experiments and perspectives on the future, *Advances in Water Resources* 95 (2016) 341–351. doi:10.1016/j.advwatres.2015.05.012.
- [99] J. A. Seibert, J. M. Boone, K. K. Lindfors, Flat-field correction technique for digital detectors, in: *Medical Imaging 1998: Physics of Medical Imaging*, Vol. 3336, International Society for Optics and Photonics, 1998, pp. 348–355. doi:10.1117/12.317034.
- [100] V. V. Nieuwenhove, J. D. Beenhouwer, F. D. Carlo, L. Mancini, F. Marone, J. Sijbers, Dynamic intensity normalization using eigen flat fields in X-ray imaging, *Optics Express* 23 (21) (2015) 27975–27989. doi:10.1364/OE.23.027975.
- [101] C. Jailin, J.-Y. Buffière, F. Hild, M. Poncelet, S. Roux, On the use of flat-fields for tomographic reconstruction, *Journal of Synchrotron Radiation* 24 (1) (2017) 220–231. doi:10.1107/S1600577516015812.
- [102] S. Kappler, A. Henning, B. Kreisler, F. Schoeck, K. Stierstorfer, T. Flohr, Photon counting CT at elevated X-ray Tube currents: Contrast stability, image noise and multi-energy performance, Vol. 9033, 2014. doi:10.1117/12.2043511.
- [103] D. Walter, U. Zscherpel, U. Ewert, Photon Counting and Energy Discriminating X-Ray Detectors – Benefits and Applications, in: *Proceedings*

- ings of the 19th World Conference on Non-Destructive Testing 2016, Munich, Germany, 2016.
- [104] R. Cierniak, X-Ray Computed Tomography in Biomedical Engineering, Springer-Verlag London, 2011.
- [105] B. De Man, J. Nuyts, P. Dupont, G. Marchal, P. Suetens, Metal streak artifacts in X-ray computed tomography: a simulation study, *IEEE Transactions on Nuclear Science* 46 (3) (1999) 691–696. doi:10.1109/23.775600.
- [106] J. F. Barrett, N. Keat, Artifacts in CT: Recognition and Avoidance, *RadioGraphics* 24 (6) (2004) 1679–1691. doi:10.1148/rg.246045065.
- [107] G. R. Davis, J. C. Elliott, Artefacts in X-ray microtomography of materials, *Materials Science and Technology* 22 (9) (2006) 1011–1018. doi:10.1179/174328406X114117.
- [108] E. M. Abu Anas, J. G. Kim, S. Y. Lee, M. K. Hasan, Comparison of ring artifact removal methods using flat panel detector based CT images, *BioMedical Engineering OnLine* 10 (2011) 72. doi:10.1186/1475-925X-10-72.
- [109] F. E. Boas, D. Fleischmann, CT artifacts: causes and reduction techniques, *Imaging in Medicine* 4 (2) (2012) 229–240. doi:10.2217/iim.12.13.
- [110] G. R. Davis, J. C. Elliott, X-ray microtomography scanner using time-delay integration for elimination of ring artefacts in the reconstructed image, *Nuclear Instruments and Methods in Physics Research Section A: Accelerators, Spectrometers, Detectors and Associated Equipment* 394 (1) (1997) 157–162. doi:10.1016/S0168-9002(97)00566-4.
- [111] A. Mouton, N. Megherbi, K. Van Slambrouck, J. Nuyts, T. P. Breckon, An experimental survey of metal artefact reduction in computed tomography, *Journal of X-Ray Science and Technology* (2) (2013) 193–226. doi:10.3233/XST-130372.
- [112] W. A. Kalender, R. Hebel, J. Ebersberger, Reduction of CT artifacts caused by metallic implants, *Radiology* 164 (2) (1987) 576–577. doi:10.1148/radiology.164.2.3602406.
- [113] F. Morsbach, S. Bickelhaupt, G. A. Wanner, A. Krauss, B. Schmidt, H. Alkadhi, Reduction of Metal Artifacts from Hip Prostheses on CT Images of the Pelvis: Value of Iterative Reconstructions, *Radiology* 268 (1) (2013) 237–244. doi:10.1148/radiol.13122089.
- [114] Y. Zhang, H. Yan, X. Jia, J. Yang, S. B. Jiang, X. Mou, A hybrid metal artifact reduction algorithm for x-ray CT: A hybrid metal artifact reduction algorithm, *Medical Physics* 40 (4) (2013) 041910. doi:10.1118/1.4794474.
- [115] E. Pessis, R. Campagna, J.-M. Sverzut, F. Bach, M. Rodallec, H. Guerini, A. Feydy, J.-L. Drapé, Virtual Monochromatic Spectral Imaging with Fast Kilovoltage Switching: Reduction of Metal Artifacts at CT, *RadioGraphics* 33 (2) (2013) 573–583. doi:10.1148/rg.332125124.
- [116] S. Kuchenbecker, S. Faby, S. Sawall, M. Lell, M. Kachelrieß, Dual energy CT: How well can pseudo-monochromatic imaging reduce metal artifacts?: DECT: Can monoenergetic imaging remove metal artifacts?, *Medical Physics* 42 (2) (2015) 1023–1036. doi:10.1118/1.4905106.
- [117] S. Scheiner, R. Sinibaldi, B. Pichler, V. Komlev, C. Renghini, C. Vitale-Brovarone, F. Rustichelli, C. Hellmich, Micromechanics of bone tissue-engineering scaffolds, based on resolution error-cleared computer tomography, *Biomaterials* 30 (12) (2009) 2411–2419. doi:10.1016/j.biomaterials.2008.12.048.
- [118] J.-F. Bruchon, J.-M. Pereira, M. Vandamme, N. Lenoir, P. Delage, M. Bornert, Full 3d investigation and characterisation of capillary collapse of a loose unsaturated sand using X-ray CT, *Granular Matter* 15 (6) (2013) 783–800. doi:10.1007/s10035-013-0452-6.
- [119] E. Boulard, A. King, N. Guignot, J.-P. Deslandes, Y. Le Godec, J.-P. Perrillat, A. Clark, G. Morard, J.-P. Itié, High-speed tomography under extreme conditions at the PSICHE beamline of the SOLEIL Synchrotron, *Journal of Synchrotron Radiation* 25 (3) (2018) 818–825. doi:10.1107/S1600577518004861.
- [120] M. Kovács, R. Danyi, M. Erdélyi, P. Fejérdy, C. Dobó-Nagy, Distortional effect of beam-hardening artefacts on microCT: a simulation study based on an in vitro caries model, *Oral Surgery, Oral Medicine, Oral Pathology, Oral Radiology, and Endodontology* 108 (4) (2009) 591–599. doi:10.1016/j.tripleo.2009.06.009.
- [121] R. A. Ketcham, R. D. Hanna, Beam hardening correction for X-ray computed tomography of heterogeneous natural materials, *Computers & Geosciences* 67 (2014) 49–61. doi:10.1016/j.cageo.2014.03.003.
- [122] M. Krumm, S. Kasperl, M. Franz, Reducing non-linear artifacts of multi-material objects in industrial 3d computed tomography, *NDT & E International* 41 (4) (2008) 242–251. doi:10.1016/j.ndteint.2007.12.001.
- [123] G. V. Gompel, K. V. Slambrouck, M. Defrise, K. J. Batenburg, J. d. Mey, J. Sijbers, J. Nuyts, Iterative correction of beam hardening artifacts in CT, *Medical Physics* 38 (S1) (2011) S36–S49. doi:10.1118/1.3577758.
- [124] G. Rigaud, On Analytical Solutions to Beam-Hardening, *Sensing and Imaging* 18 (1) (Dec. 2017). doi:10.1007/s11220-016-0153-4.
- [125] R. Hegerl, W. Hoppe, Influence of Electron Noise on Three-dimensional Image Reconstruction, *Zeitschrift für Naturforschung A* 31 (12) (1976) 1717–1721. doi:10.1515/zna-1976-1241.
- [126] W. Hoppe, R. Hegerl, Some remarks concerning the influence of electron noise on 3D reconstruction, *Ultramicroscopy* 6 (1) (1981) 205–206. doi:10.1016/S0304-3991(81)80200-8.
- [127] B. F. McEwen, K. H. Downing, R. M. Glaeser, The relevance of dose-fractionation in tomography of radiation-sensitive specimens, *Ultramicroscopy* 60 (3) (1995) 357–373. doi:10.1016/0304-3991(95)00082-8.
- [128] L. Garnero, J. Brunol, S. Lowenthal, Problèmes Statistiques en Tomographie Axiale Transverse, *Optica Acta: International Journal of Optics* 28 (8) (1981) 1071–1085. doi:10.1080/713820707.
- [129] F. Peyrin, L. Garnero, I. Magnin, Introduction to 2d and 3d tomographic methods based on straight line propagation: X-ray, emission and ultrasonic tomography, *Traitement du Signal* 13 (4) (1996) 382–413.
- [130] T. Lei, W. Sewchand, Statistical Approach to X-ray CT and Its Applications in Image Analysis, in: *Medical Imaging III: Image Formation*, Vol. 1090, International Society for Optics and Photonics, 1989, pp. 456–471. doi:10.1117/12.953233.
- [131] T. Lei, W. Sewchand, Statistical approach to X-ray CT imaging and its applications in image analysis. I. Statistical analysis of X-ray CT imaging, *IEEE Transactions on Medical Imaging* 11 (1) (1992) 53–61. doi:10.1109/42.126910.
- [132] T. Lei, J. K. Udupa, Statistical properties of x-ray CT and MRI: from imaging physics to image statistics, in: *Medical Imaging 2002: Physics of Medical Imaging*, Vol. 4682, International Society for Optics and Photonics, 2002, pp. 82–94. doi:10.1117/12.465626.
- [133] R. C. Gonzalez, R. E. Woods, *Digital image processing*, 4th Edition, Pearson, New York, NY, 2018.
- [134] W. Burger, M. J. Burge, *Digital Image Processing: An Algorithmic Introduction Using Java*, 2nd Edition, Texts in Computer Science, Springer-Verlag, London, 2016, http://dx.doi.org/10.1007/978-1-4471-6684-9.
- [135] R. Szeliski, *Computer Vision: Algorithms and Applications*, Texts in Computer Science, Springer-Verlag, London, 2011.
- [136] M. Petrou, P. Bosdogianni, *Image processing: the fundamentals*, Wiley, Chichester [England] ; New York, 1999.
- [137] B. K. Bay, T. S. Smith, D. P. Fyhrig, M. Saad, Digital volume correlation: Three-dimensional strain mapping using X-ray tomography, *Experimental Mechanics* 39 (3) (1999) 217–226. doi:10.1007/BF02323555.
- [138] N. Lenoir, M. Bornert, J. Desrues, P. Bésuelle, G. Viggiani, Volumetric Digital Image Correlation Applied to X-ray Microtomography Images from Triaxial Compression Tests on Argillaceous Rock, *Strain* 43 (3) (2007) 193–205. doi:10.1111/j.1475-1305.2007.00348.x.
- [139] A. Germaneau, P. Doumalin, J.-C. Dupré, Comparison between X-ray micro-computed tomography and optical scanning tomography for full 3d strain measurement by digital volume correlation, *NDT & E International* 41 (6) (2008) 407–415. doi:10.1016/j.ndteint.2008.04.001.
- [140] S. Roux, F. Hild, P. Viot, D. Bernard, Three-dimensional image correlation from X-ray computed tomography of solid foam, *Composites Part A: Applied Science and Manufacturing* 39 (8) (2008) 1253–1265. doi:10.1016/j.compositesa.2007.11.011.
- [141] S. A. Hall, M. Bornert, J. Desrues, Y. Pannier, N. Lenoir, G. Viggiani, P. Bésuelle, Discrete and continuum analysis of localised deformation in sand using X-ray μ CT and volumetric digital image correlation, *Géotechnique* 60 (5) (2010) 315–322.
- [142] E. Andò, S. A. Hall, G. Viggiani, J. Desrues, P. Bésuelle, Grain-scale experimental investigation of localised deformation in sand: a discrete

- particle tracking approach, *Acta Geotechnica* 7 (1) (2012) 1–13. doi:10.1007/s11440-011-0151-6.
- [143] O. Lézoray, L. Grady (Eds.), *Image Processing and Analysis With Graphs: Theory and Practice*, Digital Imaging and Computer Vision Series, CRC Press, Taylor & Francis Group, Boca Raton, FL, 2012.
- [144] C. Couprie, L. Grady, L. Najman, H. Talbot, Power Watershed: A Unifying Graph-Based Optimization Framework, *IEEE Transactions on Pattern Analysis and Machine Intelligence* 33 (7) (2011) 1384–1399. doi:10.1109/TPAMI.2010.200.
- [145] D. M. Ushizima, H. A. Bale, E. W. Bethel, P. Ercius, B. A. Helms, H. Krishnan, L. T. Grinberg, M. Haranczyk, A. A. Macdowell, K. Odziomek, D. Y. Parkinson, T. Perciano, R. O. Ritchie, C. Yang, IDEAL: Images Across Domains, Experiments, Algorithms and Learning, *JOM* 68 (11) (2016) 2963–2972. doi:10.1007/s11837-016-2098-4.
- [146] D. Y. Parkinson, D. M. Pelt, T. Perciano, D. Ushizima, H. Krishnan, H. S. Barnard, A. A. MacDowell, J. Sethian, Machine learning for micro-tomography, in: *Proceedings of the SPIE*, Vol. 10391, International Society for Optics and Photonics, San Diego, CA, United States, 2017, p. 103910J. doi:10.1117/12.2274731.
- [147] S. van der Walt, J. L. Schönberger, J. Nunez-Iglesias, F. Boulogne, J. D. Warner, N. Yager, E. Goullart, T. Yu, scikit-image: image processing in Python, *PeerJ* 2 (2014) e453. doi:10.7717/peerj.453.
- [148] U. Ayachit, *The ParaView Guide: A Parallel Visualization Application*, full color version Edition, Kitware, Los Alamos, 2015, oCLC: 944221263.
- [149] H. Childs, E. Brugger, B. Whitlock, J. Meredith, S. Ahern, D. Pugmire, K. Biagas, M. Miller, C. Harrison, G. H. Weber, H. Krishnan, T. Fogal, A. Sanderson, C. Garth, E. W. Bethel, D. Camp, O. Rübel, M. Durant, J. M. Favre, P. Navrátil, VisIt: An End-User Tool For Visualizing and Analyzing Very Large Data, in: E. W. Bethel, H. Childs, C. Hansen (Eds.), *High Performance Visualization—Enabling Extreme-Scale Scientific Insight*, CRC Press, Taylor & Francis Group, Boca Raton, FL, 2016, pp. 357–372.
- [150] K. S. Nowinski, B. Borucki, VisNow – a Modular, Extensible Visual Analysis Platform, in: *Proceedings of the 22nd Conference on Computer Graphics, Visualization and Computer Vision*, 2014, pp. 73–76.
- [151] R. Kikinis, S. D. Pieper, K. G. Vosburgh, 3d Slicer: A Platform for Subject-Specific Image Analysis, Visualization, and Clinical Support, in: *Intraoperative Imaging and Image-Guided Therapy*, Springer, New York, NY, 2014, pp. 277–289. doi:10.1007/978-1-4614-7657-3_19.
- [152] A. Buades, B. Coll, J. Morel, A Review of Image Denoising Algorithms, with a New One, *Multiscale Modeling & Simulation* 4 (2) (2005) 490–530. doi:10.1137/040616024.
- [153] J. J. Koenderink, The structure of images, *Biological Cybernetics* 50 (5) (1984) 363–370. doi:10.1007/BF00336961.
- [154] T. Lindeberg, Scale-space theory: a basic tool for analyzing structures at different scales, *Journal of Applied Statistics* 21 (1-2) (1994) 225–270. doi:10.1080/757582976.
- [155] T. Lindeberg, Scale-Space, in: *Wiley Encyclopedia of Computer Science and Engineering*, John Wiley & Sons, Inc., 2007.
- [156] T. Lindeberg, Generalized Gaussian Scale-Space Axiomatics Comprising Linear Scale-Space, Affine Scale-Space and Spatio-Temporal Scale-Space, *Journal of Mathematical Imaging and Vision* 40 (1) (2011) 36–81. doi:10.1007/s10851-010-0242-2.
- [157] T. Huang, G. Yang, G. Tang, A fast two-dimensional median filtering algorithm, *IEEE Transactions on Acoustics, Speech, and Signal Processing* 27 (1) (1979) 13–18. doi:10.1109/TASSP.1979.1163188.
- [158] C. Tomasi, R. Manduchi, Bilateral filtering for gray and color images, in: *Sixth International Conference on Computer Vision*, IEEE, Bombay, India, 1998, pp. 839–846. doi:10.1109/ICCV.1998.710815.
- [159] P. Perona, J. Malik, Scale-space and edge detection using anisotropic diffusion, *IEEE Transactions on Pattern Analysis and Machine Intelligence* 12 (7) (1990) 629–639. doi:10.1109/34.56205.
- [160] L. I. Rudin, S. Osher, E. Fatemi, Nonlinear total variation based noise removal algorithms, *Physica D: Nonlinear Phenomena* 60 (1–4) (1992) 259–268. doi:10.1016/0167-2789(92)90242-F.
- [161] A. Chambolle, An Algorithm for Total Variation Minimization and Applications, *Journal of Mathematical Imaging and Vision* 20 (1-2) (2004) 89–97. doi:10.1023/B:JMIV.0000011325.36760.1e.
- [162] A. Danielyan, V. Katkovnik, K. Egiazarian, BM3d Frames and Variational Image Deblurring, *IEEE Transactions on Image Processing* 21 (4) (2012) 1715–1728. doi:10.1109/TIP.2011.2176954.
- [163] D. Pacella, Energy-resolved X-ray detectors: The future of diagnostic imaging, *Reports in Medical Imaging* (2015) 1doi:10.2147/RMI.S50045.
- [164] K. Taguchi, Energy-sensitive photon counting detector-based X-ray computed tomography, *Radiological Physics and Technology* 10 (1) (2017) 8–22. doi:10.1007/s12194-017-0390-9.
- [165] M. J. Willemink, M. Persson, A. Pourmorteza, N. J. Pelc, D. Fleischmann, Photon-counting CT: Technical Principles and Clinical Prospects, *Radiology* 289 (2) (2018) 293–312. doi:10.1148/radiol.2018172656.
- [166] P. K. Sahoo, S. Soltani, A. K. C. Wong, Y. C. Chen, A survey of thresholding techniques, *Computer Vision, Graphics, and Image Processing* 41 (2) (1988) 233–260. doi:10.1016/0734-189X(88)90022-9.
- [167] M. Sezgin, B. Sankur, Survey over image thresholding techniques and quantitative performance evaluation, *Journal of Electronic Imaging* 13 (1) (2004) 146–166. doi:10.1117/1.1631315.
- [168] N. Otsu, A Threshold Selection Method from Gray-Level Histograms, *IEEE Transactions on Systems, Man and Cybernetics* 9 (1) (1979) 62–66. doi:10.1109/TSMC.1979.4310076.
- [169] J. N. Kapur, P. K. Sahoo, A. K. C. Wong, A new method for gray-level picture thresholding using the entropy of the histogram, *Computer Vision, Graphics, and Image Processing* 29 (3) (1985) 273–285. doi:10.1016/0734-189X(85)90125-2.
- [170] C. H. Li, C. K. Lee, Minimum cross entropy thresholding, *Pattern Recognition* 26 (4) (1993) 617–625. doi:10.1016/0031-3203(93)90115-D.
- [171] L.-K. Huang, M.-J. J. Wang, Image thresholding by minimizing the measures of fuzziness, *Pattern Recognition* 28 (1) (1995) 41–51. doi:10.1016/0031-3203(94)E0043-K.
- [172] C. H. Li, P. K. S. Tam, An iterative algorithm for minimum cross entropy thresholding, *Pattern Recognition Letters* 19 (8) (1998) 771–776. doi:10.1016/S0167-8655(98)00057-9.
- [173] Z.-K. Huang, K.-W. Chau, A new image thresholding method based on Gaussian mixture model, *Applied Mathematics and Computation* 205 (2) (2008) 899–907. doi:10.1016/j.amc.2008.05.130.
- [174] J. Sauvola, M. Pietikäinen, Adaptive document image binarization, *Pattern Recognition* 33 (2) (2000) 225–236. doi:10.1016/S0031-3203(99)00055-2.
- [175] O. Stamatii, E. Roubin, E. Andò, Y. Malecot, Phase segmentation of concrete x-ray tomographic images at meso-scale: Validation with neutron tomography, *Cement and Concrete Composites* 88 (2018) 8–16. doi:10.1016/j.cemconcomp.2017.12.011.
- [176] L. Grady, Random Walks for Image Segmentation, *IEEE Transactions on Pattern Analysis and Machine Intelligence* 28 (11) (2006) 1768–1783. doi:10.1109/TPAMI.2006.233.
- [177] P. Soille, *Morphological Image Analysis: Principles and Applications*, Springer Berlin Heidelberg, Berlin, Heidelberg, 2004. doi:10.1007/978-3-662-05088-0.
- [178] L. Najman, H. Talbot (Eds.), *Mathematical Morphology: From Theory to Applications*, John Wiley & Sons, Inc., Hoboken, NJ, USA, 2013. doi:10.1002/9781118600788.
- [179] F. Y. Shih, *Image Processing and Mathematical Morphology: fundamentals and applications.*, CRC PRESS, S.I., 2017, oCLC: 1007930037.
- [180] J. Serra, Introduction to mathematical morphology, *Computer Vision, Graphics, and Image Processing* 35 (3) (1986) 283–305. doi:10.1016/0734-189X(86)90002-2.
- [181] E. J. Breen, R. Jones, H. Talbot, Mathematical morphology: A useful set of tools for image analysis, *Statistics and Computing* 10 (2) (2000) 105–120. doi:10.1023/A:1008990208911.
- [182] L. He, X. Ren, Q. Gao, X. Zhao, B. Yao, Y. Chao, The connected-component labeling problem: A review of state-of-the-art algorithms, *Pattern Recognition* 70 (2017) 25–43. doi:10.1016/j.patcog.2017.04.018.
- [183] S. Beucher, C. Lantuéjoul, Use of Watersheds in Contour Detection, Rennes, France, 1979.
- [184] F. Meyer, An overview of morphological segmentation, *International Journal of Pattern Recognition and Artificial Intelligence* 15 (07) (2001) 1089–1118. doi:10.1142/S0218001401001337.
- [185] D. Stutz, A. Hermans, B. Leibe, Superpixels: An evaluation of the state-

- of-the-art, *Computer Vision and Image Understanding* 166 (2018) 1–27. doi:10.1016/j.cviu.2017.03.007.
- [186] S. Beucher, The watershed transformation applied to image segmentation, in: *Scanning Microscopy International*, Vol. suppl. 6, Cambridge, UK, 1992, pp. 299–314.
- [187] L. Vincent, P. Soille, Watersheds in digital spaces: an efficient algorithm based on immersion simulations, *IEEE Transactions on Pattern Analysis and Machine Intelligence* 13 (6) (1991) 583–598. doi:10.1109/34.87344.
- [188] J. B. T. M. Roerdink, A. Meijster, The Watershed Transform: Definitions, Algorithms and Parallelization Strategies, *Fundamenta Informaticae* 41 (1,2) (2000) 187–228. doi:10.3233/FI-2000-411207.
- [189] F. Meyer, S. Beucher, Morphological segmentation, *Journal of Visual Communication and Image Representation* 1 (1) (1990) 21–46. doi:10.1016/1047-3203(90)90014-M.
- [190] V. Tariel, D. Jeulin, A. Fanget, G. Contesse, 3d multi-scale segmentation of granular materials, *Image Analysis & Stereology* 27 (1) (2011) 23–28. doi:10.5566/ias.v27.p23-28.
- [191] W. E. Lorensen, H. E. Cline, Marching Cubes: A High Resolution 3d Surface Construction Algorithm, in: *Proceedings of the 14th Annual Conference on Computer Graphics and Interactive Techniques*, ACM, 1987, pp. 163–169. doi:10.1145/37401.37422.
- [192] H. G. Merkus, *Particle Size Measurements: Fundamentals, Practice, Quality*, Particle Technology Series, Springer Netherlands, 2009.
- [193] J. Escoda, F. Willot, D. Jeulin, J. Sanahuja, C. Toulemonde, Estimation of local stresses and elastic properties of a mortar sample by FFT computation of fields on a 3d image, *Cement and Concrete Research* 41 (5) (2011) 542–556. doi:10.1016/j.cemconres.2011.02.003.
- [194] S. Seltzer, *Tables of X-Ray Mass Attenuation Coefficients and Mass Energy-Absorption Coefficients*, NIST Standard Reference Database 126 NISTIR 5632, National Institute of Standards and Technology, Gaithersburg, MD (1995). doi:10.18434/t4d01f.
- [195] M. Lanzón, V. Cnudde, T. de Kock, J. Dewanckele, X-ray microtomography (μ -CT) to evaluate microstructure of mortars containing low density additions, *Cement and Concrete Composites* 34 (9) (2012) 993–1000. doi:10.1016/j.cemconcomp.2012.06.011.
- [196] A. Qsymah, R. Sharma, Z. Yang, L. Margetts, P. Mummery, Micro X-ray computed tomography image-based two-scale homogenisation of ultra high performance fibre reinforced concrete, *Construction and Building Materials* 130 (2017) 230–240. doi:10.1016/j.conbuildmat.2016.09.020.
- [197] L. Yang, Y. Zhang, Z. Liu, P. Zhao, C. Liu, In-situ tracking of water transport in cement paste using X-ray computed tomography combined with CsCl enhancing, *Materials Letters* 160 (2015) 381–383. doi:10.1016/j.matlet.2015.08.011.
- [198] M. Khanzadeh Moradillo, Q. Hu, M. T. Ley, Using X-ray imaging to investigate in-situ ion diffusion in cementitious materials, *Construction and Building Materials* 136 (2017) 88–98. doi:10.1016/j.conbuildmat.2017.01.038.
- [199] P. Tritt, B. Münch, W. Weiss, A. Kaestner, I. Jerjen, L. Josic, E. Lehmann, P. Lura, Release of internal curing water from lightweight aggregates in cement paste investigated by neutron and X-ray tomography, *Nuclear Instruments and Methods in Physics Research Section A: Accelerators, Spectrometers, Detectors and Associated Equipment* 651 (1) (2011) 244–249. doi:10.1016/j.nima.2011.02.012.
- [200] F. Yang, M. Griffa, A. Hipp, H. Derluyn, P. Moonen, R. Kaufmann, M. N. Boone, F. Beckmann, P. Lura, Advancing the visualization of pure water transport in porous materials by fast, talbot interferometry-based multi-contrast x-ray micro-tomography, 2016, p. 99670L. doi:10.1117/12.2236221.
- [201] P. Carrara, R. Kruse, D. P. Bentz, M. Lunardelli, T. Leusmann, P. A. Varady, L. De Lorenzis, Improved mesoscale segmentation of concrete from 3d X-ray images using contrast enhancers, *Cement and Concrete Composites* 93 (2018) 30–42. doi:10.1016/j.cemconcomp.2018.06.014.
- [202] M. Parisatto, M. C. Dalconi, L. Valentini, G. Artioli, A. Rack, R. Tucoulou, G. Cruciani, G. Ferrari, Examining microstructural evolution of Portland cements by in-situ synchrotron micro-tomography, *Journal of Materials Science* 50 (4) (2015) 1805–1817. doi:10.1007/s10853-014-8743-9.
- [203] M. Voltolini, M. C. Dalconi, G. Artioli, M. Parisatto, L. Valentini, V. Russo, A. Bonnin, R. Tucoulou, Understanding cement hydration at the microscale: new opportunities from ‘pencil-beam’ synchrotron X-ray diffraction tomography, *Journal of Applied Crystallography* 46 (1) (2013) 142–152. doi:10.1107/S0021889812046985.
- [204] T. Sugiyama, T. Hitomi, K. Kajiwara, Nondestructive Integrated CT-XRD Method for Research on Hydrated Cement System, in: *Proceedings of the 4th International Conference on the Durability of Concrete Structures*, Purdue University, West Lafayette, IN, USA, 2014, pp. 298–303.
- [205] L. Valentini, M. C. Dalconi, M. Parisatto, G. Cruciani, G. Artioli, Towards three-dimensional quantitative reconstruction of cement microstructure by X-ray diffraction microtomography, *Journal of Applied Crystallography* 44 (2) (2011) 272–280. doi:10.1107/S0021889810054701.
- [206] Q. Hu, M. T. Ley, J. Davis, J. C. Hanan, R. Frazier, Y. Zhang, 3d chemical segmentation of fly ash particles with X-ray computed tomography and electron probe microanalysis, *Fuel* 116 (2014) 229–236. doi:10.1016/j.fuel.2013.07.037.
- [207] H. Takahashi, T. Sugiyama, Investigation of alteration in deteriorated mortar due to water attack using non-destructive integrated CT-XRD method, in: K. Maekawa, A. Kasuga, J. Yamazaki (Eds.), *Proceedings of the 11th International PhD Symposium in Civil Engineering*, Tokyo, Japan, 2016, pp. 445–452.
- [208] M. Leite, P. Monteiro, Microstructural analysis of recycled concrete using X-ray microtomography, *Cement and Concrete Research* 81 (2016) 38–48. doi:10.1016/j.cemconres.2015.11.010.
- [209] K. Wan, Q. Xu, Local porosity distribution of cement paste characterized by X-ray micro-tomography, *Science China Technological Sciences* 57 (5) (2014) 953–961. doi:10.1007/s11431-014-5513-5.
- [210] B. Łaźniewska-Piekarczyk, J. Szwabowski, P. Miera, Porosity parameters of concrete with innovative air-entraining multicomponent portland cement CEM II/B-V, in: *Proceedings of the 11th International Symposium on Brittle Matrix Composites*, Warsaw, 2015, pp. 151–160.
- [211] T. Pyatina, T. Sugama, J. Moon, S. James, Effect of Tartaric Acid on Hydration of a Sodium-Metasilicate-Activated Blend of Calcium Aluminate Cement and Fly Ash F, *Materials* 9 (12) (2016) 422. doi:10.3390/ma9060422.
- [212] B. Lee, J.-S. Lee, J. Min, J. H. Lee, Evaluation of physical characteristics and microscopic structure of mortar containing synthetic resin, *Construction and Building Materials* 114 (2016) 880–887. doi:10.1016/j.conbuildmat.2016.03.192.
- [213] B. J. Olawuyi, W. P. Boshoff, Influence of SAP content and curing age on air void distribution of high performance concrete using 3d volume analysis, *Construction and Building Materials* 135 (2017) 580–589. doi:10.1016/j.conbuildmat.2016.12.128.
- [214] I. Viejo, L. P. Esteves, M. Laspalas, J. M. Bielsa, Numerical modelling of porous cement-based materials by superabsorbent polymers, *Cement and Concrete Research* 90 (2016) 184–193. doi:10.1016/j.cemconres.2016.07.018.
- [215] M. Lanzón, V. Cnudde, T. De Kock, J. Dewanckele, Microstructural examination and potential application of rendering mortars made of tire rubber and expanded polystyrene wastes, *Construction and Building Materials* 94 (2015) 817–825. doi:10.1016/j.conbuildmat.2015.07.086.
- [216] M. Murugan, M. Santhanam, S. Sen Gupta, T. Pradeep, S. P. Shah, Influence of 2d rGO nanosheets on the properties of OPC paste, *Cement and Concrete Composites* 70 (2016) 48–59. doi:10.1016/j.cemconcomp.2016.03.005.
- [217] A. Kashani, T. D. Ngo, P. Mendis, J. R. Black, A. Hajimohammadi, A sustainable application of recycled tyre crumbs as insulator in lightweight cellular concrete, *Journal of Cleaner Production* 149 (2017) 925–935. doi:10.1016/j.jclepro.2017.02.154.
- [218] S. Pilehvar, V. D. Cao, A. M. Szczotok, L. Valentini, D. Salvioni, M. Magistri, R. Pamies, A.-L. Kjønksen, Mechanical properties and microscale changes of geopolymer concrete and Portland cement concrete containing micro-encapsulated phase change materials, *Cement and Concrete Research* 100 (2017) 341–349. doi:10.1016/j.cemconres.2017.07.012.
- [219] P. Niewiadomski, D. Stefaniuk, J. Hoła, Microstructural Analysis of Self-compacting Concrete Modified with the Addition of Nanoparticles, *Procedia Engineering* 172 (2017) 776–783. doi:10.1016/j.proeng.

- 2017.02.122.
- [220] P. Awoyera, A. Dawson, N. Thom, J. Akinmusuru, Suitability of mortars produced using laterite and ceramic wastes: Mechanical and microscale analysis, *Construction and Building Materials* 148 (2017) 195–203. doi:10.1016/j.conbuildmat.2017.05.031.
- [221] C. E. Schaefer, K. Kupwade-Patil, M. Ortega, C. Soriano, O. Büyükköztürk, A. E. White, M. P. Short, Irradiated recycled plastic as a concrete additive for improved chemo-mechanical properties and lower carbon footprint, *Waste Management* 71 (2018) 426–439. doi:10.1016/j.wasman.2017.09.033.
- [222] U. Rattanasak, K. Kendall, Pore structure of cement/pozzolan composites by X-ray microtomography, *Cement and Concrete Research* 35 (4) (2005) 637–640. doi:10.1016/j.cemconres.2004.04.022.
- [223] I. Tekin, R. Birgul, H. Y. Aruntas, Determination of the effect of volcanic pumice replacement on macro void development for blended cement mortars by computerized tomography, *Construction and Building Materials* 35 (2012) 15–22. doi:10.1016/j.conbuildmat.2012.02.084.
- [224] I. Tekin, R. Birgul, I. Ozgur Yaman, O. Gencel, H. Yilmaz Aruntas, Monitoring macro voids in mortars by computerized tomography method, *Measurement* 63 (2015) 299–308. doi:10.1016/j.measurement.2014.11.034.
- [225] E. G. A. Ferreira, F. Yokaichiya, M. S. Rodrigues, A. L. Beraldo, A. Isaac, N. Kardjilov, M. K. Franco, Assessment of Greener Cement by employing thermally treated sugarcane straw ashes, *Construction and Building Materials* 141 (2017) 343–352. doi:10.1016/j.conbuildmat.2017.03.022.
- [226] K. Kupwade-Patil, S. D. Palkovic, A. Bumajdad, C. Soriano, O. Büyükköztürk, Use of silica fume and natural volcanic ash as a replacement to Portland cement: Micro and pore structural investigation using NMR, XRD, FTIR and X-ray microtomography, *Construction and Building Materials* 158 (2018) 574–590. doi:10.1016/j.conbuildmat.2017.09.165.
- [227] W.-J. Long, B.-X. Xiao, Y.-C. Gu, F. Xing, Micro- and macro-scale characterization of nano-SiO₂ reinforced alkali activated slag composites, *Materials Characterization* 136 (2018) 111–121. doi:10.1016/j.matchar.2017.12.013.
- [228] G. Ferrari, L. Valentini, V. Russo, M. C. Dalconi, M. Favero, G. Artioli, Improving the performance of PCE superplasticizers in early stiffening Portland cement, *Construction and Building Materials* 130 (2017) 83–91. doi:10.1016/j.conbuildmat.2016.11.015.
- [229] F. Chalencon, P. Dumont, L. Orgéas, G. Foray, J.-Y. Cavallé, E. Maire, Homogeneous and heterogeneous rheology and flow-induced microstructures of a fresh fiber-reinforced mortar, *Cement and Concrete Research* 82 (2016) 130–141. doi:10.1016/j.cemconres.2015.12.012.
- [230] S.-Y. Chung, M. A. Elrahman, D. Stephan, P. H. Kamm, Investigation of characteristics and responses of insulating cement paste specimens with Aer solids using X-ray micro-computed tomography, *Construction and Building Materials* 118 (2016) 204–215. doi:10.1016/j.conbuildmat.2016.04.159.
- [231] M. Maaroufi, K. Abahri, C. E. Hachem, R. Belarbi, Characterization of EPS lightweight concrete microstructure by X-ray tomography with consideration of thermal variations, *Construction and Building Materials* 178 (2018) 339–348. doi:10.1016/j.conbuildmat.2018.05.142.
- [232] J. Pinilla Melo, A. Sepulcre Aguilar, F. Hernández Olivares, Rheological properties of aerated cement pastes with fly ash, metakaolin and sepiolite additions, *Construction and Building Materials* 65 (2014) 566–573. doi:10.1016/j.conbuildmat.2014.05.034.
- [233] S.-Y. Chung, T.-S. Han, S.-Y. Kim, T.-H. Lee, Investigation of the permeability of porous concrete reconstructed using probabilistic description methods, *Construction and Building Materials* 66 (2014) 760–770. doi:10.1016/j.conbuildmat.2014.06.013.
- [234] H. Rifai, A. Staude, D. Meinel, B. Illerhaus, G. Bruno, In-situ pore size investigations of loaded porous concrete with non-destructive methods, *Cement and Concrete Research* 111 (2018) 72–80. doi:10.1016/j.cemconres.2018.06.008.
- [235] V. Calderón, S. Gutiérrez-González, A. Rodríguez, M. Horgnies, Study of the microstructure and pores distribution of lightweight mortar containing polymer waste aggregates, *WIT Transactions on Engineering Sciences* 77 (2013) 263–272. doi:10.2495/MC130231.
- [236] S. Wei, C. Yiqiang, Z. Yunsheng, M. Jones, Characterization and simulation of microstructure and thermal properties of foamed concrete, *Construction and Building Materials* 47 (2013) 1278–1291. doi:10.1016/j.conbuildmat.2013.06.027.
- [237] W. She, Y. Du, C. Miao, J. Liu, G. Zhao, J. Jiang, Y. Zhang, Application of organic- and nanoparticle-modified foams in foamed concrete: Reinforcement and stabilization mechanisms, *Cement and Concrete Research* 106 (2018) 12–22. doi:10.1016/j.cemconres.2018.01.020.
- [238] V. Ducman, L. Korat, Characterization of geopolymer fly-ash based foams obtained with the addition of Al powder or H₂O₂ as foaming agents, *Materials Characterization* 113 (2016) 207–213. doi:10.1016/j.matchar.2016.01.019.
- [239] L. Korat, V. Ducman, The influence of the stabilizing agent SDS on porosity development in alkali-activated fly-ash based foams, *Cement and Concrete Composites* 80 (2017) 168–174. doi:10.1016/j.cemconcomp.2017.03.010.
- [240] S.-Y. Chung, T.-S. Han, S.-Y. Kim, Reconstruction and evaluation of the air permeability of a cement paste specimen with a void distribution gradient using CT images and numerical methods, *Construction and Building Materials* 87 (2015) 45–53. doi:10.1016/j.conbuildmat.2015.03.103.
- [241] M. Koster, J. Hannawald, W. Brameshuber, Simulation of water permeability and water vapor diffusion through hardened cement paste, *Computational Mechanics* 37 (2) (2006) 163–172. doi:10.1007/s00466-005-0687-0.
- [242] M. R. Karim, K. Krabbenhoft, Extraction of Effective Cement Paste Diffusivities from X-ray Microtomography Scans, *Transport in Porous Media* 84 (2) (2010) 371–388. doi:10.1007/s11242-009-9506-y.
- [243] J. Schock, S. Liebl, K. Achterhold, F. Pfeiffer, Obtaining the spacing factor of microporous concrete using high-resolution Dual Energy X-ray Micro CT, *Cement and Concrete Research* 89 (2016) 200–205. doi:10.1016/j.cemconres.2016.08.008.
- [244] N. Bossa, P. Chaurand, J. Vicente, D. Borschneck, C. Levard, O. Aguerre-Chariol, J. Rose, Micro- and nano-X-ray computed tomography: A step forward in the characterization of the pore network of a leached cement paste, *Cement and Concrete Research* 67 (2015) 138–147. doi:10.1016/j.cemconres.2014.08.007.
- [245] M. A. B. Promentilla, T. Sugiyama, T. Hitomi, N. Takeda, Characterizing the 3d Pore Structure of Hardened Cement Paste with Synchrotron Microtomography, *Journal of Advanced Concrete Technology* 6 (2) (2008) 273–286. doi:10.3151/jact.6.273.
- [246] M. Promentilla, T. Sugiyama, T. Hitomi, N. Takeda, Quantification of tortuosity in hardened cement pastes using synchrotron-based X-ray computed microtomography, *Cement and Concrete Research* 39 (6) (2009) 548–557. doi:10.1016/j.cemconres.2009.03.005.
- [247] J. L. Provis, R. J. Myers, C. E. White, V. Rose, J. S. van Deventer, X-ray microtomography shows pore structure and tortuosity in alkali-activated binders, *Cement and Concrete Research* 42 (6) (2012) 855–864. doi:10.1016/j.cemconres.2012.03.004.
- [248] Z. Ranachowski, D. Józwiak-Niedzwiedzka, P. Ranachowski, F. Rejmund, M. Dabrowski, S. Kudela, T. Dvorak, Application of X-Ray Microtomography and Optical Microscopy to Determine the Microstructure of Concrete Penetrated by Carbon Dioxide/ Zastosowanie Mikrotomografii Komputerowej I Mikroskopii Optycznej Do Oceny Mikrostruktury Betonów Poddanych Działaniu Co₂, *Archives of Metallurgy and Materials* 59 (4) (Jan. 2014). doi:10.2478/amm-2014-0245.
- [249] K. Schabowicz, Z. Ranachowski, D. Józwiak-Niedzwiedzka, Ł. Radzik, S. Kudela, T. Dvorak, Application of X-ray microtomography to quality assessment of fibre cement boards, *Construction and Building Materials* 110 (2016) 182–188. doi:10.1016/j.conbuildmat.2016.02.035.
- [250] M. Zhang, Y. He, G. Ye, D. A. Lange, K. v. Breugel, Computational investigation on mass diffusivity in Portland cement paste based on X-ray computed microtomography (μ CT) image, *Construction and Building Materials* 27 (1) (2012) 472–481. doi:10.1016/j.conbuildmat.2011.07.017.
- [251] Y.-S. Wang, J.-G. Dai, X-ray computed tomography for pore-related characterization and simulation of cement mortar matrix, *NDT & E International* 86 (2017) 28–35. doi:10.1016/j.ndteint.2016.11.005.
- [252] M. Zhang, Pore-scale modelling of relative permeability of cementitious

- materials using X-ray computed microtomography images, *Cement and Concrete Research* 95 (2017) 18–29. doi:10.1016/j.cemconres.2017.02.005.
- [253] E. Gallucci, K. Scrivener, A. Groso, M. Stamboni, G. Margaritondo, 3d experimental investigation of the microstructure of cement pastes using synchrotron X-ray microtomography (μ CT), *Cement and Concrete Research* 37 (3) (2007) 360–368. doi:10.1016/j.cemconres.2006.10.012.
- [254] A. du Plessis, B. J. Olawuyi, W. P. Boshoff, S. G. le Roux, Simple and fast porosity analysis of concrete using X-ray computed tomography, *Materials and Structures* 49 (1-2) (2016) 553–562. doi:10.1617/s11527-014-0519-9.
- [255] E. E. Bernardes, E. V. Mantilla Carrasco, W. L. Vasconcelos, A. G. de Magalhães, X-ray microtomography (μ -CT) to analyze the pore structure of a Portland cement composite based on the selection of different regions of interest, *Construction and Building Materials* 95 (2015) 703–709. doi:10.1016/j.conbuildmat.2015.07.128.
- [256] K. Y. Kim, T. S. Yun, J. Choo, D. H. Kang, H. S. Shin, Determination of air-void parameters of hardened cement-based materials using X-ray computed tomography, *Construction and Building Materials* 37 (2012) 93–101. doi:10.1016/j.conbuildmat.2012.07.012.
- [257] M. G. Sierra Beltran, E. Schlagen, Fibre-matrix interface properties in a wood fibre reinforced cement matrix, in: B. H. Oh (Ed.), *Proceedings of the VII International Conference on Fracture Mechanics of Concrete and Concrete Structures, IA-FraMCoS, Jeju, S. Korea, 2010*, pp. 1425–1430.
- [258] K. J. Trainor, L. S. Flanders, E. N. Landis, 3d measurements to determine micromechanical energy dissipation in steel fiber reinforced concrete, in: J. Van Mier, G. Ruiz, C. Andrade, R. Yu, X. Zhang (Eds.), *Proceedings of the VIII International Conference on Fracture Mechanics of Concrete and Concrete Structures, IA-FraMCoS, Toledo, Spain, 2013*, p. 101.
- [259] B. Zhou, Y. Uchida, Influence of flowability, casting time and formwork geometry on fiber orientation and mechanical properties of UHPFRC, *Cement and Concrete Research* 95 (2017) 164–177. doi:10.1016/j.cemconres.2017.02.017.
- [260] D. Hernández-Cruz, C. W. Hargis, S. Bae, P. A. Itty, C. Meral, J. Dominowski, M. J. Radler, D. A. Kilcoyne, P. J. Monteiro, Multiscale characterization of chemical–mechanical interactions between polymer fibers and cementitious matrix, *Cement and Concrete Composites* 48 (2014) 9–18. doi:10.1016/j.cemconcomp.2014.01.001.
- [261] V. Machovič, J. Andertová, L. Kopecký, M. Černý, L. Borecká, O. Píbyl, F. Kolář, J. Svítlová, Effect of aging of PET fibre on the mechanical properties of PET fibre reinforced cement composite, *Ceramics-Silikáty* 52 (3) (2008) 172–182.
- [262] Z. Wang, J. Gao, T. Ai, W. Jiang, P. Zhao, Quantitative evaluation of carbon fiber dispersion in cement based composites, *Construction and Building Materials* 68 (2014) 26–30. doi:10.1016/j.conbuildmat.2014.06.035.
- [263] J. Gao, Z. Wang, T. Zhang, L. Zhou, Dispersion of carbon fibers in cement-based composites with different mixing methods, *Construction and Building Materials* 134 (2017) 220–227. doi:10.1016/j.conbuildmat.2016.12.047.
- [264] H. M. Park, G. Kim, S. Y. Lee, H. Jeon, S. Y. Kim, M. Kim, J. W. Kim, Y. C. Jung, B. Yang, Electrical resistivity reduction with pitch-based carbon fiber into multi-walled carbon nanotube (MWCNT)-embedded cement composites, *Construction and Building Materials* 165 (2018) 484–493. doi:10.1016/j.conbuildmat.2017.12.205.
- [265] J. Gao, A. Sha, Z. Wang, L. Hu, D. Yun, Z. Liu, Y. Huang, Characterization of carbon fiber distribution in cement-based composites by Computed Tomography, *Construction and Building Materials* 177 (2018) 134–147. doi:10.1016/j.conbuildmat.2018.05.114.
- [266] A. R. Sakulich, D. P. Bentz, Increasing the Service Life of Bridge Decks by Incorporating Phase-Change Materials to Reduce Freeze-Thaw Cycles, *Journal of Materials in Civil Engineering* 24 (8) (2012) 1034–1042. doi:10.1061/(ASCE)MT.1943-5533.0000381.
- [267] M. Aguayo, S. Das, A. Maroli, N. Kabay, J. C. Mertens, S. D. Rajan, G. Sant, N. Chawla, N. Neithalath, The influence of microencapsulated phase change material (PCM) characteristics on the microstructure and strength of cementitious composites: Experiments and finite element simulations, *Cement and Concrete Composites* 73 (2016) 29–41. doi:10.1016/j.cemconcomp.2016.06.018.
- [268] V. Rheinheimer, Y. Wu, T. Wu, K. Celik, J. Wang, L. De Lorenzis, P. Wriggers, M.-H. Zhang, P. J. Monteiro, Multi-scale study of high-strength low-thermal-conductivity cement composites containing cenospheres, *Cement and Concrete Composites* 80 (2017) 91–103. doi:10.1016/j.cemconcomp.2017.03.002.
- [269] F. Bennai, C. El Hachem, K. Abahri, R. Belarbi, Microscopic hydric characterization of hemp concrete by X-ray microtomography and digital volume correlation, *Construction and Building Materials* 188 (2018) 983–994. doi:10.1016/j.conbuildmat.2018.08.198.
- [270] X. Li, L. Wang, Y. Liu, W. Li, B. Dong, W. H. Duan, Dispersion of graphene oxide agglomerates in cement paste and its effects on electrical resistivity and flexural strength, *Cement and Concrete Composites* 92 (2018) 145–154. doi:10.1016/j.cemconcomp.2018.06.008.
- [271] W.-J. Long, Y.-c. Gu, B.-X. Xiao, Q.-m. Zhang, F. Xing, Micro-mechanical properties and multi-scaled pore structure of graphene oxide cement paste: Synergistic application of nanoindentation, X-ray computed tomography, and SEM-EDS analysis, *Construction and Building Materials* 179 (2018) 661–674. doi:10.1016/j.conbuildmat.2018.05.229.
- [272] B. Pang, Y. Zhang, G. Liu, Study on the effect of waterborne epoxy resins on the performance and microstructure of cement paste, *Construction and Building Materials* 167 (2018) 831–845. doi:10.1016/j.conbuildmat.2018.02.096.
- [273] S. Diamond, E. Landis, Microstructural features of a mortar as seen by computed microtomography, *Materials and Structures* 40 (9) (2007) 989–993. doi:10.1617/s11527-006-9194-9.
- [274] M. D. Jackson, E. N. Landis, P. F. Brune, M. Vitti, H. Chen, Q. Li, M. Kunz, H.-R. Wenk, P. J. M. Monteiro, A. R. Ingrassia, Mechanical resilience and cementitious processes in Imperial Roman architectural mortar, *Proceedings of the National Academy of Sciences* 111 (52) (2014) 18484–18489. doi:10.1073/pnas.1417456111.
- [275] T. Oesch, E. Landis, D. Kuchma, A methodology for quantifying the impact of casting procedure on anisotropy in fiber-reinforced concrete using X-ray CT, *Materials and Structures* 51 (3) (2018) 73. doi:10.1617/s11527-018-1198-8.
- [276] M. Mironova, M. Ivanova, V. Naidenov, I. Georgiev, J. Stary, Advance study of fiber-reinforced self-compacting concrete, in: *AIP Conference Proceedings*, Vol. 1684, AIP Publishing, 2015, p. 030009. doi:10.1063/1.4934293.
- [277] T. Ponikiewski, J. Gołaszewski, M. Rudzki, M. Bugdol, Determination of steel fibres distribution in self-compacting concrete beams using X-ray computed tomography, *Archives of Civil and Mechanical Engineering* 15 (2) (2015) 558–568. doi:10.1016/j.acme.2014.08.008.
- [278] E. Verstryne, C. Van Steen, J. Andries, K. Van Balen, L. Vandewalle, M. Wevers, Experimental Study of Failure Mechanisms in Brittle Construction Materials by Means of X-Ray Microfocus Computed Tomography, in: *Proceedings of the IX International Conference on Fracture Mechanics of Concrete and Concrete Structures, IA-FraMCoS, Berkeley, California USA, 2016*. doi:10.21012/FC9.092.
- [279] D. C. González, J. Mínguez, M. A. Vicente, F. Cambronero, G. Aragón, Study of the effect of the fibers' orientation on the post-cracking behavior of steel fiber reinforced concrete from wedge-splitting tests and computed tomography scanning, *Construction and Building Materials* 192 (2018) 110–122. doi:10.1016/j.conbuildmat.2018.10.104.
- [280] H. Herrmann, E. Pastorelli, A. Kallonen, J.-P. Suuronen, Methods for fibre orientation analysis of X-ray tomography images of steel fibre reinforced concrete (SFRC), *Journal of Materials Science* 51 (8) (2016) 3772–3783. doi:10.1007/s10853-015-9695-4.
- [281] R. Mu, H. Li, L. Qing, J. Lin, Q. Zhao, Aligning steel fibers in cement mortar using electro-magnetic field, *Construction and Building Materials* 131 (2017) 309–316. doi:10.1016/j.conbuildmat.2016.11.081.
- [282] A. C. Bordelon, J. R. Roesler, Spatial distribution of synthetic fibers in concrete with X-ray computed tomography, *Cement and Concrete Composites* 53 (2014) 35–43. doi:10.1016/j.cemconcomp.2014.04.007.
- [283] D. Hernández-Cruz, C. W. Hargis, J. Dominowski, M. J. Radler, P. J. Monteiro, Fiber reinforced mortar affected by alkali-silica reaction: A study by synchrotron microtomography, *Cement and Concrete Composites* 68 (2016) 123–130. doi:10.1016/j.cemconcomp.2016.02.

003.

- [284] E. Garboczi, J. Bullard, Shape analysis of a reference cement, *Cement and Concrete Research* 34 (10) (2004) 1933–1937. doi:10.1016/j.cemconres.2004.01.006.
- [285] S. Erdoğan, X. Nie, P. Stutzman, E. Garboczi, Micrometer-scale 3-D shape characterization of eight cements: Particle shape and cement chemistry, and the effect of particle shape on laser diffraction particle size measurement, *Cement and Concrete Research* 40 (5) (2010) 731–739. doi:10.1016/j.cemconres.2009.12.006.
- [286] H. He, Z. Guo, P. Stroeven, M. Stroeven, L. J. Sluys, Strategy on simulation of arbitrary-shaped cement grains in concrete, *Image Analysis & Stereology* 29 (2) (2011) 79. doi:10.5566/ias.v29.p79-84.
- [287] H. He, P. Stroeven, E. Pirard, L. Courard, On the Shape Simulation of Aggregate and Cement Particles in a DEM System, *Advances in Materials Science and Engineering* 2015 (2015) 1–7. doi:10.1155/2015/692768.
- [288] E. Garboczi, Three-dimensional mathematical analysis of particle shape using X-ray tomography and spherical harmonics: Application to aggregates used in concrete, *Cement and Concrete Research* 32 (10) (2002) 1621–1638. doi:10.1016/S0008-8846(02)00836-0.
- [289] E. Masad, S. Saadeh, T. Al-Rousan, E. Garboczi, D. Little, Computations of particle surface characteristics using optical and X-ray CT images, *Computational Materials Science* 34 (4) (2005) 406–424. doi:10.1016/j.commatsci.2005.01.010.
- [290] T. Liu, S. Qin, D. Zou, W. Song, J. Teng, Mesoscopic modeling method of concrete based on statistical analysis of CT images, *Construction and Building Materials* 192 (2018) 429–441. doi:10.1016/j.conbuildmat.2018.10.136.
- [291] L. Holzer, B. Muench, M. Wegmann, P. Gasser, R. J. Flatt, FIB-Nanotomography of Particulate Systems—Part I: Particle Shape and Topology of Interfaces, *Journal of the American Ceramic Society* 89 (8) (2006) 2577–2585. doi:10.1111/j.1551-2916.2006.00974.x.
- [292] L. Holzer, R. J. Flatt, S. T. Erdoğan, J. W. Bullard, E. J. Garboczi, Shape Comparison between 0.4–2.0 and 20–60 μm Cement Particles, *Journal of the American Ceramic Society* (Mar. 2010). doi:10.1111/j.1551-2916.2010.03654.x.
- [293] B. Munch, P. Gasser, L. Holzer, R. Flatt, FIB-Nanotomography of Particulate Systems—Part II: Particle Recognition and Effect of Boundary Truncation, *Journal of the American Ceramic Society* 89 (8) (2006) 2586–2595. doi:10.1111/j.1551-2916.2006.01121.x.
- [294] H. F. W. Taylor, *Cement chemistry*, 2nd Edition, T. Telford, London, 1997.
- [295] D. Bentz, S. Mizell, S. Satterfield, J. Devaney, W. George, P. Ketcham, J. Graham, J. Porterfield, D. Quenard, F. Vallee, H. Sallee, E. Boller, J. Baruchel, The visible cement data set, *Journal of Research of the National Institute of Standards and Technology* 107 (2) (2002) 137–148. doi:10.6028/jres.107.013.
- [296] T. Deboodt, J. H. Ideker, O. B. Isgor, D. Wildenschild, Quantification of synthesized hydration products using synchrotron microtomography and spectral analysis, *Construction and Building Materials* 157 (2017) 476–488. doi:10.1016/j.conbuildmat.2017.09.031.
- [297] D. Gastaldi, F. Canonico, L. Capelli, E. Boccaleri, M. Milanesio, L. Palin, G. Croce, F. Marone, K. Mader, M. Stampanoni, In situ tomographic investigation on the early hydration behaviors of cementing systems, *Construction and Building Materials* 29 (2012) 284–290. doi:10.1016/j.conbuildmat.2011.10.016.
- [298] L. Wang, B. Yang, A. Abraham, L. Qi, X. Zhao, Z. Chen, Construction of dynamic three-dimensional microstructure for the hydration of cement using 3d image registration, *Pattern Analysis and Applications* 17 (3) (2014) 655–665. doi:10.1007/s10044-013-0335-9.
- [299] J. Adrien, S. Meille, S. Tadier, E. Maire, L. Sasaki, In-situ X-ray tomographic monitoring of gypsum plaster setting, *Cement and Concrete Research* 82 (2016) 107–116. doi:10.1016/j.cemconres.2015.12.011.
- [300] M. Moradian, Q. Hu, M. Aboustait, M. T. Ley, J. C. Hanan, X. Xiao, G. W. Scherer, Z. Zhang, Direct observation of void evolution during cement hydration, *Materials & Design* 136 (2017) 137–149. doi:10.1016/j.matdes.2017.09.056.
- [301] X. Zhu, Z. Zhang, K. Yang, B. Magee, Y. Wang, L. Yu, S. Nanukuttan, Q. Li, S. Mu, C. Yang, M. Basheer, Characterisation of pore structure development of alkali-activated slag cement during early hydration using electrical responses, *Cement and Concrete Composites* 89 (2018) 139–149. doi:10.1016/j.cemconcomp.2018.02.016.
- [302] T. J. Chotard, M. P. Boncoeur-Martel, A. Smith, J. P. Dupuy, C. Gault, Application of X-Ray Computed Tomography for Evaluating Density-Gradient Formation during Hydration of Aluminous Cement at the Young Age, *Key Engineering Materials* 206–213 (2002) 1863–1866. doi:10.4028/www.scientific.net/KEM.206-213.1863.
- [303] Z. Liu, Y. Zhang, G. Sun, Q. Jiang, Observation of microstructure formation process of cement paste using non-destructive methods, *Magazine of Concrete Research* 64 (11) (2012) 957–965. doi:10.1680/mac.11.00149.
- [304] L. Helfen, F. Dehn, P. Mikulík, T. Baumbach, Three-dimensional imaging of cement microstructure evolution during hydration, *Advances in Cement Research* 17 (3) (2005) 103–111. doi:10.1680/adcr.2005.17.3.103.
- [305] P. Levitz, V. Tarel, M. Stampanoni, E. Gallucci, Topology of evolving pore networks, *The European Physical Journal Applied Physics* 60 (2) (2012) 24202. doi:10.1051/epjap/2012120156.
- [306] N. Burlion, D. Bernard, D. Chen, X-ray microtomography: Application to microstructure analysis of a cementitious material during leaching process, *Cement and Concrete Research* 36 (2) (2006) 346–357. doi:10.1016/j.cemconres.2005.04.008.
- [307] R. El-Hachem, E. Rozière, F. Grondin, A. Loukili, Multi-criteria analysis of the mechanism of degradation of Portland cement based mortars exposed to external sulphate attack, *Cement and Concrete Research* 42 (10) (2012) 1327–1335. doi:10.1016/j.cemconres.2012.06.005.
- [308] T. Sugiyama, M. Promentilla, T. Hitomi, N. Takeda, Application of synchrotron microtomography for pore structure characterization of deteriorated cementitious materials due to leaching, *Cement and Concrete Research* 40 (8) (2010) 1265–1270. doi:10.1016/j.cemconres.2009.10.009.
- [309] K. Wan, Q. Xu, L. Li, W. Sun, 3d porosity distribution of partly calcium leached cement paste, *Construction and Building Materials* 48 (2013) 11–15. doi:10.1016/j.conbuildmat.2013.06.073.
- [310] M. Promentilla, S. Cortez, R. Papel, B. Tablada, T. Sugiyama, Evaluation of Microstructure and Transport Properties of Deteriorated Cementitious Materials from Their X-ray Computed Tomography (CT) Images, *Materials* 9 (5) (2016) 388. doi:10.3390/ma9050388.
- [311] T. Rougelot, N. Burlion, D. Bernard, F. Skoczylas, About microcracking due to leaching in cementitious composites: X-ray microtomography description and numerical approach, *Cement and Concrete Research* 40 (2) (2010) 271–283. doi:10.1016/j.cemconres.2009.09.021.
- [312] K. Wan, Y. Li, W. Sun, Application of tomography for solid calcium distributions in calcium leaching cement paste, *Construction and Building Materials* 36 (2012) 913–917. doi:10.1016/j.conbuildmat.2012.06.069.
- [313] A. Koenig, F. Dehn, Main considerations for the determination and evaluation of the acid resistance of cementitious materials, *Materials and Structures* 49 (5) (2016) 1693–1703. doi:10.1617/s11527-015-0605-7.
- [314] T. Dyer, Influence of cement type on resistance to attack from two carboxylic acids, *Cement and Concrete Composites* 83 (2017) 20–35. doi:10.1016/j.cemconcomp.2017.07.004.
- [315] K. P. Ramaswamy, M. Santhanam, A study of deterioration of cement paste due to acid attack using X-ray computed micro-tomography, *Advances in Cement Research* 30 (3) (2018) 123–138. doi:10.1680/jadcr.17.00032.
- [316] M. Muthu, M. Santhanam, Effect of reduced graphene oxide, alumina and silica nanoparticles on the deterioration characteristics of Portland cement paste exposed to acidic environment, *Cement and Concrete Composites* 91 (2018) 118–137. doi:10.1016/j.cemconcomp.2018.05.005.
- [317] S. Stock, N. Naik, A. Wilkinson, K. Kurtis, X-ray microtomography (microCT) of the progression of sulfate attack of cement paste, *Cement and Concrete Research* 32 (10) (2002) 1673–1675. doi:10.1016/S0008-8846(02)00814-1.
- [318] N. Naik, A. Jupe, S. Stock, A. Wilkinson, P. Lee, K. Kurtis, Sulfate attack monitored by microCT and EDXRD: Influence of cement type, water-to-cement ratio, and aggregate, *Cement and Concrete Research* 36 (1) (2006) 144–159. doi:10.1016/j.cemconres.2005.06.004.

- [319] Y. Yang, Y. Zhang, W. She, N. Liu, Z. Liu, In situ observing the erosion process of cement pastes exposed to different sulfate solutions with X-ray computed tomography, *Construction and Building Materials* 176 (2018) 556–565. doi:10.1016/j.conbuildmat.2018.05.093.
- [320] B. Šavija, M. Luković, S. A. S. Hosseini, J. Pacheco, E. Schlangen, Corrosion induced cover cracking studied by X-ray computed tomography, nanoindentation, and energy dispersive X-ray spectrometry (EDS), *Materials and Structures* 48 (7) (2015) 2043–2062. doi:10.1617/s11527-014-0292-9.
- [321] B. Dong, G. Fang, Y. Liu, P. Dong, J. Zhang, F. Xing, S. Hong, Monitoring reinforcement corrosion and corrosion-induced cracking by X-ray microcomputed tomography method, *Cement and Concrete Research* 100 (2017) 311–321. doi:10.1016/j.cemconres.2017.07.009.
- [322] A. Michel, B. J. Pease, M. R. Geiker, H. Stang, J. F. Olesen, Monitoring reinforcement corrosion and corrosion-induced cracking using non-destructive x-ray attenuation measurements, *Cement and Concrete Research* 41 (11) (2011) 1085–1094. doi:10.1016/j.cemconres.2011.06.006.
- [323] C. Van Steen, M. Wevers, E. Verstryngne, X-ray computed tomography for the detection of corrosion-induced damage at the reinforcement-concrete interface, in: *Proceedings of the 7th Conference on Industrial Computed Tomography*, Leuven, Belgium, 2017.
- [324] B. Dong, G. Shi, P. Dong, W. Ding, X. Teng, S. Qin, Y. Liu, F. Xing, S. Hong, Visualized tracing of rebar corrosion evolution in concrete with x-ray micro-computed tomography method, *Cement and Concrete Composites* 92 (2018) 102–109. doi:10.1016/j.cemconcomp.2018.06.003.
- [325] P.-A. Itty, M. Serdar, C. Meral, D. Parkinson, A. A. MacDowell, D. Bjegović, P. J. Monteiro, In situ 3d monitoring of corrosion on carbon steel and ferritic stainless steel embedded in cement paste, *Corrosion Science* 83 (2014) 409–418. doi:10.1016/j.corsci.2014.03.010.
- [326] J. Shi, J. Ming, Y. Zhang, J. Jiang, Corrosion products and corrosion-induced cracks of low-alloy steel and low-carbon steel in concrete, *Cement and Concrete Composites* 88 (2018) 121–129. doi:10.1016/j.cemconcomp.2018.02.002.
- [327] S. Erdem, X-ray computed tomography and fractal analysis for the evaluation of segregation resistance, strength response and accelerated corrosion behaviour of self-compacting lightweight concrete, *Construction and Building Materials* 61 (2014) 10–17. doi:10.1016/j.conbuildmat.2014.02.070.
- [328] A. Rodríguez, S. Gutiérrez-González, M. I. Prieto, A. Cobo, V. Calderón, Analysis of long-term corrosion behavior in mortars containing recycled ladle furnace slag using computerized tomography and SEM: Long-term corrosion behavior in mortars with slag, *Materials and Corrosion* 66 (3) (2015) 199–205. doi:10.1002/maco.201407697.
- [329] A. Česen, T. Kosec, A. Legat, Characterization of steel corrosion in mortar by various electrochemical and physical techniques, *Corrosion Science* 75 (2013) 47–57. doi:10.1016/j.corsci.2013.05.015.
- [330] H. Sun, D. Zhao, Y. Gu, S. A. Memon, Z. Ren, B. Liu, X. Zhang, F. Xing, D. Li, Three-dimensional characterization of steel corrosion embedded in cement paste, *Construction and Building Materials* 143 (2017) 24–32. doi:10.1016/j.conbuildmat.2017.03.106.
- [331] B. Šavija, M. Luković, J. Pacheco, E. Schlangen, Cracking of the concrete cover due to reinforcement corrosion: A two-dimensional lattice model study, *Construction and Building Materials* 44 (2013) 626–638. doi:10.1016/j.conbuildmat.2013.03.063.
- [332] P. K. Mehta, P. J. M. Monteiro, *Concrete: microstructure, properties, and materials*, fourth edition Edition, McGraw-Hill Education, New York, 2014.
- [333] M. Voltolini, N. Marinoni, L. Mancini, Synchrotron X-ray computed microtomography investigation of a mortar affected by alkali-silica reaction: a quantitative characterization of its microstructural features, *Journal of Materials Science* 46 (20) (2011) 6633–6641. doi:10.1007/s10853-011-5614-5.
- [334] N. Marinoni, M. Voltolini, L. Mancini, F. Cella, Influence of aggregate mineralogy on alkali-silica reaction studied by X-ray powder diffraction and imaging techniques, *Journal of Materials Science* 47 (6) (2012) 2845–2855. doi:10.1007/s10853-011-6114-3.
- [335] S. Yang, H. Cui, C. S. Poon, Assessment of in-situ alkali-silica reaction (ASR) development of glass aggregate concrete prepared with dry-mix and conventional wet-mix methods by X-ray computed microtomography, *Cement and Concrete Composites* 90 (2018) 266–276. doi:10.1016/j.cemconcomp.2018.03.027.
- [336] N. Marinoni, M. Voltolini, M. A. T. M. Broekmans, L. Mancini, P. J. M. Monteiro, N. Rotiroli, E. Ferrari, A. Bernasconi, A combined synchrotron radiation micro computed tomography and micro X-ray diffraction study on deleterious alkali-silica reaction, *Journal of Materials Science* 50 (24) (2015) 7985–7997. doi:10.1007/s10853-015-9364-7.
- [337] T. Wu, I. Temizer, P. Wriggers, Multiscale hydro-thermo-chemomechanical coupling: Application to alkali-silica reaction, *Computational Materials Science* 84 (2014) 381–395. doi:10.1016/j.commatsci.2013.12.029.
- [338] V. Ngala, C. Page, Effects of carbonation on pore structure and diffusional properties of hydrated cement pastes, *Cement and Concrete Research* 27 (7) (1997) 995–1007. doi:10.1016/S0008-8846(97)00102-6.
- [339] A. Morandau, M. Thiéry, P. Dangla, Impact of accelerated carbonation on OPC cement paste blended with fly ash, *Cement and Concrete Research* 67 (2015) 226–236. doi:10.1016/j.cemconres.2014.10.003.
- [340] J. Han, Y. Liang, W. Sun, W. Liu, S. Wang, Microstructure Modification of Carbonated Cement Paste with Six Kinds of Modern Microscopic Instruments, *Journal of Materials in Civil Engineering* 27 (10) (2015) 04014262. doi:10.1061/(ASCE)MT.1943-5533.0001210.
- [341] D. Cui, W. Sun, N. Banthia, Use of tomography to understand the influence of preconditioning on carbonation tests in cement-based materials, *Cement and Concrete Composites* 88 (2018) 52–63. doi:10.1016/j.cemconcomp.2018.01.011.
- [342] K. Wan, Q. Xu, Y. Wang, G. Pan, 3d spatial distribution of the calcium carbonate caused by carbonation of cement paste, *Cement and Concrete Composites* 45 (2014) 255–263. doi:10.1016/j.cemconcomp.2013.10.011.
- [343] J. Han, W. Sun, G. Pan, In situ dynamic XCT imaging of the microstructure evolution of cement mortar in accelerated carbonation reaction, *Magazine of Concrete Research* 64 (11) (2012) 1025–1031. doi:10.1680/mac.11.00173.
- [344] J. Han, W. Sun, G. Pan, Analysis of different contents of blast-furnace slag effect on carbonation properties of hardened binder paste using micro-XCT technique, in: G. Ye, K. van Breugel, W. Sun, C. Miao (Eds.), *Proceedings of the 2nd International Conference on Microstructural-related Durability of Cementitious Composites*, Vol. Pro083, RILEM Publications SARL, 2012, pp. 228–234.
- [345] T. Ahn, D. Kim, S. Kang, Crack Self-Healing Behavior of High Performance Fiber Reinforced Cement Composites under Various Environmental Conditions, in: *Earth and Space 2012, Proceedings*, ASCE, Pasadena, California, United States, 2012. doi:10.1061/9780784412190.068.
- [346] K. Van Tittelboom, D. Snoeck, P. Vontobel, F. H. Wittmann, N. De Belie, Use of neutron radiography and tomography to visualize the autonomous crack sealing efficiency in cementitious materials, *Materials and Structures* 46 (1-2) (2013) 105–121. doi:10.1617/s11527-012-9887-1.
- [347] J. Wang, J. Dewanckele, V. Cnudde, S. Van Vlierberghe, W. Verstraete, N. De Belie, X-ray computed tomography proof of bacterial-based self-healing in concrete, *Cement and Concrete Composites* 53 (2014) 289–304. doi:10.1016/j.cemconcomp.2014.07.014.
- [348] K. Olivier, A. Darquennes, F. Benboudjema, R. Gagné, Early-Age Self-Healing of Cementitious Materials Containing Ground Granulated Blast-Furnace Slag under Water Curing, *Journal of Advanced Concrete Technology* 14 (11) (2016) 717–727. doi:10.3151/jact.14.717.
- [349] A. R. Suleiman, M. L. Nehdi, Effect of environmental exposure on autogenous self-healing of cracked cement-based materials, *Cement and Concrete Research* 111 (2018) 197–208. doi:10.1016/j.cemconres.2018.05.009.
- [350] G. Hong, S. Choi, Rapid self-sealing of cracks in cementitious materials incorporating superabsorbent polymers, *Construction and Building Materials* 143 (2017) 366–375. doi:10.1016/j.conbuildmat.2017.03.133.
- [351] L.-Y. Lv, H. Zhang, E. Schlangen, Z. Yang, F. Xing, Experimental and numerical study of crack behaviour for capsule-based self-healing cementitious materials, *Construction and Building Materials* 156 (2017) 219–229. doi:10.1016/j.conbuildmat.2017.08.157.

- [352] L. Lv, E. Schlangen, Z. Yang, F. Xing, Micromechanical Properties of a New Polymeric Microcapsule for Self-Healing Cementitious Materials, *Materials* 9 (12) (2016) 1025. doi:10.3390/ma9121025.
- [353] F. Gilabert, K. Van Tittelboom, J. Van Stappen, V. Cnudde, N. De Belie, W. Van Paeppegem, Integral procedure to assess crack filling and mechanical contribution of polymer-based healing agent in encapsulation-based self-healing concrete, *Cement and Concrete Composites* 77 (2017) 68–80. doi:10.1016/j.cemconcomp.2016.12.001.
- [354] G. Fang, Y. Liu, S. Qin, W. Ding, J. Zhang, S. Hong, F. Xing, B. Dong, Visualized tracing of crack self-healing features in cement/microcapsule system with X-ray microcomputed tomography, *Construction and Building Materials* 179 (2018) 336–347. doi:10.1016/j.conbuildmat.2018.05.193.
- [355] B. Dong, W. Ding, S. Qin, N. Han, G. Fang, Y. Liu, F. Xing, S. Hong, Chemical self-healing system with novel microcapsules for corrosion inhibition of rebar in concrete, *Cement and Concrete Composites* 85 (2018) 83–91. doi:10.1016/j.cemconcomp.2017.09.012.
- [356] J. Chen, X. Deng, Y. Luo, L. He, Q. Liu, X. Qiao, Investigation of microstructural damage in shotcrete under a freeze–thaw environment, *Construction and Building Materials* 83 (2015) 275–282. doi:10.1016/j.conbuildmat.2015.02.042.
- [357] S. Jungwirth, X. Shi, Laboratory Investigation of Naturally Sourced Liquid Deicers and Subsequent Decision Support, *Journal of Cold Regions Engineering* 31 (3) (2017) 06017002. doi:10.1061/(ASCE)CR.1943-5495.0000132.
- [358] Q. Luo, D. Liu, P. Qiao, Q. Feng, L. Sun, Microstructural damage characterization of concrete under freeze-thaw action, *International Journal of Damage Mechanics* (2017) 1056789517736573. doi:10.1177/1056789517736573.
- [359] Y. Shields, E. Garboczi, J. Weiss, Y. Farnam, Freeze-thaw crack determination in cementitious materials using 3d X-ray computed tomography and acoustic emission, *Cement and Concrete Composites* 89 (2018) 120–129. doi:10.1016/j.cemconcomp.2018.03.004.
- [360] F. Liu, Z. You, X. Yang, H. Wang, Macro-micro degradation process of fly ash concrete under alternation of freeze-thaw cycles subjected to sulfate and carbonation, *Construction and Building Materials* 181 (2018) 369–380. doi:10.1016/j.conbuildmat.2018.06.037.
- [361] J. Yuan, Y. Wu, J. Zhang, Characterization of air voids and frost resistance of concrete based on industrial computerized tomographical technology, *Construction and Building Materials* 168 (2018) 975–983. doi:10.1016/j.conbuildmat.2018.01.117.
- [362] M. A. B. Promentilla, T. Sugiyama, X-Ray Microtomography of Mortars Exposed to Freezing-Thawing Action, *Journal of Advanced Concrete Technology* 8 (2) (2010) 97–111. doi:10.3151/jact.8.97.
- [363] M. A. B. Promentilla, T. Sugiyama, J. W. Z. Lu, A. Y. T. Leung, V. P. Iu, K. M. Mok, Computation of Crack Tortuosity from Microtomographic Images of Cement-based Materials, in: *AIP Conference Proceedings*, Vol. 1233, 2010, pp. 1378–1383. doi:10.1063/1.3452106.
- [364] M. Hain, P. Wriggers, Computational homogenization of microstructural damage due to frost in hardened cement paste, *Finite Elements in Analysis and Design* 44 (5) (2008) 233–244. doi:10.1016/j.finel.2007.11.020.
- [365] K. Y. Kim, T. S. Yun, K. P. Park, Evaluation of pore structures and cracking in cement paste exposed to elevated temperatures by X-ray computed tomography, *Cement and Concrete Research* 50 (2013) 34–40. doi:10.1016/j.cemconres.2013.03.020.
- [366] L. Sitek, Analysis of inner structure changes of concretes exposed to high temperatures using micro X-ray computed tomography, *Acta Geodynamica et Geomaterialia* (2015) 79–89. doi:10.13168/AGG.2015.0009.
- [367] O. Rivera, W. Long, C. Weiss Jr., R. Moser, B. Williams, K. Torres-Cancel, E. Gore, P. Allison, Effect of elevated temperature on alkali-activated geopolymers compared to portland cement-based binders, *Cement and Concrete Research* 90 (2016) 43–51. doi:10.1016/j.cemconres.2016.09.013.
- [368] Y.-M. Su, T.-C. Hou, L.-C. Lin, G.-Y. Chen, H.-H. Pan, The nondestructive evaluation of high temperature conditioned concrete in conjunction with acoustic emission and x-ray computed tomography, in: T. Yu, A. L. Gyekenyesi, P. J. Shull, H. F. Wu (Eds.), *Proceedings of the SPIE*, Vol. 98040L, SPIE, Las Vegas, Nevada, United States, 2016. doi:10.1117/12.2228107.
- [369] A. Kashani, T. D. Ngo, B. Walkley, P. Mendis, Thermal performance of calcium-rich alkali-activated materials: A microstructural and mechanical study, *Construction and Building Materials* 153 (2017) 225–237. doi:10.1016/j.conbuildmat.2017.07.119.
- [370] Y.-L. Li, X.-L. Zhao, R. Singh Raman, S. Al-Saadi, Thermal and mechanical properties of alkali-activated slag paste, mortar and concrete utilising seawater and sea sand, *Construction and Building Materials* 159 (2018) 704–724. doi:10.1016/j.conbuildmat.2017.10.104.
- [371] R. Anay, V. Soltangharai, L. Assi, T. DeVol, P. Ziehl, Identification of damage mechanisms in cement paste based on acoustic emission, *Construction and Building Materials* 164 (2018) 286–296. doi:10.1016/j.conbuildmat.2017.12.207.
- [372] A. Bouterf, S. Roux, F. Hild, J. Adrien, E. Maire, S. Meille, Digital Volume Correlation Applied to X-ray Tomography Images from Spherical Indentation Tests on Lightweight Gypsum, *Strain* 50 (5) (2014) 444–453. doi:10.1111/str.12101.
- [373] S. P. Shah, S. Choi, Nondestructive Techniques for Studying Fracture Processes in Concrete, *International Journal of Fracture* 98 (3-4) (1999) 351. doi:10.1023/A:1018620008780.
- [374] C. Poinard, E. Piotrowska, Y. Malecot, L. Daudeville, E. N. Landis, Compression triaxial behavior of concrete: the role of the mesostructure by analysis of X-ray tomographic images, *European Journal of Environmental and Civil Engineering* 16 (sup1) (2012) s115–s136. doi:10.1080/19648189.2012.682458.
- [375] G. G. Liu, A. B. Ma, H. G. Qin, P. Zhang, Propagating and Reconstructing Cracks in 3d in Cement-Based Materials, *Applied Mechanics and Materials* 578-579 (2014) 1441–1445. doi:10.4028/www.scientific.net/AMM.578-579.1441.
- [376] H. Elaqra, N. Godin, G. Peix, M. R’Mili, G. Fantozzi, Damage evolution analysis in mortar, during compressive loading using acoustic emission and X-ray tomography: Effects of the sand/cement ratio, *Cement and Concrete Research* 37 (5) (2007) 703–713. doi:10.1016/j.cemconres.2007.02.008.
- [377] K. Wan, W. Sun, C. Tang, Z. Rong, Three-dimensional analysis of micro defect morphologies in cement-based materials using focused ion beam tomography, *Science China Technological Sciences* 55 (6) (2012) 1539–1544. doi:10.1007/s11431-012-4780-2.
- [378] T. S. Oesch, E. N. Landis, D. A. Kuchma, Conventional Concrete and UHPC Performance–Damage Relationships Identified Using Computed Tomography, *Journal of Engineering Mechanics* 142 (12) (2016) 04016101. doi:10.1061/(ASCE)EM.1943-7889.0001168.
- [379] P. Trtik, J. V. Mier, M. Stampanoni, Three dimensional crack detection in hardened cement pastes using synchrotron-based computer microtomography (SR μ CT), in: *Proceedings of the 11th International Conference on Fracture 2005*, Turin, Italy, 2005.
- [380] Y.-S. Wang, J.-G. Dai, Use of magnesia sand for optimal design of high performance magnesium potassium phosphate cement mortar, *Construction and Building Materials* 153 (2017) 385–392. doi:10.1016/j.conbuildmat.2017.07.099.
- [381] M. Malbois, A. Darquennes, C. De Sa, F. Benboudjema, Experimental Study on the Effects of Aggregates Restraint on the Delayed Behavior of Cementitious Materials, in: *Proceedings of the 10th International Conference on Mechanics and Physics of Creep, Shrinkage, and Durability of Concrete and Concrete Structures*, American Society of Civil Engineers, Vienna, Austria, 2015, pp. 1167–1176. doi:10.1061/9780784479346.139.
- [382] L. Li, Y. Jia, T. Rougelot, N. Burlion, Effects of inclusion stiffness on the cracking of cement-based composites under drying: a numerical study, *European Journal of Environmental and Civil Engineering* (2017) 1–23. doi:10.1080/19648189.2017.1363088.
- [383] E. N. Landis, E. N. Nagy, D. T. Keane, Microtomographic Measurements of Internal Damage in Portland-Cement-Based Composites, *Journal of Aerospace Engineering* 10 (1) (1997) 2–6. doi:10.1061/(ASCE)0893-1321(1997)10:1(2).
- [384] K. Wan, X. Xue, In situ compressive damage of cement paste characterized by lab source X-ray computer tomography, *Materials Characterization* 82 (2013) 32–40. doi:10.1016/j.matchar.2013.05.004.
- [385] Z. Yang, W. Ren, R. Sharma, S. McDonald, M. Mostafavi, Y. Vertyagina, T. Marrow, In-situ X-ray computed tomography characterisation of 3d fracture evolution and image-based numerical homogenisation of concrete, *Cement and Concrete Composites* 75 (2017) 74–83. doi:

- 10.1016/j.cemconcomp.2016.10.001.
- [386] X. Chen, H. Q. Yang, Y. Z. Zuo, Y. Shi, K. T. Xiao, Interfacial Transition Zone Micro-Structure of Light-Burnt MgO Concrete, *Advanced Materials Research* 415-417 (2011) 514–518. doi:10.4028/www.scientific.net/AMR.415-417.514.
- [387] T. Nguyen, J. Yvonnet, M. Bornert, C. Chateau, Initiation and propagation of complex 3d networks of cracks in heterogeneous quasi-brittle materials: Direct comparison between in situ testing-microCT experiments and phase field simulations, *Journal of the Mechanics and Physics of Solids* 95 (2016) 320–350. doi:10.1016/j.jmps.2016.06.004.
- [388] E. N. Landis, C. Gangsa, L. S. Flanders, Revisiting Critical Flaws in Cement-Based Composites, *Journal of Nanomechanics and Micromechanics* 6 (4) (2016) 04016007. doi:10.1061/(ASCE)NM.2153-5477.0000111.
- [389] T. Nguyen, A. Ghazlan, A. Kashani, S. Bordas, T. Ngo, 3d meso-scale modelling of foamed concrete based on X-ray Computed Tomography, *Construction and Building Materials* 188 (2018) 583–598. doi:10.1016/j.conbuildmat.2018.08.085.
- [390] Ł. Skarżyński, J. Tejchman, Experimental Investigations of Fracture Process in Concrete by Means of X-ray Micro-computed Tomography: X-ray Micro-computed Tomography, *Strain* 52 (1) (2016) 26–45. doi:10.1111/str.12168.
- [391] Ł. Skarżyński, J. Suchozrewski, Mechanical and fracture properties of concrete reinforced with recycled and industrial steel fibers using Digital Image Correlation technique and X-ray micro computed tomography, *Construction and Building Materials* 183 (2018) 283–299. doi:10.1016/j.conbuildmat.2018.06.182.
- [392] S. C. de Wolski, J. E. Bolander, E. N. Landis, An In-Situ X-Ray Microtomography Study of Split Cylinder Fracture in Cement-Based Materials, *Experimental Mechanics* 54 (7) (2014) 1227–1235. doi:10.1007/s11340-014-9875-1.
- [393] C. Chateau, T. T. Nguyen, M. Bornert, J. Yvonnet, DVC-based image subtraction to detect microcracking in lightweight concrete, *Strain* 54 (5) (2018) e12276. doi:10.1111/str.12276.
- [394] E. Schlangen, Z. Qian, 3d MODELING OF FRACTURE IN CEMENT-BASED MATERIALS, *Journal of Multiscale Modelling* 01 (02) (2009) 245–261. doi:10.1142/S1756973709000116.
- [395] M. Zhang, A. P. Jivkov, Microstructure-informed modelling of damage evolution in cement paste, *Construction and Building Materials* 66 (2014) 731–742. doi:10.1016/j.conbuildmat.2014.06.017.
- [396] M. Nitka, Ł. Skarżyński, J. Tejchman, Simulations of fracture in concrete beams under bending using a continuum and discrete approach, in: *Proceedings of the XIII International Conference on Computational Plasticity : fundamentals and applications*, CIMNE, Barcelona, 2015, pp. 1065–1076.
- [397] W. Ren, Z. Yang, R. Sharma, C. Zhang, P. J. Withers, Two-dimensional X-ray CT image based meso-scale fracture modelling of concrete, *Engineering Fracture Mechanics* 133 (2015) 24–39. doi:10.1016/j.engfracmech.2014.10.016.
- [398] Ł. Skarżyński, M. Nitka, J. Tejchman, Modelling of concrete fracture at aggregate level using FEM and DEM based on X-ray μ CT images of internal structure, *Engineering Fracture Mechanics* 147 (2015) 13–35. doi:10.1016/j.engfracmech.2015.08.010.
- [399] Y. Huang, Z. Yang, G. Liu, X-Ray Computed Tomography Image-Based Meso-scale Dynamic Fracture of Concrete Under Compression: Monte Carlo Simulations, in: *Proceedings of the IX International Conference on Fracture Mechanics of Concrete and Concrete Structures*, IA-FraMCoS, Berkeley, California USA, 2016. doi:10.21012/FC9.065.
- [400] H. Zhang, B. Šavija, S. C. Figueiredo, E. Schlangen, Experimentally validated multi-scale modelling scheme of deformation and fracture of cement paste, *Cement and Concrete Research* 102 (2017) 175–186. doi:10.1016/j.cemconres.2017.09.011.
- [401] T.-S. Han, X. Zhang, J.-S. Kim, S.-Y. Chung, J.-H. Lim, C. Linder, Area of lineal-path function for describing the pore microstructures of cement paste and their relations to the mechanical properties simulated from μ -CT microstructures, *Cement and Concrete Composites* 89 (2018) 1–17. doi:10.1016/j.cemconcomp.2018.02.008.
- [402] M. Nitka, J. Tejchman, A three-dimensional meso-scale approach to concrete fracture based on combined DEM with X-ray μ CT images, *Cement and Concrete Research* 107 (2018) 11–29. doi:10.1016/j.cemconres.2018.02.006.
- [403] O. Coussy, *Mechanics and Physics of Porous Solids*, John Wiley & Sons Ltd, Chichester, United Kingdom, 2010.
- [404] F. Prade, K. Fischer, D. Heinz, P. Meyer, J. Mohr, F. Pfeiffer, Time resolved X-ray Dark-Field Tomography Revealing Water Transport in a Fresh Cement Sample, *Scientific Reports* 6 (1) (Sep. 2016). doi:10.1038/srep29108.
- [405] S. Brisard, R. S. Chae, I. Bihannic, L. Michot, P. Guttman, J. Thieme, G. Schneider, P. J. Monteiro, P. Levitz, Morphological quantification of hierarchical geomaterials by X-ray nano-CT bridges the gap from nano to micro length scales, *American Mineralogist* 97 (2-3) (2012) 480–483. doi:10.2138/am.2012.3985.
- [406] S. Bae, R. Taylor, D. Shapiro, P. Denes, J. Joseph, R. Celestre, S. Marchesini, H. Padmore, T. Tyliczszak, T. Warwick, D. Kilcoyne, P. Levitz, P. J. M. Monteiro, Soft X-ray Ptychographic Imaging and Morphological Quantification of Calcium Silicate Hydrates (C–S–H), *Journal of the American Ceramic Society* 98 (12) (2015) 4090–4095. doi:10.1111/jace.13808.
- [407] M. D. Jackson, J. Moon, E. Gotti, R. Taylor, S. R. Chae, M. Kunz, A.-H. Emwas, C. Meral, P. Guttman, P. Levitz, H.-R. Wenk, P. J. M. Monteiro, Material and Elastic Properties of Al-Tobermorite in Ancient Roman Seawater Concrete, *Journal of the American Ceramic Society* 96 (8) (2013) 2598–2606. doi:10.1111/jace.12407.
- [408] J. L. Provis, V. Rose, R. P. Winarski, J. S. van Deventer, Hard X-ray nanotomography of amorphous aluminosilicate cements, *Scripta Materialia* 65 (4) (2011) 316–319. doi:10.1016/j.scriptamat.2011.04.036.
- [409] Q. Hu, M. Aboustait, M. T. Ley, J. C. Hanan, V. Rose, R. Winarski, Combined three-dimensional structure and chemistry imaging with nanoscale resolution, *Acta Materialia* 77 (2014) 173–182. doi:10.1016/j.actamat.2014.05.050.
- [410] Q. Hu, M. Aboustait, T. Kim, M. T. Ley, J. C. Hanan, J. Bullard, R. Winarski, V. Rose, Direct three-dimensional observation of the microstructure and chemistry of C3s hydration, *Cement and Concrete Research* 88 (2016) 157–169. doi:10.1016/j.cemconres.2016.07.006.
- [411] Q. Hu, M. Aboustait, T. Kim, M. T. Ley, J. W. Bullard, G. Scherer, J. C. Hanan, V. Rose, R. Winarski, J. Gelb, Direct measurements of 3d structure, chemistry and mass density during the induction period of C3s hydration, *Cement and Concrete Research* 89 (2016) 14–26. doi:10.1016/j.cemconres.2016.07.008.
- [412] J. W. Bullard, J. Hagedorn, M. T. Ley, Q. Hu, W. Griffin, J. E. Terrill, A critical comparison of 3d experiments and simulations of tricalcium silicate hydration, *Journal of the American Ceramic Society* 101 (4) (2018) 1453–1470. doi:10.1111/jace.15323.
- [413] A. Sakdinawat, D. Attwood, Nanoscale X-ray imaging, *Nature Photonics* 4 (12) (2010) 840–848. doi:10.1038/nphoton.2010.267.
- [414] H. N. Chapman, K. A. Nugent, Coherent lensless X-ray imaging, *Nature Photonics* 4 (12) (2010) 833–839. doi:10.1038/nphoton.2010.240.
- [415] J. M. Rodenburg, Ptychography and Related Diffractive Imaging Methods, in: *Hawkes (Ed.), Advances in Imaging and Electron Physics*, Vol. 150, Elsevier, 2008, pp. 87–184. doi:10.1016/S1076-5670(07)00003-1.
- [416] W. Hoppe, Trace structure analysis, ptychography, phase tomography, *Ultramicroscopy* 10 (3) (1982) 187–198. doi:10.1016/0304-3991(82)90038-9.
- [417] G. Zheng, *Fourier Ptychographic Imaging*, 2053-2571, Morgan & Claypool Publishers, 2016. doi:10.1088/978-1-6817-4273-1.
- [418] F. Pfeiffer, X-ray ptychography, *Nature Photonics* 12 (1) (2018) 9–17. doi:10.1038/s41566-017-0072-5.
- [419] P. Trtik, A. Diaz, M. Guizar-Sicairos, A. Menzel, O. Bunk, Density mapping of hardened cement paste using ptychographic X-ray computed tomography, *Cement and Concrete Composites* 36 (2013) 71–77. doi:10.1016/j.cemconcomp.2012.06.001.
- [420] J. C. da Silva, P. Trtik, A. Diaz, M. Holler, M. Guizar-Sicairos, J. Raabe, O. Bunk, A. Menzel, Mass Density and Water Content of Saturated Never-Dried Calcium Silicate Hydrates, *Langmuir* 31 (13) (2015) 3779–3783. doi:10.1021/la504478j.
- [421] A. Cuesta, A. G. De la Torre, I. Santacruz, P. Trtik, J. C. da Silva, A. Diaz, M. Holler, M. A. G. Aranda, In situ hydration imaging study of a ye'elimite paste by ptychographic x-ray computed tomography, in: *Proceedings of the Thirty-Ninth Annual International Conference on Ce-*

ment Microscopy, Toronto, Canada, 2017.

- [422] A. Cuesta, A. G. De la Torre, I. Santacruz, P. Trtik, J. C. da Silva, A. Diaz, M. Holler, M. A. G. Aranda, Chemistry and Mass Density of Aluminum Hydroxide Gel in Eco-Cements by Ptychographic X-ray Computed Tomography, *The Journal of Physical Chemistry C* 121 (5) (2017) 3044–3054. [doi:10.1021/acs.jpcc.6b10048](https://doi.org/10.1021/acs.jpcc.6b10048).
- [423] D. Bentz, N. S. Martys, P. Stutzman, M. S. Levenson, E. Garboczi, J. Dunsmuir, L. M. Schwartz, X-Ray Microtomography of an Astm C109 Mortar Exposed to Sulfate Attack, *MRS Proceedings* 370 (1994) 77. [doi:10.1557/PROC-370-77](https://doi.org/10.1557/PROC-370-77).
- [424] J. Han, W. Liu, S. Wang, D. Du, F. Xu, W. Li, G. De Schutter, Effects of crack and ITZ and aggregate on carbonation penetration based on 3D micro X-ray CT microstructure evolution, *Construction and Building Materials* 128 (2016) 256–271. [doi:10.1016/j.conbuildmat.2016.10.062](https://doi.org/10.1016/j.conbuildmat.2016.10.062).
- [425] D. M. Pelt, J. A. Sethian, A mixed-scale dense convolutional neural network for image analysis, *Proceedings of the National Academy of Sciences* 115 (2) (2018) 254–259. [doi:10.1073/pnas.1715832114](https://doi.org/10.1073/pnas.1715832114).